

**Darstellung, Strukturen und Eigenschaften ausgewählter
Perowskit-Materialien und Molekülkristalle**

Von der Fakultät Chemie der Universität Stuttgart
zur Erlangung der Würde eines Doktors der
Naturwissenschaften (Dr. rer. nat.) genehmigte Abhandlung

Vorgelegt von
Jianwei Tong
aus Nanjing, China

Vorsitzender:	Prof. Dr. T. Schleid
Hauptberichter:	Prof. Dr. A. Simon
Mitberichter:	Prof. Dr. J. Köhler
weiterer Prüfer:	Prof. Dr. J. Bill

Tag der mündlichen Prüfung: 28. Oktober 2010

Max-Planck-Institut für Festkörperforschung, Stuttgart

2010

Preparations, Structures and Properties of Selected Perovskite Materials and Molecular Crystals

Von der Fakultät Chemie der Universität Stuttgart
zur Erlangung der Würde eines Doktors der
Naturwissenschaften (Dr. rer. nat.) genehmigte Abhandlung

Vorgelegt von
Jianwei Tong
aus Nanjing, China

Vorsitzender:	Prof. Dr. T. Schleid
Hauptberichter:	Prof. Dr. A. Simon
Mitberichter:	Prof. Dr. J. Köhler
weiterer Prüfer:	Prof. Dr. J. Bill

Tag der mündlichen Prüfung: 28. Oktober 2010

Max-Planck-Institut für Festkörperforschung, Stuttgart

2010

The outcome is simple, the process is tortuous.

Zusammenfassung

In dieser Dissertation werden präparative und strukturelle Untersuchungen von Silbernitriden diskutiert. Die triklinen ternären Fluoride, AgCuF_3 und NaCuF_3 , enthalten stark Jahn-Teller verzerrte CuF_6 Oktaeder und zeigen typische 1D antiferromagnetisches Verhalten bei niedrigen Temperaturen. Cs_2AgF_4 , ein 2D Heisenberg-Ferromagnet mit quadratischem Gitter, kristallisiert in der K_2NiF_4 -Struktur und seine magnetischen und optischen Eigenschaften werden diskutiert. Darüber hinaus haben wir die Möglichkeiten des Einschlusses von tetraedrischen Molekülen, z.B. OsO_4 und P_4 , in das CsF-Gitter untersucht. Zum Schluß sind strukturelle Studien auf SiBr_4 (m.p. 278 K) durchgeführt worden.

Abstract

In this dissertation preparative and structural studies of silver nitrides are discussed. The triclinic ternary fluorides AgCuF_3 and NaCuF_3 exhibit strongly Jahn-Teller distorted CuF_6 octahedra, and become typical 1D antiferromagnets at low temperatures. Cs_2AgF_4 , a 2D square-lattice Heisenberg ferromagnet, crystallizes in the K_2NiF_4 -type structure, and its magnetic and optical properties have been studied. Moreover, we have investigated the possibilities of the inclusion of tetrahedral molecules, e.g. OsO_4 and P_4 , into the CsF lattice. Finally structural studies have been performed on SiBr_4 (m.p. 278 K).

Table of Contents

1 Introduction	1
2 Experimental background	3
2.1 Preparative background	3
2.1.1 Treatment of reactants and products	3
2.1.2 Solid state reactions	4
2.1.3 Solid-gas reactions	4
2.1.4 Storage of air-sensitive substances	5
2.2 Starting materials	5
2.3 Characterization and analysis	6
2.3.1 X-ray diffraction (XRD)	6
2.3.1.1 Powder XRD	6
2.3.1.2 Single crystal XRD	6
2.3.1.3 Temperature-dependent Simon-Guinier camera	7
2.3.1.4 Energy-dispersive X-ray spectroscopy (EDX) and scanning electron microscope (SEM)	7
2.3.2 Neutron diffraction	7
2.3.3 Synchrotron diffraction	8
2.3.3.1 Synchrotron Powder diffraction	8
2.3.3.2 High pressure study	8
2.3.4 Structure refinement	9
2.3.4.1 Rietveld refinement	9
2.3.4.2 Single crystal structure refinement	9
2.3.5 Thermal properties	9
2.3.6 Magnetic properties	11
2.3.7 Optical properties	11
2.3.8 Computations	11

3 Structural and electrical properties of explosive silver nitrides	13
3.1 Introduction	13
3.2 Experimental section	14
3.2.1 Silver nitride synthesis	14
3.2.1.1 Aqueous ammonia route	14
3.2.1.2 Gaseous ammonia route	14
3.2.2 Other nitrides	15
3.2.3 Sample characterization	15
3.3 Results	15
3.3.1 Silver nitride	15
3.3.1.1 Synthesis	15
3.3.1.2 Structure determination	17
3.3.1.3 LDA calculations	20
3.3.1.4 Copper nitride	21
3.3.1.5 Discussion	22
3.3.2 Efforts to synthesize other binary nitrides	25
3.3.2.1 Palladium nitride	25
3.3.2.2 Gold nitride	25
3.3.2.3 Mercury nitride	26
3.3.3 Efforts to synthesize ternary copper nitrides	27
3.3.3.1 Silver copper nitride	27
3.3.3.2 Copper palladium nitride	29
3.4 Discussion	29
3.5 Conclusion	31
4 Preparations, structures and properties of triclinic perovskites AgCuF₃ and NaCuF₃	32
4.1 Introduction	32
4.2 Experimental section	
4.2.1 Sample preparation	33
4.2.2 Characterization	33
4.3 Results and Discussion	34
4.3.1 Crystal structure of AgCuF ₃	34

4.3.2 Thermal analysis	39
4.3.3 Magnetic susceptibilities	40
4.3.4 Electron paramagnetic resonance	43
4.3.5 Specific heat	49
4.3.6 Powder neutron diffraction studies	51
4.3.7 High pressure study of NaCuF ₃	55
4.3.8 Calculation of the spin exchange interactions of AgCuF ₃ and NaCuF ₃	56
4.4 Conclusion	56
5 Physical properties of two dimensional Cs₂AgF₄:	
Spin exchange of Ag²⁺ in layered Cs₂AgF₄ and dimers in Ag₂ZnZr₂F₁₄	57
5.1 Introduction	57
5.2 Experimental section	58
5.2.1 Sample preparation	58
5.2.2 Sample characterization	58
5.3 Results and discussions	58
5.3.1 Crystal structure	58
5.3.2 Magnetic susceptibility	61
5.3.3 Specific heat	63
5.3.4 Electron paramagnetic resonance	65
5.3.5 UV-Vis diffuse reflection	67
5.4 Spin exchange of Ag ²⁺ in dimers in Ag ₂ ZnZr ₂ F ₁₄	69
5.5 Conclusion	73
6 Reactions of CsF and compounds with tetrahedral molecules	74
6.1 Introduction	74
6.2 CsF+OsO ₄	75
6.2.1 Sample preparation and characterization	75
6.2.2 Results and discussions	75
6.2.2.1 Crystal structure	75
6.2.2.2 Raman spectroscopy	83
6.2.2.3 ¹⁹ F MAS NMR	85
6.2.2.4 Discussion	87

6.3 CsF+P ₄	88
6.3.1 Sample preparation and characterization	88
6.3.2 Results	88
6.3.3 Discussion	91
6.4 Conclusion	92
7 Crystal structure of SiBr₄	93
7.1 Introduction	93
7.2 Prediction	94
7.3 Experimental section	95
7.3.1 Characterization	95
7.3.2 DSC	96
7.3.3 Powder synchrotron diffraction	96
7.3.4 Studies of Transition between α -SiBr ₄ and β -SiBr ₄	104
7.3.5 Single crystal XRD	106
7.3.6 Discussion	109
7.4 Conclusion	111
Summary	112
List of Tables	115
List of Figures	117
Bibliography	124
Publications	131
Acknowledgement	133
Curriculum Vitae	135

Chapter 1

Introduction

Perovskite materials exhibit many interesting and intriguing properties from both the theoretical and the application point of view. These compounds are used as sensors and catalyst electrodes in certain types of fuel cells and are candidates for memory devices and spintronics applications. Although the most common perovskite compounds are oxides, there are also perovskite compounds with fluorine and nitrogen, as well as RT_3M (R : rare-earth or other relatively large ion, T : transition metal ion and M : light metalloids), e.g. $KCuF_3$ [1-4], Fe_4N [5], $Cu_3Pd_{0.989}N$ [6], $MgCNi_3$ [7] etc.

Besides the cubic perovskite structure, the orthorhombic and tetragonal phases are the most common non-cubic variants. ABX_3 , where A and B are two cations of very different sizes, and X is an anion that bonds to both. The A atoms are larger than the B atoms. The ideal cubic-symmetry structure has the B cation in 6-fold coordination, surrounded by an octahedron of anions, and the A cation in 12-fold cuboctahedral coordination. The relative ion size requirements for stability of the cubic structure are quite stringent, so slight buckling and distortion can produce several lower-symmetry distorted variants, in which the coordination numbers of A cations, B cations or both are reduced. For example, perovskites containing Jahn-Teller ions (e.g. Cu^{2+} and Mn^{3+}) on the octahedral site exhibit interesting physical properties, including charge ordering, spin ordering and cooperative Jahn-Teller distortions [8].

Nitrogen has one of the highest electronegativities, and metal nitrides often possess unique properties suitable for a number of applications, such as high hardness, high chemical stability and useful magnetic and electrical properties [9]. Transition metal nitrides, especially $3d$ metal nitrides, have been extensively studied [5, 10-15]. One example, Cu_3N , which crystallizes in the anti- ReO_3 type structure, represents an open cubic framework suitable for inclusion of Li, Pd or Cu [6, 11, 12]. Not much is known about binary nitrides of noble metals. Only the nitrides of Os, Ir and Pt have been synthesized under extreme conditions so far [16-22]. Recently a pernitride of palladium was proposed to have a possible stoichiometry of PdN_2 , which was prepared from high pressure reaction of Pd metal with N_2 using the laser-heated diamond anvil cell [23]. This type of structure is typical for noble metals, such as Ir [23], Pt [24] and Os [25]. Besides,

surface nitrides on gold films have been prepared by Šiller et al [9], by means of reactive ion sputtering and plasma etching, addressing the need to produce harder, but still conductive, gold coatings.

In my thesis the experimental part will be described first in Chapter 2, including the handling of air-sensitive samples, obtaining structure information and investigating chemical and physical properties. Followed by the preparative and structural studies of silver nitrides in Chapter 3, Ag_{3+x}N is found to adopt the perovskite structure with fully ($x = 1$) or partially ($0 < x < 1$) filled “A” site. For the preparation of such silver nitrides two different reactions with diluted gaseous NH_3 (in Ar) or alternatively concentrated aqueous ammonia have been used. Attempts for the preparation of ternary nitrides, e.g. silver copper nitride, have also been done, in which AgCuF_3 was used as the precursor.

Chapter 4 deals with AgCuF_3 and its isostructural analogue NaCuF_3 , which crystallize in a distorted variant of the GdFeO_3 -type structure with $P\bar{1}$ symmetry. They exhibit interesting magnetic properties, and become typical one-dimensional (1D) antiferromagnets at low temperature, related to a cooperative Jahn-Teller effect. Cs_2AgF_4 crystallizes in the K_2NiF_4 -type structure, and its magnetic and optical properties have been studied and explained in chapter 5. It behaves as a two-dimensional (2D) square-lattice Heisenberg ferromagnet, which is associated with orbital order.

CsF crystallizes in a rock-salt type structure, which contains larger cations and smaller anions. It has a strong tendency to form complex fluorides, and includes easily molecules like H_2O or Br_2 molecules at low temperatures, i.e. 70°C [26, 27]. We have studied the possibilities of the inclusion of tetrahedral molecules, e.g. OsO_4 and P_4 , into the CsF lattice, which will be discussed in chapter 6.

In the last part of my thesis, Chapter 7, structural studies have been performed on SiBr_4 (m.p. 278 K), the only tetrahedral EX_4 compound ($E = \text{C, Si, Ge, Sn, Pb}$; $X = \text{F, Cl, Br, I}$) for which the structural data has not been reported yet. The structures of two polymorphs of SiBr_4 , a high temperature phase ($P\bar{a}3$) and a low temperature phase ($P2_1/c$) have been experimentally determined from the refinements of X-ray and synchrotron powder diffraction data as well as single crystal diffraction data. The transition temperature and halogen-halogen interactions of the experimental and calculated structures are discussed.

Chapter 2

Experimental background

2.1 Preparative background

2.1.1 Treatment of reactants and products

Most of the chemicals used in this work are sensitive to air and moisture. Therefore, special techniques have to be utilized in order to protect them within an inert atmosphere and handle them for various reactions. Commercially available fluorides, like CsF and CuF₂, need to be pretreated first to get rid of the absorbed water by being heated up to at least 250°C under vacuum. Silver fluorides, i.e. AgF and AgF₂, are light- and air-sensitive, and no heat can be applied as they decompose into Ag at low temperatures ($\geq 90^\circ\text{C}$). OsO₄ is a highly volatile and oxidizing compound, therefore all manipulations should be carried out quickly under inert gas, e.g. argon, for protection. Similarly, white phosphorus is always kept in water and handled in argon because of its high volatility and reactivity in air. Silicon tetrabromide, liquid at ambient conditions, hydrolyzes readily when exposed to air with formation of HBr [28]. As a result, the preparation and treatment of these chemicals must be undertaken in a glove box or via the Schlenk technique [29].

Argon (99.996%, Messer-Griesheim) was used as a protection gas in the Schlenk technique, which was once dried over silica gel and a molecular sieve. Then any trace of oxygen and nitrogen was removed using an 800 °C hot titanium sponge. Any oxygen and water impurities left were finally eliminated with the catalyst containing Cr²⁺ in silica gel [30]. The evacuation was performed with a two-step rotary vane pump (Leybold-Heraeus, minimal vacuum 10⁻³ mbar) and a silicone diffusion pump (Leybold-Heraeus, minimal vacuum 10⁻⁶ mbar) with upstream liquid-cooling trap.

Glove boxes (M. Braun) were available for weighing the starting materials, looking for single crystals or sample preparation for the measurements of physical properties. It was filled with Argon (99.996%, Messer-Griesheim), which was dried through a molecular sieve and from which hydrogen was removed with a BTS catalyst (BASF).

The glove box was regularly checked for O₂ (< 0.05 ppm) and H₂O (< 0.1 ppm). Light-sensitive compounds, particularly AgF and AgF₂, have been kept in dark containers there.

2.1.2 Solid state reactions

For the reactions at temperatures between 500 and 650 °C Ar filled gold tubes and silica tubes were used as protection. In this temperature range the fluoride mixtures, Ag-Cu-F, Na-Cu-F and Cs-Ag-F, are inert to gold. The gold tubes were rinsed with water, petrol ether and ethanol before use. The ternary fluorides were prepared from the stoichiometric mixtures of reactants finely dispersed in a mortar in the glove box. Each mixture was made into pellet form and closed in a gold tube, which was then sealed in a silica tube under purified argon. The samples were heated to 500-650 °C at a heating rate of 50-100 °C/h, held for 0.5-4 days at a temperature, and cooled slowly down to room temperature at 30- 60 °C/h.

For the reactions at temperatures between 100 and 300 °C Duran glass ampoules were used. In this temperature range there is no reaction between the ampoules and the mixtures of CsF and selected tetrahedral molecules, i.e. OsO₄ and P₄. The Duran glass ampoules were rinsed with water and ethanol, and baked at 300 °C in dynamic vacuum for several hours before use. Finely dispersed mixtures of reactants in a certain ratio were weighed in the glove box and stored in Duran glass ampoules, which were sealed under purified argon. The ampoules were put into an oven (Heraeus T6, Germany) with target temperature 100-300 °C for 3-5 days. After the reaction, the ampoules were taken out and left to cool down at ambient conditions.

2.1.3 Solid-gas reactions

Nitrides, such as silver nitride, were synthesized using anhydrous binary or ternary fluorides as starting materials and gaseous NH₃ (99.98%, Westfalen Gas, Münster) as nitriding agent in the ammonolysis reactions. The setup consisted of four main parts: two gas delivery systems, a reactor and a vacuum system. Ammonia gas was first dried in one gas delivery system and then mixed with purified Ar gas (99.999%, from liquid Argon, Westfalen Gas) coming from the other gas delivery system. Both gases were controlled by mass flow controllers (Wagner) with certain flow rates. The mixed gas was then led into the reactor chamber, which is a silica tube (45 cm long, 2.5 cm internal diameter, Quarzschmelze Heraeus, Hanau) fitted in a home-made tube furnace. In each preparation,

ca. 0.1 g of the fluoride was first placed in an alumina boat (Friatec, 4.5 cm long) in the glovebox, which was then put into the above-mentioned silica tube. The target temperatures were reached within one hour under mixed flowing gases. At the end of each reaction, the products were cooled down to room temperature in the same atmosphere.

2.1.4 Storage of air-sensitive substances

All fluorides were stored in plastic bottles in the glove box. OsO₄ and SiBr₄ were kept in sealed glass bottles in the glove box. White phosphorus was preserved under water. Silver nitrides obtained from reaction were all kept either in water or in ethanol. The other nitrides were stored in plastic or glass vessels outside of the glove box.

2.2 Starting materials

Silver (I) fluoride (Chempur, 98%), silver (II) fluoride (Alfa Aesar, 99.5%), mercury (I) fluoride (Alfa Aesar, 97%), mercury (II) fluoride (Acros, 97%) were used as received. The following fluorides needed to be dried first: copper (II) fluoride (Alfa Aesar, 99.5%, dried in vacuum at 250 °C for 10 h), sodium fluoride (Chempur, 99.5%, dried in vacuum at 250 °C for 3 h) and cesium fluoride (Chempur, 99.5%, dried in vacuum at 500 °C for 1 h). All of the fluorides are kept in the glove box after pretreatment.

Palladium (II) chloride (ChemPur, 59.55% Pd), sodium azide (Merck, 99.9 %), gold (I) chloride (Aldrich, 99+%), gold (III) chloride (Acros, 99%) and mercury (II) oxide (Alfa Aesar, 99.9%) were used to obtain different nitrides. The two gold chlorides were handled in the glove box.

Osmium (VIII) oxide (chempur, 99.9%) was kept in the Duran ampoule in the glove box as received. For a reaction, it was weighed quickly based on a certain CsF : OsO₄ ratio and poured into a Schlenk tube, which was immediately closed.

All manipulations of white phosphorus were carried out using Schlenk technique or an argon-filled glove box. The approximate weight of white phosphorus, cut under water, was calculated by estimating its volume.

For the structure determination of SiBr₄, commercially available silicon (IV) bromide (Aldrich, 99.995%) was used as received and kept in the glove box. With Schlenk technique it was filled into glass capillaries ($\varnothing = 0.1, 0.2, 0.3$ or 0.5 mm), which were

cleaned with an acid mixture (HNO_3 (65%) : HF (40%) \approx 3:1), rinsed with water and ethanol, dried and heated at 150 °C.

2.3 Characterization and analysis

2.3.1 X-ray diffraction (XRD)

2.3.1.1 Powder XRD

The powder samples were characterized by means of XRD measurements, which were performed on a powder diffractometer STOE STADI P with $\text{CuK}\alpha_1$ radiation, $\lambda = 1.540598 \text{ \AA}$. Debye-Scherrer geometry was adopted by filling the samples into capillaries (normally $\varnothing = 0.3 \text{ mm}$) to protect them from oxidation and/or hydrolysis in air. Another option is to use flat samples that are non air-sensitive or not suitable for Debye-Scherrer geometry. Silicon (6N, $a_{\text{Si}} = 5.43102 \text{ \AA}$ at 298 K) was used as an external standard.

Phase purity was assessed from 30-min scans by referencing to powder diffraction patterns based on structural data from the Inorganic Crystal Structure Database (ICSD) or generated by the program PowderCell 2.4 [31].

2.3.1.2 Single crystal XRD

Single crystals, e.g. AgCuF_3 and SiBr_4 , were sealed under argon in a glass capillary for X-ray investigation. The diffraction data were collected using a STOE IPDS I image plate diffractometer with monochromatized $\text{AgK}\alpha$ radiation or a STOE IPDS II image plate diffractometer with monochromatized $\text{MoK}\alpha$ radiation.

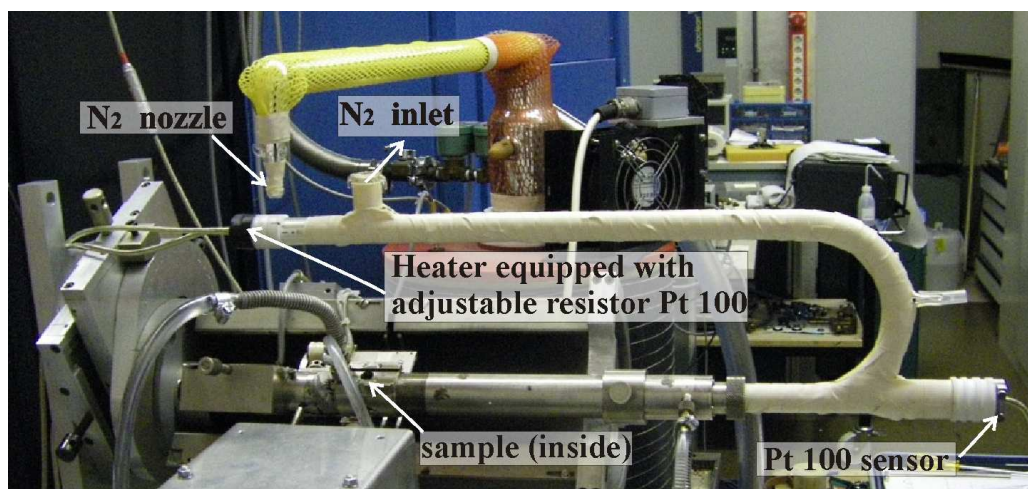


Figure 2.1 Simon-Guinier camera.

2.3.1.3 Temperature-dependent Simon-Guinier camera

Simon-Guinier camera [32] was used for temperature dependent X-ray analysis (see Figure 2.1). Typically, a sample was loaded into a glass capillary ($\text{\O} = 0.1, 0.2$ or 0.3 mm) under argon, approximately 5-8 mm length.

2.3.1.4 Energy-dispersive X-ray spectroscopy (EDX) and scanning electron microscope (SEM)

EDX was done with an Oxford Si-detector. Electron images were taken using a TESCAN 5130 MM SEM.

2.3.2 Neutron diffraction

Powder neutron diffraction was performed on polycrystalline samples on the high flux two-axis powder diffractometer D20 (see Figure 2.2 for an outline) at a wavelength of 2.4 \AA (high intensity, medium resolution) at Institut Laue-Langevin (ILL), Grenoble. Cylindrical hollow vanadium cans were used as sample holders to prevent contact with air, and indium wire was used for sealing.

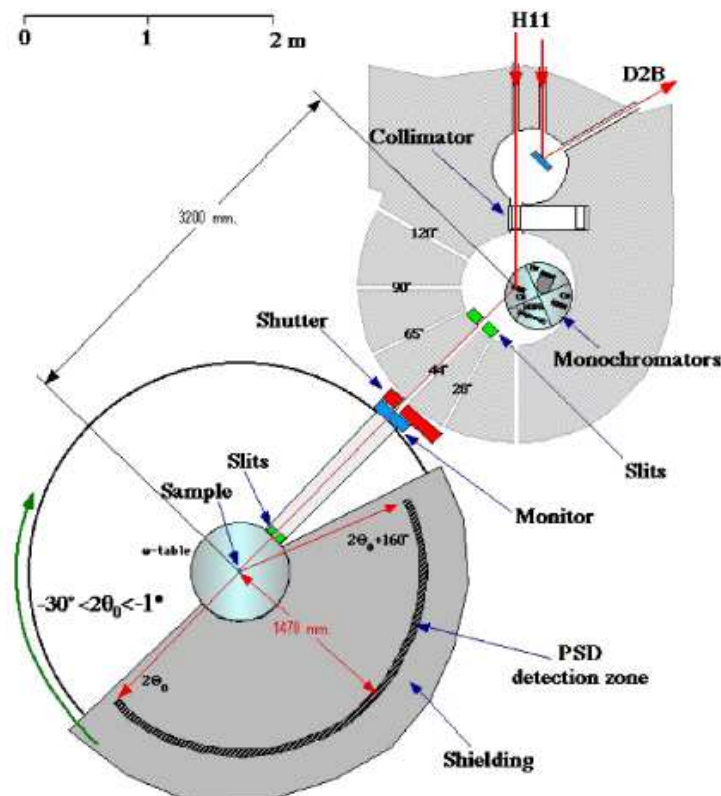


Figure 2.2 Experimental setup of D20 at the ILL [33].

2.3.3 Synchrotron diffraction

2.3.3.1 Synchrotron Powder diffraction

In-situ X-ray powder diffraction data of SiBr₄ at low temperature were collected in Debye-Scherrer geometry with a Cryostream 600 cold air blower (Oxford Cryosystems) on a motorized goniometer head at beamline X7B at the National Synchrotron Light Source (NSLS) at Brookhaven National Laboratory. X-rays of energy 13.5 keV were selected by a double flat crystal monochromator in ultra-high vacuum located 8 meters from the source. The size of the beam was adjusted to approximately 0.5 mm². As detector, a MAR 345 image plate reader was set up perpendicular to the beam path at a distance of approx. 227 mm from the sample. LaB₆ was used as an external standard to determine the beam center, sample-to-detector distance, exact wavelength ($\lambda = 0.92103$ Å), and tilting angle of the image plate. The sample, contained in a sealed lithium borate glass capillary with 0.5 mm diameter was aligned such that it was closest to the centre of the nozzle of the cold air blower at a distance of approx. 5 mm. It was immediately cooled to $T = 120$ K and slowly reheated back to room temperature ($T = 280$ K) in 70 min. During exposure, the sample was rocked by 60° in order to improve randomization of the crystallites. An exposure time of 60 seconds was chosen depending on the saturation intensity of the image plate. Together with a readout time of 80 seconds of the image plate reader, this led to a heating rate of 5.33 K/scan.

2.3.3.2 High pressure study

High pressure measurements were conducted at room temperature with a gasketed diamond anvil cell (DAC). Pressures are measured by the luminescence of a ruby crystal inserted into the pressure chamber. Monochromatic powder diffraction experiments were carried out at the ID09A beamline of the European Synchrotron Radiation Facility (ESRF), Grenoble, using a MAR345 image plate detector. The X-ray beam (wavelength $\lambda = 0.414246$ Å) is collimated to a nominal diameter of 30 µm. In order to improve powder averaging, the DAC is rocked by ± 3 degrees. The scanned two-dimensional diffraction patterns were corrected for tilt and scanner distortions and converted to intensity vs. 2θ data using the FIT2D software. Determination of peak positions, indexing, and refinements of lattice parameters were performed using the Fullprof program [34]. Liquid nitrogen was employed as a pressure transmitting medium (PTM).

2.3.4 Structure refinement

2.3.4.1 Rietveld refinement

Rietveld profile refinements for powders were carried out on the data using the Fullprof program [34]. The first step in these refinements was to execute a Le Bail extraction on the model-independent parameters. The Le Bail method is a peak extraction method using least squares to set the F_{calc} for each reflection as the F_{obs} value calculated in the previous cycle. This method was used to refine the background (manual background fitting was carried out), lattice parameters, wavelength, and the peak profile. The peak profile is described by a pseudo-Voigt function with mixed Gaussian and Lorentzian contribution. In the subsequent step, the Rietveld method was used to refine the model-dependent parameters, such as atomic positions, thermal parameters and atomic occupancy, being careful not to refine the occupancy and thermal parameters at the same time.

Alternatively, indexing of the powder pattern was performed in the program TOPASI [35] by iterative use of singular value decomposition (LSI) [36]. The crystal structure was solved by the global optimization method of simulated annealing in real space using the TOPAS program. The peak profiles and precise lattice parameters of the powder pattern were first determined by a Le Bail fit [37] using the fundamental parameter (FP) approach of TOPAS [38]. The crystal structure giving the best fit to the data was then validated by the Rietveld refinement using the TOPAS program.

2.3.4.2 Single crystal structure refinement

The starting atomic parameters, derived via direct methods using the program SIR 97 [39], were refined with the program SHELX-97 [40] (full-matrix least-squares on F^2 with anisotropic atomic displacement parameters for all atoms) within the WinGX program package [41].

2.3.5 Thermal properties

The specific heat of powder samples ($m \approx 20$ mg) were measured using a commercial Physical Property Measurements System calorimeter (Quantum Design, 6325 Lusk Boulevard, San Diego, CA.). To thermally anchor the powder to the specific heat platform, a minimal amount of Apiezon N grease was used. The specific heat of the

platform and the grease was determined in a separate run and subtracted from the total specific heat.

Differential Scanning Calorimetry (DSC) experiments are done using Pyris 1 DSC, Perkin Elmer. The sample holder is an aluminum crucible (also as the reference) with inner diameter 6.5 mm and depth of 2 mm. In case of fluoride samples, the powder was first put into a gold foil to avoid contact with the crucible.

The obtained ternary fluorides were studied with one of the institute-built Differential Thermal Analysis (DTA) devices (see Figure 2.3). This offers the possibility to record the absolute temperature and the thermal voltage difference (Hewlett Packard 3457A Microvoltmeter, Pt/PtRh thermocouples) at the same time with a compensation recorder. For one DTA measurement, typically a 15-25 mg sample held by a gold foil was weighed in the glove box. Then the foil was put into a Tantalum ampoule (15 mm long, $\text{\O} = 2$ mm), which was welded using a laser and bound to a thermocouple with the Pt wire with a standard substance (Au). The temperature of the DTA furnace was controlled in the range of 20-700 °C with an electronic temperature controller (Eurotherm, Pt/PtRh thermocouple). The thermal investigations were under argon with a heating or cooling rate of 3 °C/min.

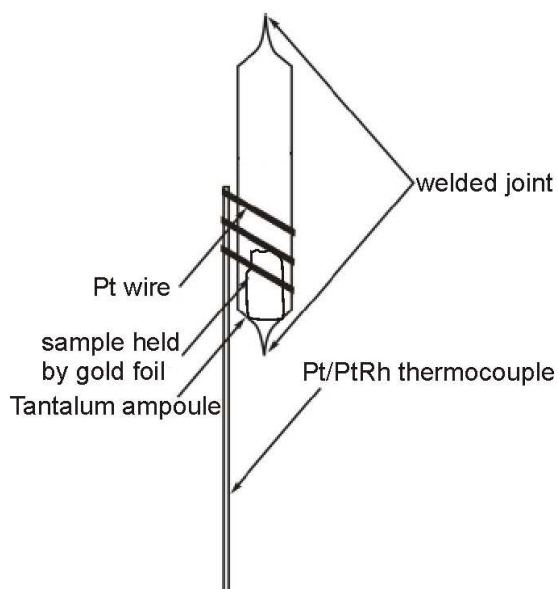


Figure 2.3 The DTA setup.

2.3.6 Magnetic properties

The magnetic susceptibility was measured as a function of temperature and magnetic field using a MPMS SQUID magnetometer (Quantum Design, 6325 Lusk Boulevard, San Diego, CA.).

Electron paramagnetic resonance (EPR) spectra were measured with a Bruker ER040XK microwave X-band spectrometer and a Bruker BE25 magnet equipped with a BH15 field controller calibrated against DPPH. A 100 kHz field modulation was used to record the first derivative of the signal intensity. The spectra were fitted to a resonance curve with Lorentzian line shape (zero dispersion) by varying the resonance position as well as the linewidth, intensity and background parameters.

Solid-state Nuclear magnetic resonance (NMR) spectra were obtained on a Bruker Avance DSX 400 (9.4T) spectrometer. ^{19}F MAS experiment spectra were recorded using a 2.5 mm double channel Bruker probehead, spinning at 25 kHz. ^{133}Cs experiments were acquired on a 4 mm double channel Bruker probehead, with a spinning rate of 8 to 10 kHz. Chemical shifts were referenced with respect to CaF_2 (set to 0 ppm) for.

2.3.7 Optical properties

Ultraviolet-visible (UV-Vis) diffuse reflectance measurements of Cs_2AgF_4 have been carried out using a Perkin-Elmer Lambda 19 UV/VIS/NIR spectrophotometer.

Raman spectra were taken with a Jobin Yvon Typ labram V 010 single grating spectrometer, equipped with a double super razor edge filter and a peltier cooled CCD camera. The spectra are taken in quasi-backscattering geometry using the linearly polarized 632.817 nm line of an He/Ne gas laser with power less than 1 mW, focused to a 10 μm spot through a 50x microscope objective on to the top surface of the sample. The measurement time for each sample has been 10 minute using several accumulations. The resolution of the spectrometer (grating 1800 L/mm) is 1 wavenumber (cm^{-1}).

2.3.8 Computations

The spin exchange parameters of ternary fluorides were estimated by performing a spin dimer analysis [42, 43] based on extended Hückel tight binding (ETHB) calculations [44] as well as mapping analysis [45-48] based on first principles density functional theory (DFT) electronic band structure calculations.

The crystal structures of SiBr_4 were predicted using the program CRYSCA [49] by global minimization of the lattice energy using force-field methods. In CRYSCA the energy is described as the sum of van der Waals and electrostatic terms.

Band structure calculations for binary nitrides were carried out in the framework of the local density approximation (LDA) [50] by using the Stuttgart TB-LMTO code [51].

Chapter 3

Structural and electrical properties of explosive silver nitrides

3.1 Introduction

Nitrogen has one of the highest electronegativities, only oxygen, fluorine and chlorine are higher, and as a consequence nitrides form a very large group of salt-like compounds. As mentioned in Chapter 1, Cu_3N represents an open cubic framework suitable for inclusion of other atoms. Another example is mercury nitride, which has been reported only in early 20th century as prepared from KNH_2 and Hg salts [52-54]. Its chemical components had been determined from elemental analysis as Hg_3N_2 .

Silver nitride, mentioned as Ag_3N , was first known as “fulminating silver” (Bertholletsches Knallsilber) two centuries ago. This explosive black solid can be obtained by adding silver oxide to aqueous ammonia [55, 56]. By addition of alcohol or acetone into the above ammoniacal solution or simply by heating it, silver nitride can also be prepared [57]. However, starting with silver oxide always leads to a silver nitride containing impurities of Ag and Ag_2O . Thereafter, J. Eggert found that adding absolute alcohol to the ammoniacal solution of silver oxide results in the precipitation of purer black silver nitride in a relatively short time [58]. Furthermore, Olmer and Dervin obtained the nitride free of Ag_2O but with some Ag from $\text{AgF}\cdot 2\text{NH}_3\cdot 2\text{H}_2\text{O}$ complex [59, 60]. From the ammoniacal solution of AgCl the same explosive solid can be produced as well when a solid strong base, such as KOH , is added [61, 62].

The first structural study of silver nitride was performed by Hahn and Gilbert in 1949 with a reported formula of Ag_3N [61]. The authors realized that there should be 4 Ag atoms in the unit cell according to the density measurement, and they reported a structure, which has a face-centered cubic (f.c.c.) unit cell with $Z = 4/3$ and $a = 4.369\text{\AA}$. Consequently, it was suggested that the Ag atoms are located at the corners and face centers of the unit cell, and no N atom positions were given, probably statistically distributed in the octahedral interstices [63]. According to Hahn and Gilbert, in contrast

to its black color, silver nitride can be described as an ionic compound according to the calculated N radius. In contrast, Luchs concluded that the connection has metal characteristics because of the similar lattice of metal Ag and the easily separated N as N₂ [64].

Here the results of our studies on silver nitride are discussed. We have used the synthetic method of Hahn and Gilbert. For the first time silver nitride powder was obtained by ammonolysis reaction with gaseous ammonia. Band structure calculations have been done for Ag₄N and Ag₃N. Furthermore, the ammonolysis reaction has also been applied in order to obtain nitrides of other noble metals, such as Pd, Au and Hg.

3.2 Experimental section

3.2.1 Silver nitride synthesis

Two methods were used for preparing silver nitride. Aqueous ammonia was the nitriding agent in the first method, while gaseous ammonia was used in the second one.

3.2.1.1 Aqueous ammonia route

AgF (Alfa Aesar, 99%) and AgCl are alternative starting materials. AgF was used without pretreatment. AgCl powder was synthesized by mixing anhydrous AgNO₃ (Merck, 99.8%) and aqueous HCl (Merck, 30%). The obtained AgCl and KOH pellets (Aldrich, 85%) were added into NH₃·H₂O (Alfa Aesar, 50%) to produce silver nitride [61]. This method was performed at both room temperature and 100 °C, and the product obtained is named “1”.

3.2.1.2 Gaseous ammonia route

Another way to produce silver nitride powder is the ammonolysis reaction, in which anhydrous AgF (Alfa Aesar, 99%) or AgF₂ (Alfa Aesar, 99.5%) were used as starting materials and gaseous NH₃ (99.98%, Westfalen Gas) is the nitriding agent. The setup was introduced in Chapter 2. The reactions were carried out at pre-determined temperatures and reaction durations as shown in Table 3.1. The products obtained with this method are named “2”.

3.2.2 Other nitrides

Cu_3N was synthesized from CuF_2 and NH_3 according to publications [10, 12]. The same setup for the gaseous ammonia route in 3.2.1.2 has been used as well as in attempts to obtain binary nitrides of other noble metals, i.e. Pd, Au and Hg.

PdCl_2 was used as the starting material for palladium nitride. Another method for synthesizing this nitride is through a solid state reaction route. A mixture of PdCl_2 and NaN_3 in a 1:2 molar ratio (total weight ~ 0.1 g) was finely ground in a glove box. The detail of such method was introduced in Chapter 2. For a binary nitride of gold, AuCl and AuCl_3 were used. HgF , HgF_2 and HgO were the starting materials for a mercury nitride.

PdCl_2 and CuF_2 as well as PdCl_2 and Cu_3N (as prepared in this work) were used for preparing a ternary nitride, i.e. copper palladium nitride. The same setup has been used to synthesize another ternary nitride, silver copper nitride, from AgCuF_3 , the preparation and the physical properties of which will be discussed in the next chapter.

3.2.3 Sample characterization

The product samples were characterized by means of powder XRD, Simon-Guinier camera, EDX, SEM and band structure calculations in the framework of the local density approximation [50].

3.3 Results

3.3.1 Silver nitride

3.3.1.1 Synthesis

When AgF was used for the preparation of silver nitrides via the aqueous ammonia route, the product always contained elemental Ag as a byproduct. Starting from AgCl at room temperature led to pure silver nitride, but at a temperature above 100°C , only Ag was obtained.

Through the gaseous ammonia route, i.e. the ammonolysis reaction, when the temperature was lower than 120°C and the concentration of NH_3 gas in Ar was lower than 2% as shown in Table 3.1, pure silver nitride was successfully obtained from AgF as the starting material. Ag was found to be the only product if pure NH_3 was used, obviously, because of its strong reducing ability. When AgF_2 was used instead, no silver

nitride has been observed, no matter pure or diluted NH₃ (in Ar) was used. Pure elemental Ag was obtained when diluted NH₃ was used at 120 °C.

Table 3.1 The synthetic conditions and products from ammonolysis reactions of silver fluorides via the gaseous ammonia route.

Starting material	Nitriding agent	Preparation conditions	Product
	NH ₃	150°C 24h	Ag
	NH ₃	120°C 36h	Ag
AgF	2% NH ₃ / 98% Ar ^a	120°C 3h	impure Ag _{3+x} N
	5% NH ₃ / 95% Ar ^b	110°C 3h	Ag
	2% NH ₃ / 98% Ar ^a	100°C 2h	Ag _{3+x} N
AgF ₂	NH ₃	145°C 20h	impure Ag
	NH ₃	120°C 15h	impure Ag
	2% NH ₃ / 98% Ar ^a	120°C 12h	Ag
	2% NH ₃ / 98% Ar ^a	120°C 3h	Ag

^a The flowing rates of NH₃ and Ar are 10 ml/min and Ar 490 ml/min, respectively, same for below.

^b The flowing rates of NH₃ and Ar are 15 ml/min and 285 ml/min, respectively.

The obtained black powder samples from both methods are explosive when touched with hard objects. They are extremely sensitive when dry, even with a tension from a drop of water, but relatively easy to handle under water or ethanol. Silver nitride samples even slowly decompose at room temperature. They explode at temperatures above 165 °C in air or even under Ar. In agreement with this finding, if the reaction temperature goes beyond 160 °C in the ammonolysis reaction, the explosion of a 0.1 g sample can even break a silica tube of 2 mm thickness. Therefore, the obtained nitride is protected either in water or in ethanol as shown in Figure 3.1.



Figure 3.1 Silver nitride under water.

3.3.1.2 Structure determination

All XRD data sets were indexed on the basis of a cubic unit cell with the same cell parameters: $a = 4.3 \text{ \AA}$ (CuK α radiation). Flats were used for the XRD measurements since the silver nitride is very sensitive and difficult to fill into a capillary. The exposure time is set to 30 min in order to avoid slow decomposition. Depending on the syntheses methods, products with distinct silver contents have been obtained. The XRD patterns of the two different Ag nitride samples are shown in Figure 3.2. The determination of x in the molecular formula of Ag_{3+x}N is shown in Table 3.2.

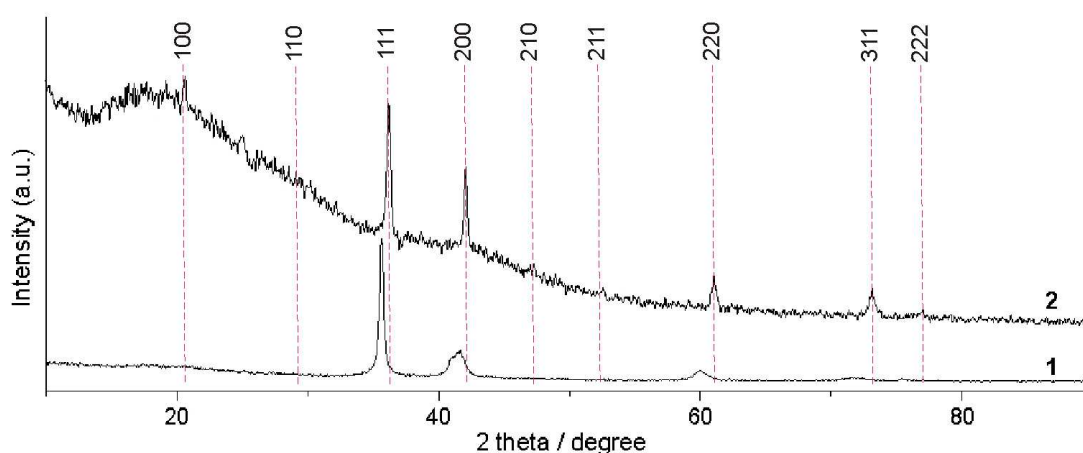


Figure 3.2 Experimental XRD patterns of the silver nitride **1** (aqueous ammonia route) and **2** (gaseous ammonia route). The vertical dashed lines correspond to the theoretical position of diffraction peaks of the silver nitride with $a = 4.29 \text{ \AA}$ (by Powdercell 2.4 [31]).

The Rietveld refinements using the Fullprof program [34] were not successful because of too few reflections in the XRD patterns. Therefore, we used the program STOE Win XPOW [65] to index and refine cell parameters with an initial Cu_4N -type structure with space group $Pm\bar{3}m$ (No. 221) [66]. Simulations with the program Powdercell [31] were carried out to visually estimate the occupation factor for Ag2 locating at the center of the unit cell by comparing the peak intensity of 100 and 111. The observed and calculated XRD data of the silver nitride for the refined model are illustrated in Figure 3.3.

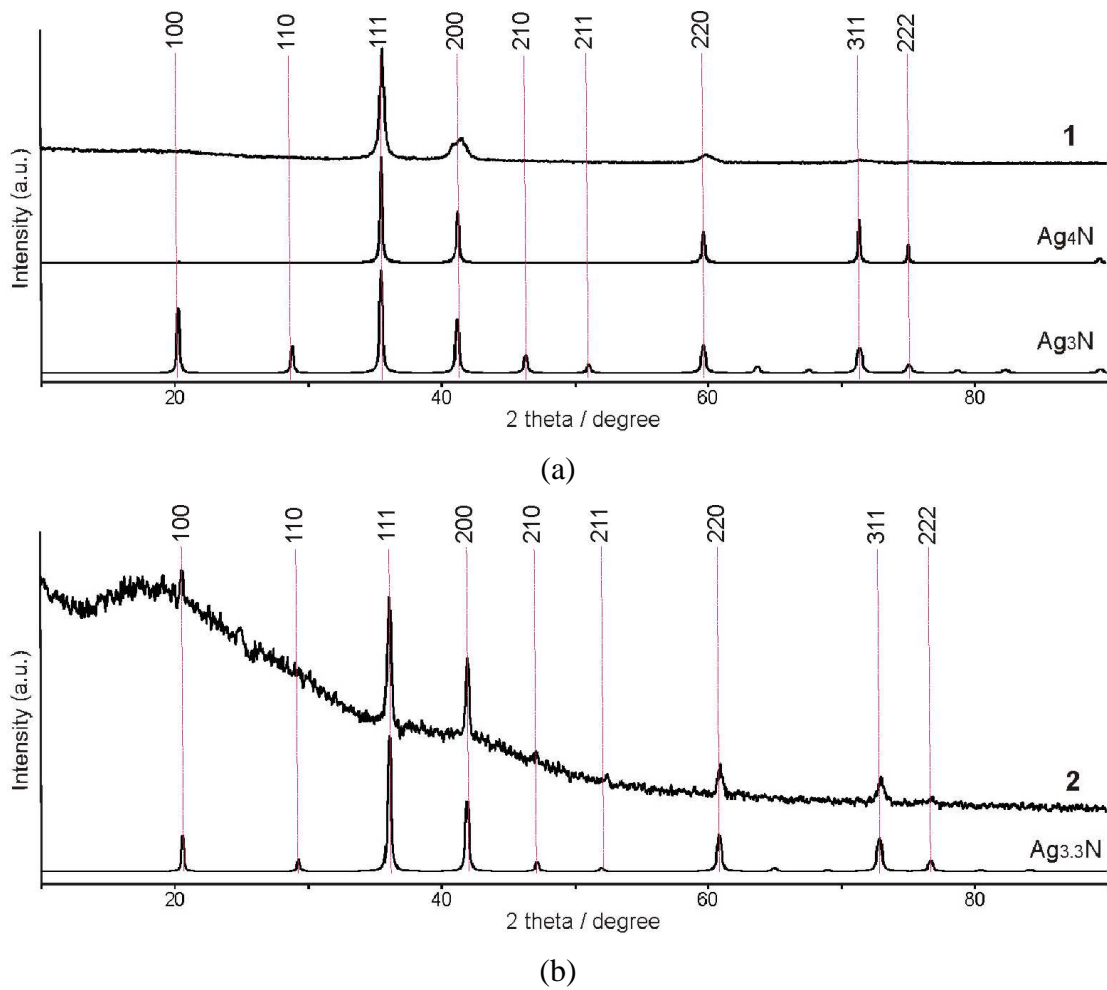


Figure 3.3 Observed and calculated X-ray diffraction patterns of the silver nitride. (a) From top to bottom: sample **1** (observed), Ag_4N and Ag_3N (the latter two calculated with $a = 4.35 \text{ \AA}$); (b) from top to bottom: sample **2** (observed), $\text{Ag}_{3.3}\text{N}$ (calculated with $a = 4.29 \text{ \AA}$). Powdercell was used for the calculation, with Ag2 occupation factor of 0, 0.3 and 1, respectively. The vertical dashed lines correspond to the theoretical position of diffraction peaks of the silver nitride.

The syntheses of **1** and **2** were repeated several times under the same conditions, and similar lattice parameters for each have been obtained. A brief comparison is listed in Table 3.2. All the silver nitrides obtained from aqueous ammonia have a full occupation at the Ag2 position, and the lattice parameter varies in the range of 4.34 and 4.38 Å. The silver nitrides obtained from gaseous ammonia have much less occupation at the Ag2 position, e.g. 0.2-0.3, and the indexed lattice parameter is smaller, which is in the range of 4.28 and 4.30 Å

Table 3.2 Comparison of the cell parameters of different batches of silver nitride for a general molecular formula of Ag_{3+x}N .

1		2	
a^a	x^b	a^a	x^b
4.363(5)	1	4.289(1)	0.3
4.377(7)	1	4.285(2)	0.3
4.351(7)	1	4.294(2)	0.2
4.345(2)	1	4.303(2)	0.3

^a Cell parameter a is indexed and refined in STOEF.

^b The approximate Ag2 occupation in unit cell is obtained by comparing peak intensity of 100 and 111 in Powdercell.

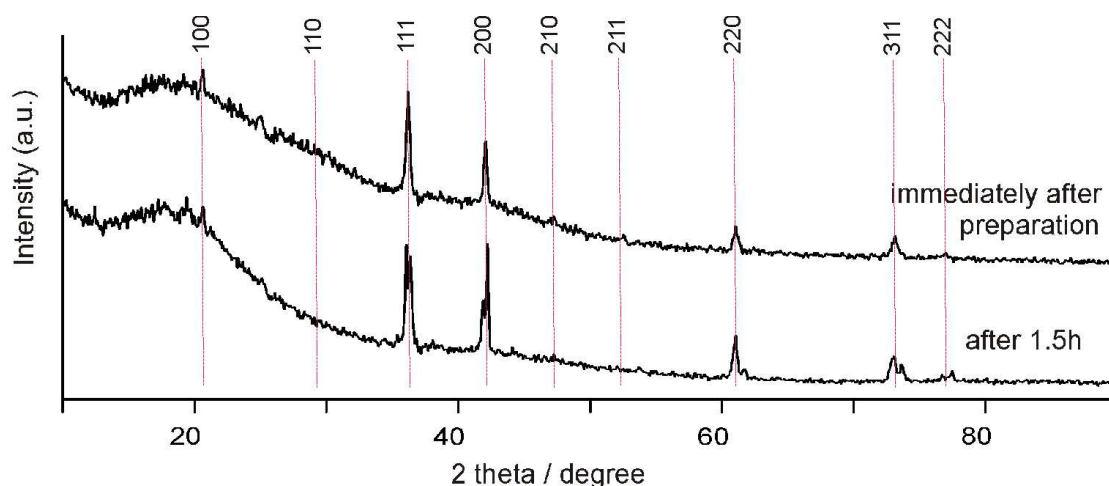


Figure 3.4 Comparison of the observed X-ray diffraction data for the same batch of silver nitride **2** at different time after preparation. The vertical dashed lines correspond to the theoretical position of diffraction peaks of the silver nitride.

Figure 3.4 shows the observed X-ray diffraction pattern for the same batch of **2** at different time after preparation. Peak splitting was found in the X-ray diffraction pattern for silver nitride **2** at room temperature after exposure in air for more than 1.5 hours. Each single peak in the pattern measured freshly after preparation splits into double peaks in the whole 2θ range. Obviously at room temperature a phase separation into more Ag-rich and Ag-poor silver nitrides takes place, in agreement with the well-known mobility of Ag^+ in solids [67].

3.3.1.3 LDA calculations

The electronic band structures for the two limiting cases, Ag_3N and Ag_4N , are shown in Figure 3.5. According to the calculations Ag_3N is an insulator with a band gap close to 1.35 eV, whereas Ag_4N is metallic.

The $\text{Ag}(0)$ occupying the center of the unit cell leads to the formation of the metallic Ag_4N from the insulating Ag_3N . In both band structures, the valence bands below the Fermi level are similar rigid bands. The conduction band with lowest energy in Ag_3N has moved towards the Fermi level in Ag_4N , and there is an additional band appearing above this band. The conduction band of Ag_4N exhibits strong hybridization among $\text{Ag}2\text{-s}$ and $\text{Ag}1\text{-}e_g$, in which $\text{Ag}2$ is the zero-valence $\text{Ag}(0)$ at the center of the unit cell (Figure 3.6).

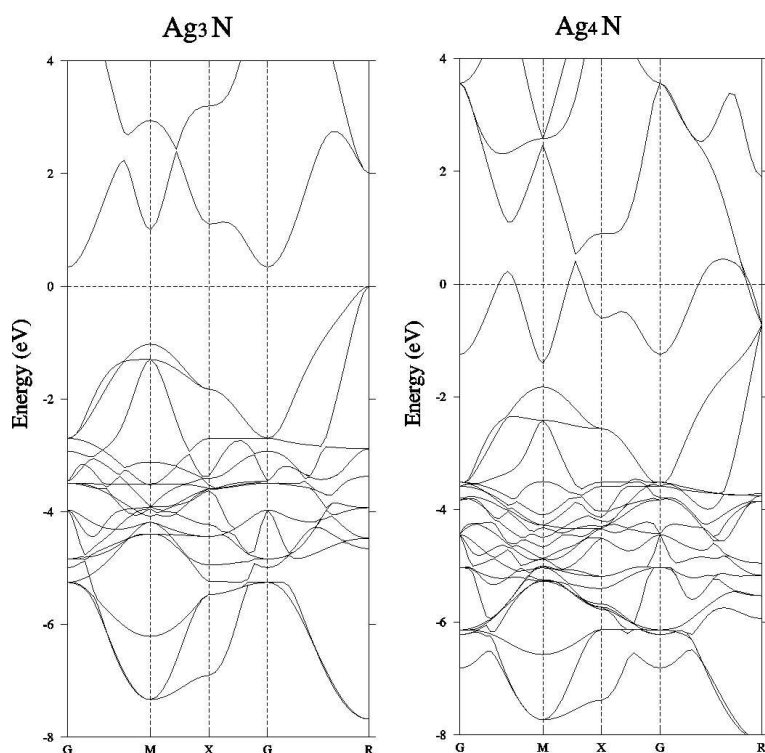


Figure 3.5 Electronic band structures of Ag_3N and Ag_4N . Horizontal line is the Fermi level.

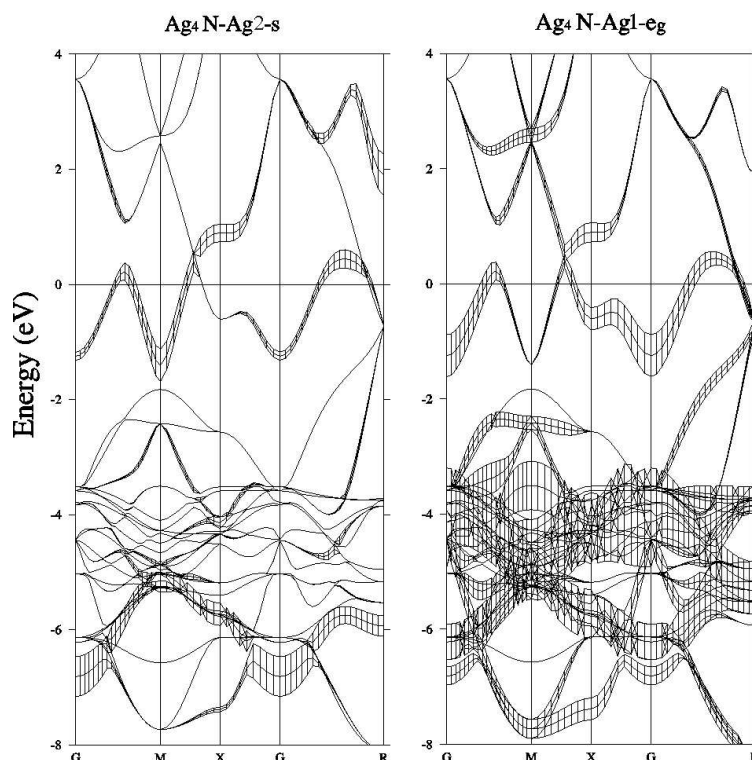


Figure 3.6 Comparison of the contribution of different orbitals to the conduction band of Ag_4N . Ag_2 is the $\text{Ag}(0)$ at the center of the unit cell. Horizontal line is the Fermi level.

Table 3.3 The synthetic conditions and products from the ammonolysis reactions for Cu_3N .

No.	Reactant	Gas	T (°C)	Time (h)	Product(s)
1	CuF_2	NH_3	150	24	CuF_2
2	CuF_2	NH_3	160	24	CuF_2
3	CuF_2	NH_3	170	24	CuF_2 (main)+ Cu_3N
4	CuF_2	NH_3	180	24	Cu_3N (main)+ CuF_2
5	CuF_2	NH_3	180	96	Cu_3N (main)+ CuF_2
6	CuF_2	NH_3	200	24	Cu_3N (main)+ CuF_2
7 [11]	CuF_2	NH_3	250	3	Cu_3N
8 [10]	CuF_2	NH_3	280	3	Cu_3N

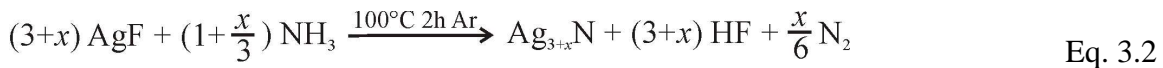
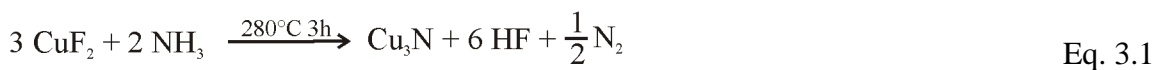
3.3.1.4 Copper nitride

The synthesis of Cu_3N was reported by Juza and Hahn for the first time from ammonolysis reactions at 280 °C for 3 hours [10]. Recently it was found by Paniconi that this can be done at a temperature as low as 250 °C [11]. In order to find temperatures

suitable for preparing ternary copper nitrides, such ammonolysis reactions for Cu₃N are investigated at even lower temperature, i.e. 150 °C < T < 200 °C. The results are shown in Table 3.3. At a temperature below 170 °C CuF₂ remained unchanged after 24-hour reaction. Cu₃N became the main product at a temperature higher than 180 °C. Extending the reaction time or increasing temperature to 200 °C will not complete the nitrating reaction, and the reaction product contains always unreacted CuF₂.

3.3.1.5 Discussion

The reactions for producing copper nitride and silver nitride can be written as the following equations, respectively,



It shows in Eq. 3.1 that all the Cu(II) in CuF₂ is reduced to Cu(I) during the nitrating reaction. However, starting with AgF, such reaction took place in a different way. As shown in Eq. 3.2, part of Ag(I) remains unreduced to form the same open framework as the Cu(I) in Cu₃N, whereas only the left *x* part of the Ag(I) is reduced to zero-valent Ag, which occupies the center of the unit cell in Ag_{3+x}N.

The obtained silver nitrides prepared by both methods have a general analytical formula Ag_{3+x}N. The experimental XRD patterns in Figure 3.2 show that the unit cell of sample **1** is larger than of sample **2**. The lattice parameters for silver nitrides given in Table 3.2 show the dependence on the preparative conditions. Via the concentrated aqueous ammonia route, the obtained black silver nitride (sample **1**) shows a powder pattern with vanishing reflections 100 and 110, resulting from an f.c.c. Ag packing. Ag₄N crystallizes in the M₄N-type structure (*M* = Fe, Mn, Co, Ni, Cu) with a preferred orientation along the [111] direction. The cell parameters are similar for the same method and the calculated values are between 4.34 and 4.38 Å.

On the other hand, a pure Ag_{3+x}N (sample **2**) with 0.2 < *x* < 0.3 was obtained by the reaction between AgF and diluted NH₃ in Ar at 100°C. There are no vanished 100 and 110 reflections in this case. The cell parameters are significantly different for these nitrides varying from 4.28 to 4.31 Å, which is ~2% less than those of the sample **1**.

The Ag₄N structural model is shown in Figure 3.7 according to the atomic coordinates listed in Table 3.4. In the M₄N-type structure displayed in Figure 3.7(a), one Ag atom is located on the cell edge, and another Ag atom lies at the center of the unit cell, while all

N atoms are at the cell corners. As shown in Figure 3.7(b), when half of the unit cell is shifted along any of the a , b or c directions, a f.c.c. unit cell for the Ag atoms will be obtained for Ag_4N with $Z = 1$ with all the N atoms in part of the octahedral voids as described in the literature [61].

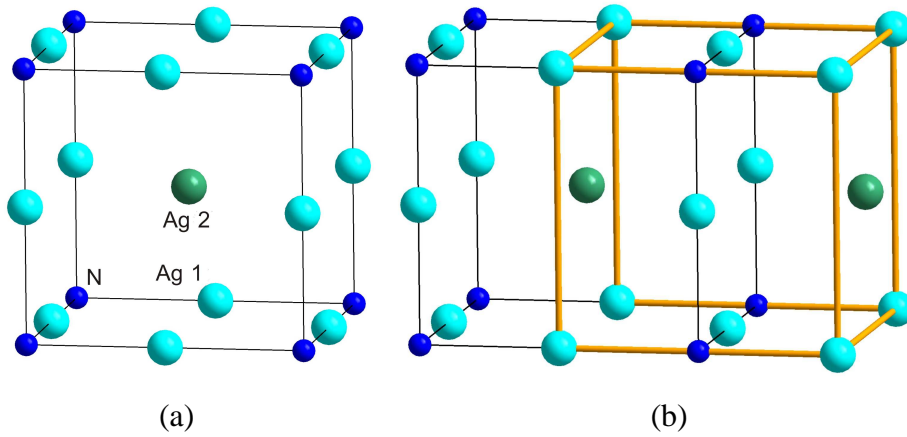


Figure 3.7 Unit cell of Ag_4N used for indexing. (a) The structure with the atomic positions following Figure 3.7 with the formula of $(\text{Ag}2)\text{N}(\text{Ag}1)_3$. (b) Shifting half of the unit cell along one of the cell axes, an f.c.c. cell for the Ag atoms is obtained.

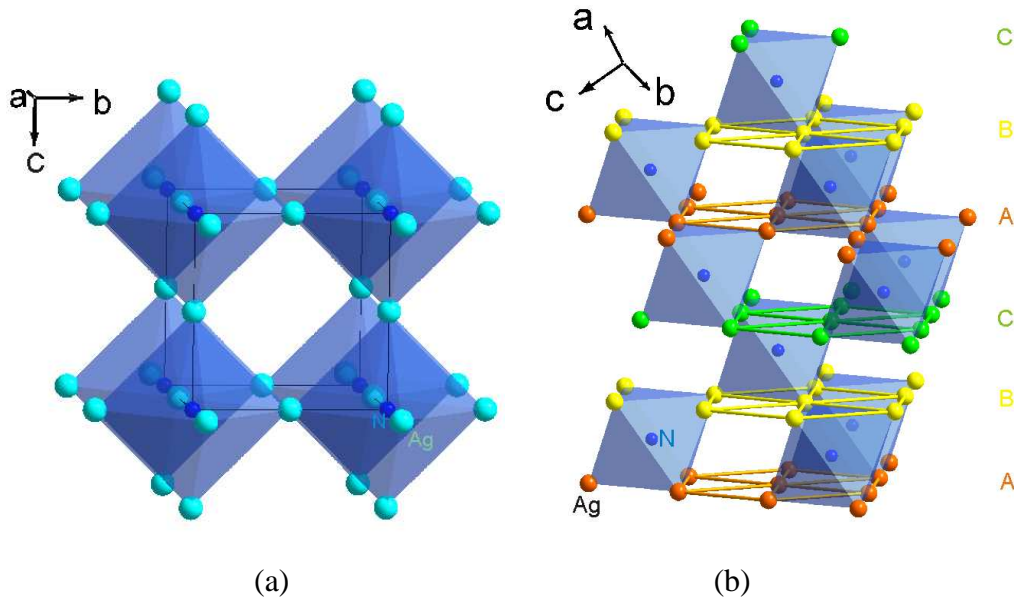


Figure 3.8 Comparison of the atomic arrangements in Ag_3N and Ag_4N : (a) open-framework Ag_3N with partially close packed silver; (b) Ag_4N described by a cubic sequence $|\text{ABC}|$ of close packed silver atom layers with analogous octahedra. Small blue spheres represent N atoms, and big spheres with all other colors represent Ag in different layers.

Table 3.4 Atomic coordinates for Ag₄N.

Site	Atom	<i>x</i>	<i>y</i>	<i>z</i>
3d	Ag1	1/2	0	0
1b	Ag2	1/2	1/2	1/2
1a	N	0	0	0

The structures of the two different silver nitrides, i.e. Ag₃N and Ag₄N, are illustrated in Figure 3.8. The open-framework Ag₃N contains corner sharing Ag₆N octahedra with Ag forming a partial cubic close packing (c.c.p.). In contrast, the silver atoms in the structure of Ag₄N show the motif of a c.c.p., and all nitrogen atoms occupy the corner-sharing octahedra. All the silver atoms have two nitrogen neighbors. A cubic sequence |ABC| of close packed silver layers are marked in different colors with inter-layer Ag₆N octahedra displayed in Figure 3.8 (b).

The interatomic distances in Ag₄N ($a = 4.363 \text{ \AA}$) and Ag_{3.3}N ($a = 4.289 \text{ \AA}$) are given in Table 3.5. Compared to f.c.c. Ag, the Ag-Ag distance in Ag₄N is increased by 7.1%. Compared to Ag₄N, in Ag_{3.3}N the amount of the body-centered Ag2 is reduced, which leads to a slight shrinking of the unit cell with the distances $d(\text{Ag-Ag})$ of $12 \times 3.0330 \text{ \AA}$.

Table 3.5 Cell parameters and interatomic distances (\AA) for Ag₄N and Ag_{3.3}N, with f.c.c. Ag for comparison.

	Ag	Ag ₄ N	Ag _{3.3} N
space group	$Fm\bar{3}m$	$Pm\bar{3}m$	$Pm\bar{3}m$
<i>a</i>	4.086	4.363(5)	4.289(1)
Ag1-Ag1	12×2.8889	8×3.0851^a	8×3.0330
Ag1-Ag2		4×3.0851	4×3.0330
Ag1-N		2×2.1815	2×2.1446
Ag2-N		8×3.7785	8×3.7146
N-N		6×4.3630	6×4.2893

^aNo error is given because no structural refinement is done.

3.3.2 Efforts to synthesize other binary nitrides

3.3.2.1 Palladium nitride

Our approach of ammonolysis reactions from PdCl₂ has been done in a temperature range between 200 and 350 °C (ranks 1-5 in Table 3.6). Above 250 °C PdCl₂ is reduced to Pd with diluted NH₃ (~1% in Ar). At T > 300 °C, the reaction is complete with Pd as the only product.

As another approach, we have performed metathetic solid state reaction of NaN₃ and PdCl₂ to synthesize a nitride of Pd. The XRD results showed that the exchange reaction resulted in the products Pd and NaCl, wherein obviously a reduction has taken place (ranks 6-8 in Table 3.6).

Table 3.6 The syntheses of palladium nitride from the ammonolysis reactions. .

No.	Reactant(s)	Gas	T (°C)	Time (h)	Product(s)
1	PdCl ₂	NH ₃ 4 ml/min / Ar 400 ml/min	200	4	NR*
2	PdCl ₂	NH ₃ 4 ml/min / Ar 400 ml/min	225	4	NR
3	PdCl ₂	NH ₃ 4 ml/min / Ar 400 ml/min	250	4	Pd+ PdCl ₂
4	PdCl ₂	NH ₃ 4 ml/min / Ar 400 ml/min	300	5	Pd
5	PdCl ₂	NH ₃ 15 ml/min / Ar 150 ml/min	350	5	Pd
6	NaN ₃ +PdCl ₂ (2:1)	Ar in silica tube	200	48	Pd+NaCl (incomplete)
7	NaN ₃ +PdCl ₂ (2:1)	Ar in silica tube	300	48	Pd+NaCl
8	NaN ₃ +PdCl ₂ (2:1)	Ar in silica tube	500	2	Pd+NaCl

*NR stands for No Reaction, same for below.

3.3.2.2 Gold nitride

Despite many efforts to obtain Au_xN, only recently gold nitride has been made on the surface of gold films by Šiller et al. [9]. In analogy to our studies for Ag nitrides, here we tried the reactions between gold chlorides and diluted gaseous ammonia. As shown in Table 3.7, either the reducing conditions are too strong or the temperatures are too high, as a result Au metal is the only reduced product.

There was no reaction found at 110 °C with 5% NH₃ in Ar when AuCl was the starting material. If the temperature was increased to 150 °C, Au was found to be the only

product. When AuCl₃ was used instead, similar results have been observed. The reactions took place at temperatures higher than 160 °C with Au metal as the only reduced product. If the concentration of NH₃ in Ar was decreased from 5% to 1%, it required higher temperature or longer duration to complete the reaction.

Table 3.7 The synthetic conditions and products from the ammonolysis reactions for gold nitride.

No.	Reactant	Gas	T (°C)	Time (h)	Product(s)
1	AuCl	NH ₃ (~5%) /Ar	110	3	NR*
2	AuCl	NH ₃ (~5%) /Ar	150	3	Au
3	AuCl ₃	NH ₃ (~5%) /Ar	100	3	NR
4	AuCl ₃	NH ₃ (~5%) /Ar	140	3	NR
5	AuCl ₃	NH ₃ (~5%) /Ar	160	3	Au
6	AuCl ₃	NH ₃ (~1%) /Ar	170	3	Au+AuCl ₃
7	AuCl ₃	NH ₃ (~5%) /Ar	180	3	Au

*NR stands for No Reaction, same for below.

Table 3.8 The synthetic conditions and products from the ammonolysis reactions for mercury nitride.

No.	Reactant	Gas flow (ml/min)	T (°C)	Time (h)	Product(s)
1	HgF	NH ₃ 15	200	6	HgF ₂ (NH ₃) ₂ +Hg
2	HgF	NH ₃ 5 (5%) / Ar 95	200	6	NR
3	HgF	NH ₃ 10 (20%) / Ar 40	200	6	HgF ₂ (NH ₃) ₂ +Hg
4	HgF ₂	NH ₃ 15	300	12	HgF ₂ +Hg
5	HgF ₂	NH ₃ 15	400	12	Hg
6	HgO	NH ₃ 15	250	6	Hg
7	HgO	NH ₃ 15	350	6	Hg

3.3.2.3 Mercury nitride

Again in analogy to the syntheses of Cu₃N and Ag nitrides, mercury fluorides and oxide are used as raw materials to prepare a mercury nitride (Table 3.8). When the flow rate of ammonia, pure or diluted in Ar, was more than 10 ml/min, HgF₂(NH₃)₂ and Hg were obtained as the products from HgF at 200 °C.

When HgF_2 was used instead (ranks 4 and 5 in Table 3.8), higher temperature was needed for the same reaction. At 400 °C the fluoride was reduced completely into elemental Hg. Similar results were observed for HgO with lower temperature.

3.3.3 Efforts to synthesize ternary copper nitrides

3.3.3.1 Silver copper nitride

Silver copper nitride is unknown until now, and only copper nitride films deposited with Ag by reactive magnetron sputtering have been reported recently [68].

In order to find a proper temperature for this ternary nitride the synthesis temperatures of the respective binary nitrides, i.e. Ag_4N and Cu_3N , have been investigated. Silver nitride can be obtained at 100 °C after two-hour reaction with diluted NH_3 and it is unstable when heated to around 165 °C. The lowest temperature for preparing Cu_3N is 180 °C, and after 3 days the reaction was still incomplete. There exists no crossover of the reaction temperature for Ag_4N and Cu_3N , thus no hint for the possible preparative temperature for the silver copper nitride could be gained in this way.

Table 3.9 The synthetic conditions and products from the ammonolysis reactions of AgCuF_3 .

No.	Gas	T (°C)	Time (h)	Product
1	NH_3	160	24	$\text{Ag}+\text{Cu}_3\text{N}$
2	NH_3	180	24	$\text{Ag}+\text{Cu}_3\text{N}$
3	NH_3	200	48	$\text{Ag}+\text{Cu}_3\text{N}$
4	$\text{NH}_3(\sim 2\%) / \text{Ar}$	120	2	No reaction
5	$\text{NH}_3(\sim 2\%) / \text{Ar}$	150	2	No reaction
6	$\text{NH}_3(\sim 2\%) / \text{Ar}$	200	3	No reaction
7	$\text{NH}_3(\sim 2\%) / \text{Ar}$	210	3	$\text{Ag}+\text{Cu}_3\text{N}+ \text{AgCuF}_3$
8	$\text{NH}_3(\sim 2\%) / \text{Ar}$	225	3	$\text{Ag}+\text{Cu}_3\text{N}+ \text{AgCuF}_3$
9	$\text{NH}_3(\sim 2\%) / \text{Ar}$	250	3	$\text{Ag}+\text{Cu}_3\text{N}$

The ammonolysis reactions to prepare silver copper nitride have been carried out in the temperature range of 120 to 250 °C. As shown in the first three rows in Table 3.9, AgCuF_3 was reduced by pure NH_3 to Ag and Cu_3N at 160°C. In order to decrease the reducing ability of NH_3 , a mixture of NH_3 and Ar was used as the nitriding agent. Below

200 °C no reaction took place. By further increasing the temperature to 210 °C, Ag and Cu₃N were observed again as the products with an incomplete transformation in 3 hours. The reaction has been found complete at 250 °C after 3 hours, and the XRD pattern of the product is shown in Figure 3.9. It is therefore concluded that silver copper nitride is unlikely to be obtained in the ammonolysis reactions from AgCuF₃ via gaseous NH₃ route.

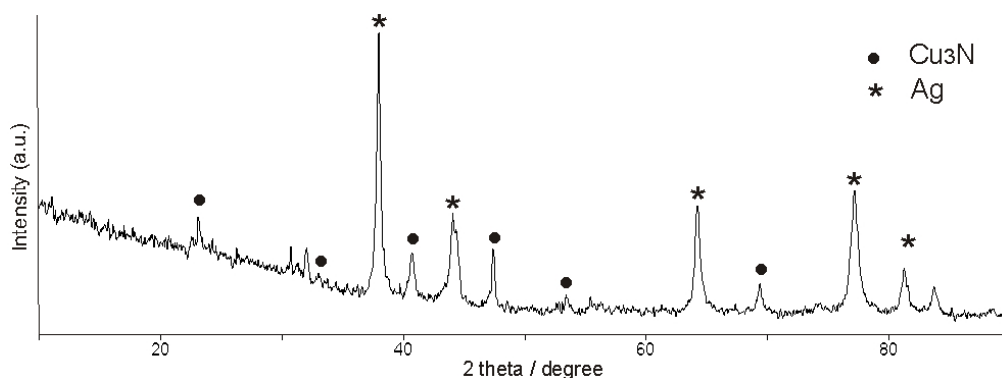


Figure 3.9 The XRD pattern of the products of the ammonolysis reaction of AgCuF₃ with diluted NH₃ at 250 °C. The Bragg reflections marked with “.” indicate Cu₃N, “*” Ag. Remaining reflections are from unreacted AgCuF₃.

Table 3.10 The synthetic conditions and products from the ammonolysis reactions for copper palladium nitride.

No.	Reactant	Gas flow (ml/min)	T (°C)	Time (h)	Product(s)
1	PdCl ₂ +CuF ₂ (1:3)	NH ₃ 15 (5%) / Ar 285	200	12	CuCl (incomplete)
2	PdCl ₂ +CuF ₂ (1:3)	NH ₃ 4 (1%) / Ar 396	240	3	CuCl+Pd (main)+ CuF ₂ (incomplete)
3	PdCl ₂ +CuF ₂ (1:3)	NH ₃ 8 (2%) / Ar 392	240	12	CuCl +CuF ₂ (main) + Pd (incomplete)
4	PdCl ₂ +CuF ₂ (1:3)	NH ₃ 15 (5%) / Ar 285	250	4	CuCl+Pd
5	PdCl ₂ +CuF ₂ (1:3)	NH ₃ 15 (5%) / Ar 285	300	12	Elements of Cu, Pd and Cl detected*
6	PdCl ₂ +CuF ₂ (1:3)	NH ₃ 15	300	12	Elements of Cu, Pd and Cl detected*
7	PdCl ₂ +CuF ₂ (1:3)	NH ₃ 4 (1%) / Ar 396	600	16	CuPd

* From EDX measurements.

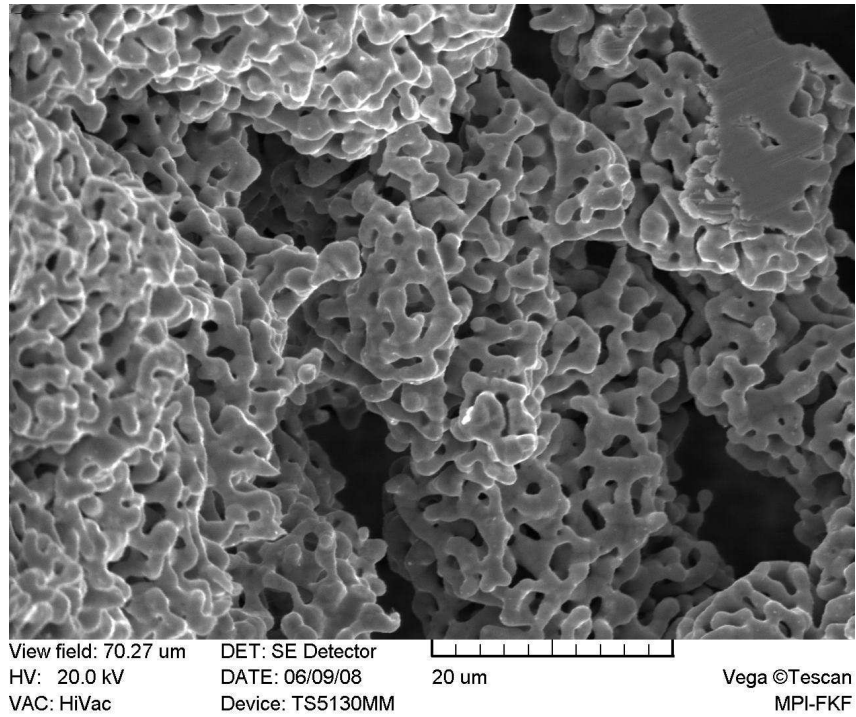
3.3.3.2 Copper palladium nitride

$\text{Cu}_3\text{Pd}_x\text{N}$ ($x = 0.020$ and 0.989) have been obtained by ammonothermal reaction of $[\text{Cu}(\text{NH}_3)_2]\text{NO}_3$ and $[\text{Pd}(\text{NH}_3)_4](\text{NO}_3)_2$ [6]. Table 3.1 shows the results of the attempts to obtain corresponding copper palladium nitrides from ammonolysis reactions. Since PdF_2 is not commercially available, PdCl_2 was used instead. When the temperature was below $250\text{ }^\circ\text{C}$, CuCl and Pd were obtained from a mixture of PdCl_2 and CuF_2 reacted with diluted NH_3 (1-5% in Ar, see ranks 1-4 in Table 3.10), and the reaction was not complete. According to XRD and EDX results, there is ammonia chloride composite in the product when the temperature is higher than $300\text{ }^\circ\text{C}$. Furthermore, at $600\text{ }^\circ\text{C}$, both metals ions are reduced to form the CuPd intermetallic compound, the SEM images of which are shown in Figure 3.10. It appears in a sponge shape with a multiporous structure, with the pores in micrometer scale. Obviously the reducing conditions are high enough to produce Pd metal in contrast to the ammonothermal reaction conditions.

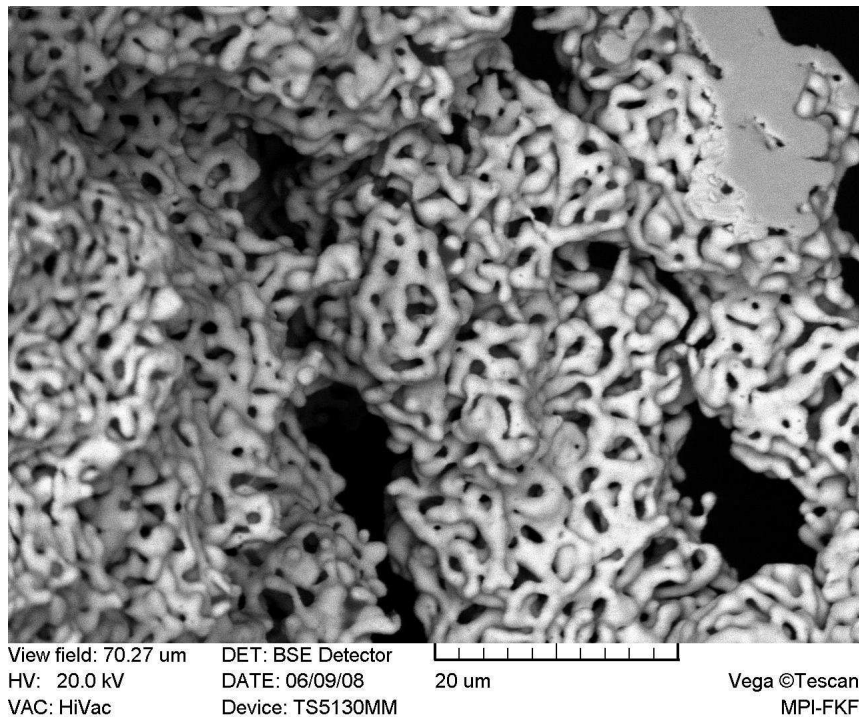
3.4 Discussion

Copper nitride and silver nitride can be obtained from pure NH_3 and diluted NH_3 respectively, while the nitrides of Pd , Au and Hg could not be obtained via the same route. There are many factors, which have influences on the formation of nitrides, including preparation temperatures and time, nitriding agents, atom sizes, atom electronegativity and so on. With the similar preparation condition, the electronegativity values of the noble metals using Pauling scale [69] provide the insight into the experimental results. Hg has the electronegativity of 2.00, slightly higher than Cu (1.90) and Ag (1.93), and the electronegativity of Pd and Au are even higher, 2.20 and 2.54, respectively. This demonstrates a possible reason why in the ammonolysis reaction for Pd , Au and Hg salts elemental metals were easily obtained.

As for ternary copper nitrides, the difference in the electronegativities of the two transition metals could be one of the reasons responsible for not forming a ternary nitride. In the case of silver copper nitride, the distinct reaction schemes of forming the individual binary nitrides might give a hint for the formation of elemental Ag .



(a)



(b)

Figure 3.10 The SEM images of CuPd for rank 7 in Table 3.1 (a) with Secondary Electron (SE) detector; (b) Backscatter Electron (BSE) detector.

3.5 Conclusion

We have discussed the preparative and structural studies of nitrides of noble metals, Cu, Ag, Pd, Au and Hg. In the case of silver nitrides, Ag_{3+x}N is found to adopt one variant of the perovskite structure, i.e. the $M_4\text{N}$ -type structure ($M = \text{Fe, Mn, Co, Ni, Cu}$), with fully or partially filled “A” site. Two methods were used to prepare silver nitride. Aqueous ammonia was used as the nitriding agent in the first method resulting in Ag_4N . Less Ag-rich samples Ag_{3+x}N ($x = 0.2-0.3$) were obtained via the gaseous ammonia route. The band structures of Ag_3N and Ag_4N calculated using TB-LMTO demonstrate that Ag_3N is an insulator while Ag_4N is metallic. The conduction band of the Ag_4N is formed from highly hybridized $\text{Ag}2\text{-s}$, $\text{Ag}1\text{-e}_g$ and N-p states.

The salts of other noble metals, i.e. Pd, Au and Hg with higher electronegativity than Ag and Cu, were reduced in the ammonolysis reactions with NH_3 , and no nitrides but metals were obtained. In the attempts to prepare ternary nitrides, no copper palladium nitride was obtained, whereas Ag and Cu_3N were the products from the ammonolysis reactions of AgCuF_3 with diluted NH_3 .

Chapter 4

Preparations, structures and properties of triclinic perovskites AgCuF_3 and NaCuF_3

4.1 Introduction

The perovskite-type structure represents a large family of compounds. Many superconducting ceramic materials (high temperature superconductors) have perovskite-like structures, often with 3 or more metals including copper, and some oxygen positions left vacant. Among the perovskite compounds there are also fluorides, such as KCuF_3 [1-4] and NaMgF_3 [70].

Apart from the cubic perovskite structure, the orthorhombic and tetragonal phases are the most common non-cubic variants. It was originally suggested [71, 72] that the temperatures T_C of zone-boundary transitions in perovskites should always increase with pressure; thus $dT_C/dP = \Delta S/\Delta V > 0$. This ‘‘general rule’’ has been challenged by recent experiments on several oxide perovskites which undergo tilt phase transitions to higher-symmetry phases on increasing pressure and as well as $dT_C/dP < 0$. LaAlO_3 was reported to undergo a phase transition at about 14 GPa from a structure with $R\bar{3}c$ symmetry to $Pm\bar{3}m$ symmetry [73].

Perovskites containing Jahn-Teller ions (i.e. Cu^{2+} and Mn^{3+}) on the octahedral site exhibit interesting physical properties, including charge ordering, spin ordering and cooperative Jahn-Teller distortions [8]. In an octahedral coordination, the first row transition-metal cations Cu^{2+} have electron configurations $(t_{2g})^6(e_g)^3$. The Jahn-Teller theorem predicts that a distortion of the ideal octahedral geometry will occur, thus providing an energetic stabilization by removing the electronic degeneracy of the highest occupied molecular orbital [74].

Ternary transition-metal fluorides NaMF_3 ($M = \text{Mn}$ [75-77], Fe [75, 78], Co [79, 80], Ni [80-82]) crystallize in the GdFeO_3 -type structure and exhibit interesting magnetic properties at low temperature [83-86]. The structure of the copper analogue NaCuF_3 [87] is a triclinic variant of this structure type, and such a low symmetry is rather unusual for a perovskite structure. The CuF_3 network of NaCuF_3 is made up of corner-sharing CuF_6

octahedra with Cu^{2+} (d^9) ions, and the cooperative Jahn-Teller distortions of these octahedra are responsible for the low-symmetry structure of NaCuF_3 . For the silver analogue AgCuF_3 , a monoclinic structure was proposed [88]. So far, the magnetic properties of NaCuF_3 and AgCuF_3 have not been reported yet.

In the present work, AgCuF_3 was synthesized and its room-temperature crystal structure was determined to be triclinic and isostructural with NaCuF_3 . The magnetic properties of AgCuF_3 and NaCuF_3 were examined by measuring their magnetic susceptibilities, EPR and specific heat, as well as powder neutron diffraction. Their spin exchange interactions were analyzed on the basis of both spin dimer analysis based on tight binding calculations and mapping analysis based on first principles electronic structure calculations. High pressure synchrotron investigations of the crystal structure were carried out for NaCuF_3 to examine the phase transition.

4.2 Experimental section

4.2.1 Sample preparation

Due to the extreme sensitivity of the reagents and products to air, all manipulations were carried out using Schlenk technique or an argon-filled glovebox. AgCuF_3 and NaCuF_3 were synthesized by the solid state reaction of the 1:1 mixture of the two binary fluorides, respectively.

For the synthesis of the AgCuF_3 powder sample, finely mixed AgF and CuF_2 were heated at 773 K for 3 days followed by slow cooling (0.5 K/min) [88], which resulted in a pale yellow powder. Single crystals of AgCuF_3 suitable for X-ray structure determination were selected from the reaction product of the same starting materials, which were heated at 873 K for 3 days. The as-grown clear crystals of AgCuF_3 were rather difficult to separate from each other, causing the difficulty to select large single-domain crystals.

The preparation of NaCuF_3 followed the procedure described in the literature [89]. A mixture of NaF and CuF_2 (total weight 0.85 g) was heated at 905 K for 12 hours, followed by a slow cooling of the ampoule (1 K/min).

4.2.2 Characterization

The samples were characterized by means of powder XRD, single crystal XRD, powder neutron diffraction for the structure information. An AgCuF_3 crystal of

0.24×0.24×0.26 mm³ was chosen for the single crystal XRD. After the data collection, the reflections could be successfully split into two data sets using the twin law (0 1 0 1 0 0 0 0 -1) encoded within the X-AREA program. The single crystal structure of AgCuF₃ was refined in the space group $P\bar{1}$ with the program SHELX-97 [40] within the WinGX program package [41], using an extinction parameter.

The magnetic susceptibility, specific heat and EPR spectra of the powder samples of AgCuF₃ and NaCuF₃ have been measured.

The high pressure study of NaCuF₃ was performed at the ID09A beamline of ESRF, Grenoble, using a MAR345 image plate detector. Determination of peak positions, indexing, and refinements of lattice parameters were performed using the Fullprof program [34].

The spin exchange parameters of AgCuF₃ and NaCuF₃ were calculated by performing a spin dimer analysis [42, 43] based on extended Hückel tight binding (EHTB) calculations [44, 90] as well as mapping analysis [45-48] based on first principles DFT electronic band structure calculations.

4.3 Results and Discussion

4.3.1 Crystal structure of AgCuF₃

The structure of AgCuF₃ was determined from single crystal XRD collected at ambient temperature. The data set was indexed in the triclinic unit cell with parameters $a = 5.5802 \text{ \AA}$, $b = 5.5787 \text{ \AA}$ and $c = 8.1018 \text{ \AA}$. Details of the data collection and structure refinement are listed in Table 4.1.

Table 4.2 presents the final results for the refined atomic positions and isotropic displacement factors for AgCuF₃. Selected interatomic distances are given in Table 4.3. The structure of AgCuF₃ is isotopic to that of NaCuF₃ with similar unit cell parameters (Table 4.4).

Table 4.1 Data collection and structure refinement parameters for AgCuF₃.

Empirical formula	AgCuF ₃
Formula weight	228.41
Wavelength (Å)	MoK α 0.71073
Crystal system	triclinic
Space group	$P\bar{1}$
data collection temperature (K)	293(2)
a (Å)	5.5802(13)
b (Å)	5.5787(11)
c (Å)	8.1018(19)
α (deg)	89.623(18)
β (deg)	90.928(19)
γ (deg)	93.496(18)
Volume (Å ³)	251.70(10)
Z	4
Density (calculated) (g/cm ³)	6.027
μ (mm ⁻¹)	16.042
Reflections collected	2891
Independent reflections	1024
parameters refined	99
Goodness-of-fit on F^2	0.888
Final R indices	$R_1 = 0.0456$, $wR_2 = 0.1035$
R indices (all data)	$R_1 = 0.0802$, $wR_2 = 0.1149$
Largest diff. peak and hole (e/Å ³)	1.64, -1.31

Table 4.2 Positional parameters and isotropic displacement factors for AgCuF₃.

Atom	<i>x</i>	<i>y</i>	<i>z</i>	$U_{\text{eq/iso}} (\text{\AA}^2)$
Ag1	0.50771(17)	0.52242(15)	0.24902(11)	0.0203(3)
Ag2	-0.00224(16)	0.02334(15)	0.25070(11)	0.0200(3)
Cu1	0.5000	0.0000	0.0000	0.0100(4)
Cu2	0.0000	0.5000	0.0000	0.0101(4)
Cu3	0.5000	0.0000	0.5000	0.0101(4)
Cu4	0.0000	0.5000	0.5000	0.0103(4)
F1	0.7129(12)	0.2885(10)	0.0396(10)	0.0214(14)
F2	0.2336(12)	0.1936(10)	-0.0340(10)	0.0215(14)
F3	0.7160(13)	0.2846(10)	0.4577(10)	0.0237(15)
F4	0.1907(12)	0.2360(10)	0.5334(9)	0.0210(14)
F5	0.4292(13)	-0.0183(10)	0.2723(8)	0.0190(13)
F6	0.0778(12)	0.4945(10)	0.2279(8)	0.0177(13)

Table 4.3 Selected interatomic distances (Å) in the structure of AgCuF₃.

Ag1 -F1	2.484(7)	Cu2 -F1 ×2	1.960(6)
Ag1 -F3	2.462(7)	Cu2 -F2 ×2	2.233(5)
Ag1 -F6	2.398(7)	Cu2 -F6 ×2	1.890(6)
Ag2 -F2	2.445(7)	Cu3 -F3 ×2	1.966(6)
Ag2 -F4	2.469(7)	Cu3 -F4 ×2	2.255(6)
Ag2 -F5	2.436(7)	Cu3 -F5 ×2	1.882(6)
Cu1 -F1 ×2	1.966(6)	Cu4 -F3 ×2	1.957(7)
Cu1 -F2 ×2	1.906(6)	Cu4 -F4 ×2	1.884(5)
Cu1 -F5 ×2	2.248(7)	Cu4 -F6 ×2	2.255(7)

Table 4.4 Lattice parameters of AgCuF₃ and NaCuF₃.

	AgCuF ₃	NaCuF ₃ [87]
Space group	$P\bar{1}$	$P\bar{1}$
a (Å)	5.5802(13)	5.391(2)
b (Å)	5.5787(11)	5.552(2)
c (Å)	8.1018(19)	7.928(2)
α (deg)	89.623(19)	90.66(2)
β (deg)	90.928(18)	92.05(2)
γ (deg)	93.496(10)	86.95(2)

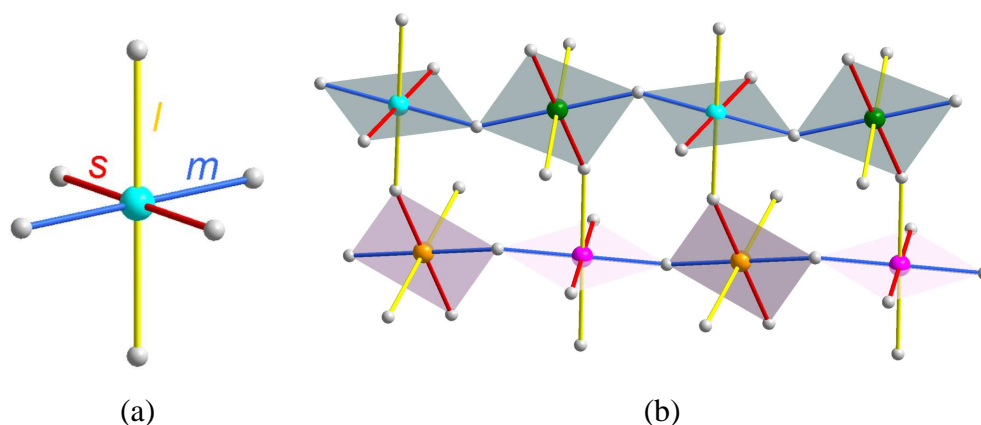


Figure 4.1 (a) Representative CuF₆ octahedron in AgCuF₃ with two short (*s*), two medium (*m*) and two long (*l*) Cu-F bonds; (b) Parallel corner-sharing CuF₆ octahedra chains. The upper chain constructed from Cu1 (turquoise) and Cu2 (green), the lower one from Cu3 (orange) and Cu4 (pink). For the color code of the bonds, see (a).

Each CuF₆ octahedron in AgCuF₃ has two short, two medium and two considerably longer Cu-F bonds (Cu-F_{*s*}, Cu-F_{*m*} and Cu-F_{*l*} bonds, respectively in Table 4.3). The Cu-F bonds of identical bond length are *trans* to each other (Figure 4.1a). Thus, each CuF₆ octahedron has the shape of an axially elongated octahedron, typical for the coordination of a Cu²⁺ ion. When the local *x*-, *y*- and *z*-axes of an isolated CuF₆ octahedron are fixed parallel to the Cu-F_{*s*}, Cu-F_{*m*} and Cu-F_{*l*} bonds, the magnetic orbital of the CuF₆ octahedron (i.e., the x^2-y^2 orbital) lies in the CuF₄ rectangular plane with the Cu-F_{*s*} and Cu-F_{*m*} bonds. For convenience, in our discussion, the CuF₄ plane containing the magnetic orbital will be referred to as the equatorial CuF₄ plane.

The 3D CuF_3 substructure of AgCuF_3 is formed from corner-sharing distorted CuF_6 octahedra. To show how their equatorial CuF_4 planes are interconnected in the 3D CuF_3 substructures, we first consider the CuF_5 chains constructed from the CuF_6 octahedra by sharing their F atoms forming the Cu-F_m bonds (Figure 4.1b). The 3D CuF_3 structure is obtained by corner-sharing the CuF_5 chains such that every Cu-F_s and Cu-F_l bonds of a given CuF_5 chain form Cu-F-Cu bridges with the Cu-F_l and Cu-F_s bonds of adjacent CuF_5 chains, respectively, as illustrated in Figure 4.2. It is apparent that the equatorial- CuF_4 planes form corner-sharing one-dimensional CuF_3 chains, and these 1D chains are isolated from each other.

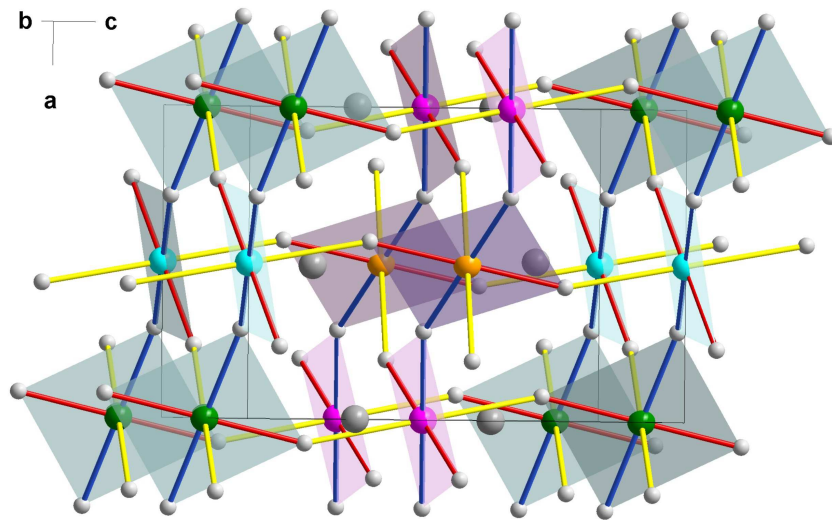


Figure 4.2 Unit cell of AgCuF_3 . Ag atoms are drawn in gray. For the coloring of the other atoms, see Figure 4.1.

There are two types of 1D CuF_3 chains. The Cu1 and Cu2 atoms alternate along the chain in one type of 1D CuF_3 chain, while the Cu3 and Cu4 atoms do in another type of 1D CuF_3 chain. To a first approximation, the magnetic properties of AgCuF_3 should be 1D because, within each 1D CuF_3 chain, adjacent spin sites have Cu-F-Cu (bonding angle $\sim 150^\circ$) superexchange interactions through the overlap between their magnetic orbitals. Within or between 1D CuF_3 chains, there is no favorable $\text{Cu-F}\dots\text{F-Cu}$ super-superexchange path between adjacent spin sites. A similar exchange interaction is expected for the magnetic properties of NaCuF_3 , because it is isostructural with AgCuF_3 . For AgCuF_3 and NaCuF_3 , Table 4.5 summarizes the geometrical parameters associated with the nearest-neighbor spin exchange paths in the 1D CuF_3 chains, namely, J_{12} for the chain with Cu1 and Cu2 and J_{34} for the chain with Cu3 and Cu4. Along these chains the Cu-F-Cu-F arrangement is in a similar way as in Ag_2SO_4 [91].

Table 4.5 Geometrical parameters and singlet-triplet splitting energy $(\Delta\varepsilon)^2$ values associated with the spin exchange paths in AgCuF_3 and NaCuF_3 ^a.

(a) AgCuF_3				
	Cu...Cu (Å)	Cu-F (Å)	$\angle\text{Cu-F-Cu}$ (°)	$(\Delta\varepsilon)^2$
J_{12}	3.823	Cu(1)-F = 1.966	153.6	19800
		Cu(2)-F = 1.960		
J_{34}	3.823	Cu(3)-F = 1.960	154.2	21400
		Cu(4)-F = 1.957		
(b) NaCuF_3				
	Cu...Cu (Å)	Cu-F (Å)	$\angle\text{Cu-F-Cu}$ (°)	$(\Delta\varepsilon)^2$
J_{12}	3.765	Cu(1)-F = 1.975	144.2	13800
		Cu(2)-F = 1.981		
J_{34}	3.765	Cu(3)-F = 1.969	146.2	15300
		Cu(3)-F = 1.966		

^a The $(\Delta\varepsilon)^2$ values are in units of $(\text{meV})^2$.

4.3.2 Thermal analysis

The DSC result for AgCuF_3 is shown in Figure 4.3. During heating, there are three endothermic peaks at 342, 469 and 574 °C, respectively. The last peak is strongest and corresponds to the melting of AgCuF_3 . Further heating caused partial decomposition into Ag, and the DSC curve becomes more complicated as can be seen between 574 and 600 °C. In the curve for subsequent cooling there are three exothermic peaks at 339, 458 and 570°C corresponding to the above three endothermic peaks respectively. Besides, some endothermic peaks are also detected which might be related to the decomposition of AgCuF_3 . According to the XRD measurement for the resulting powder, only a small portion of the starting material has decomposed.

Differently NaCuF_3 exhibits the congruent melting point at 616 °C and freezing point at 604 °C (Figure 4.4). The other two smaller peaks are due to the impurity Na_2CuF_4 .

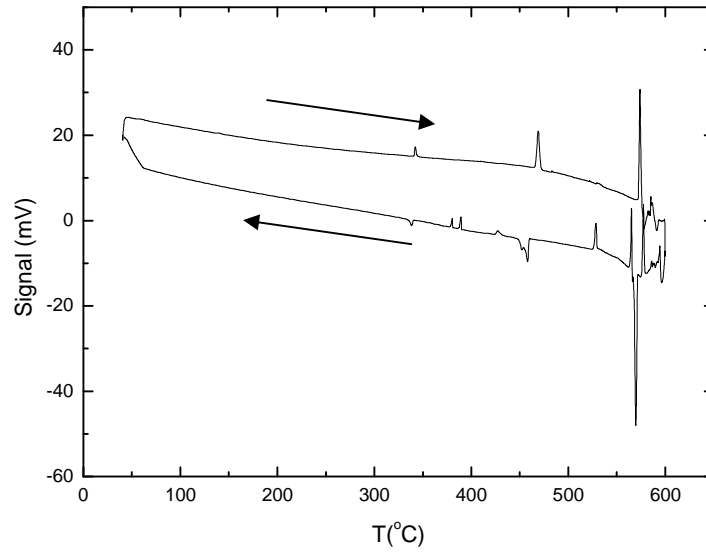


Figure 4.3 DSC curve for AgCuF_3 .

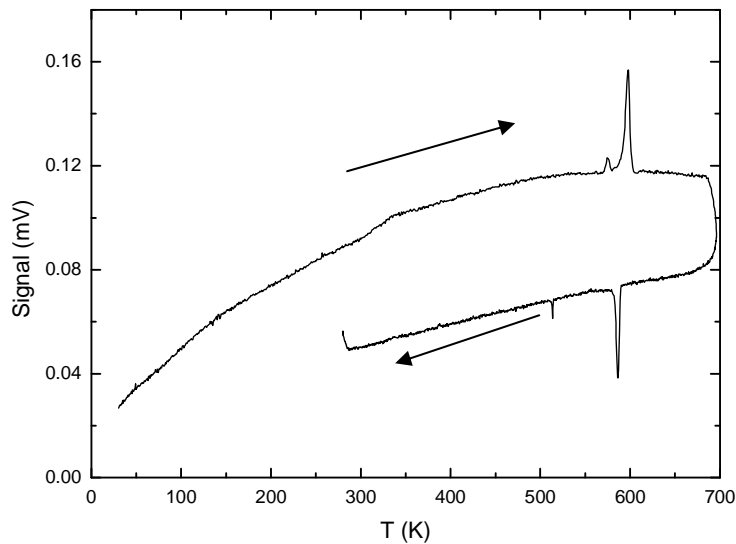


Figure 4.4 DTA curve for NaCuF_3 .

4.3.3 Magnetic susceptibilities

The temperature-dependence of the magnetic susceptibility $\chi(T)$ of AgCuF_3 is presented in Figure 4.5. The susceptibility is characterized by a broad maximum (at $T_{\text{max}} \approx 190$ K) indicative of the occurrence of a short-range antiferromagnetic ordering. As the temperature is lowered, $\chi(T)$ starts to increase rapidly from ~ 47 K to a peak at 20 K, and then decreases slowly. We attribute the peak at 20 K to the onset of a complex long-range antiferromagnetic ordering possibly to a canted spin structure, leaving a weak ferromagnetic moment.

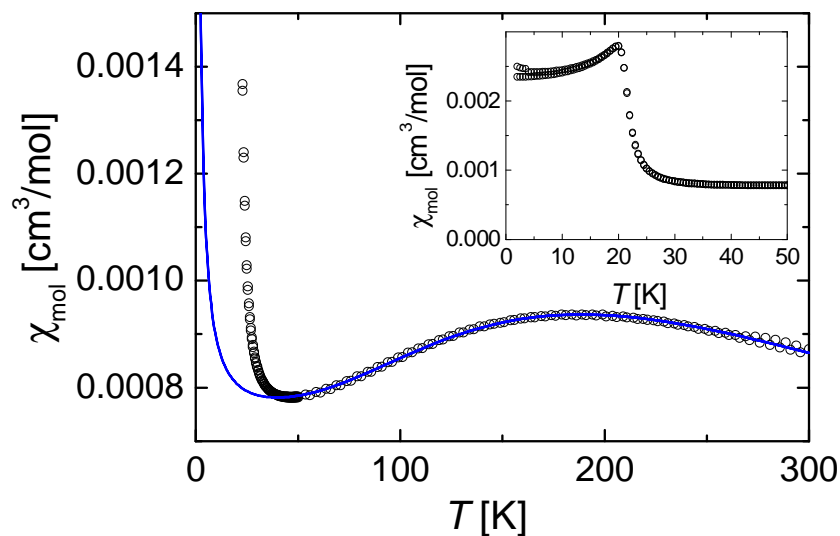


Figure 4.5 Temperature-dependence of the magnetic susceptibility of AgCuF_3 in the range of 2 - 300 K. The experimental values are presented by circles, and the solid blue line is fitted. The inset shows the molar magnetic susceptibility at low temperatures.

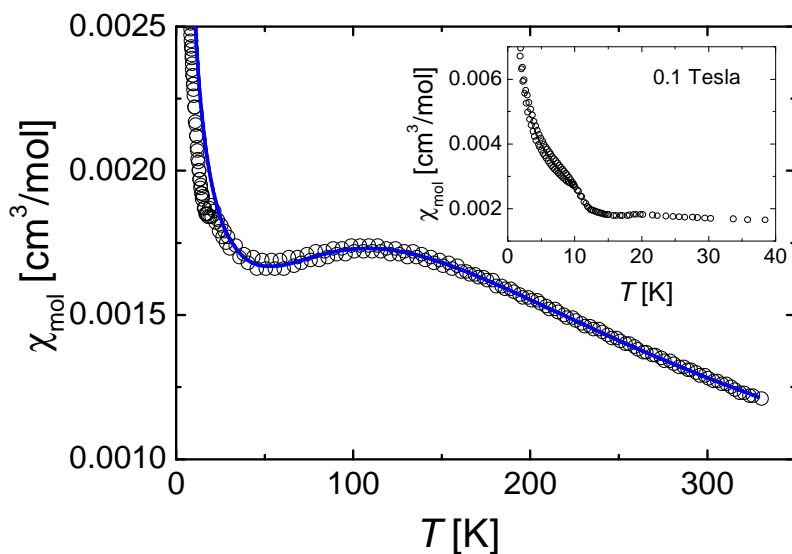


Figure 4.6 Temperature dependence of the magnetic susceptibility of NaCuF_3 in the range of 2 - 300 K. The experimental values are presented by circles, and the solid blue line is the fitting curve in terms of a $S = 1/2$ Heisenberg chain with antiferromagnetic nearest-neighbor interaction. The inset shows the molar magnetic susceptibility determined with an external field of 0.1 T at low temperatures.

The susceptibility $\chi(T)$ of NaCuF₃, displayed in Figure 4.6, shows also a broad maximum, however, at a lower temperature ($T_{\max} \approx 115$ K) and starts increasing below ~ 50 K with a significantly less pronounced ordering peak at ~ 18 K and a rapid increase of the susceptibility below due to a considerable paramagnetic impurity (cf. the results of the fits of the full temperature dependence of the magnetic susceptibility as discussed below).

As shown in the previous section, there are two types of 1D CuF₃ chains in AgCuF₃. If the small difference between them is neglected, the magnetic properties of AgCuF₃ and NaCuF₃ can be analyzed in terms of a spin-1/2 Heisenberg uniform antiferromagnetic chain model with the nearest-neighbor spin exchange J . For this model, J and T_{\max} are related via [92]:

$$T_{\max} = 0.64085 |J/k_B| \quad \text{Eq. 4.1}$$

Thus, from the observed T_{\max} values, we obtain $J/k_B \approx -300$ K for AgCuF₃ and $J/k_B \approx -180$ K for NaCuF₃. Another approach to the exchange constants can be made by fitting the $\chi(T)$ data in the temperature range 40 – 300 K to the theoretical prediction of the magnetic susceptibility of a spin-1/2 Heisenberg uniform antiferromagnetic chain model with nearest neighbor interaction [92]. The fits converged to $g = 2.26$ and $J/k_B = -298$ K for AgCuF₃, and $g = 2.29$ and $J/k_B = -191$ K for NaCuF₃. In the fits we have included a Curie term ($\propto C/T$) in order to account for small traces of paramagnetic impurities. This Curie term leads to the hyperbolic upturn at low temperatures. The fitted Curie constants C indicate an impurity level ($S = 1/2$ entities of $\sim 3.4\%$ for NaCuF₃ and of 0.52% for AgCuF₃, respectively). A constant temperature independent term χ_0 of 94×10^{-6} cm³/mol and of -16×10^{-6} cm³/mol for NaCuF₃ and AgCuF₃, respectively, has been added to account for diamagnetic and van Vleck paramagnetic contributions to the magnetic susceptibilities.

The J/k_B values are in good agreement with those obtained from Eq. 4.1, namely, the average intrachain spin exchange J is stronger for AgCuF₃ than for NaCuF₃ by a factor of ~ 1.6 . This is understandable because, in both Cu1-F-Cu2 and Cu3-F-Cu4 spin exchange paths, the Cu-F bonds are shorter and the \angle Cu-F-Cu bond angles are larger for AgCuF₃ than for NaCuF₃.

4.3.4 Electron paramagnetic resonance

The EPR spectra allow us to measure the magnetic-field dependent behavior of the g factor and examine the intrachain Cu-F-Cu spin exchange interaction. From the analysis of XRD and magnetic susceptibility data, it is evident that Cu (II) ions in both AgCuF_3 and NaCuF_3 are characteristic of 1D antiferromagnetic chain, which is further confirmed by the EPR results.

Figure 4.7 shows the 3D representation of the temperature dependence of the EPR signal for an AgCuF_3 powder sample with temperature decreasing in a range of 100 – 20 K. The spectrum is dominated by an intense isotropic EPR line of Lorentzian line shape. More detailed information is shown in the 2D representations at different temperatures in the range of (a) 150 – 30 K, (b) 28 – 20 K (Figure 4.8). The line narrows rapidly with decreasing temperature until 30 K. When the sample is further cooled down, the EPR line becomes broad again.

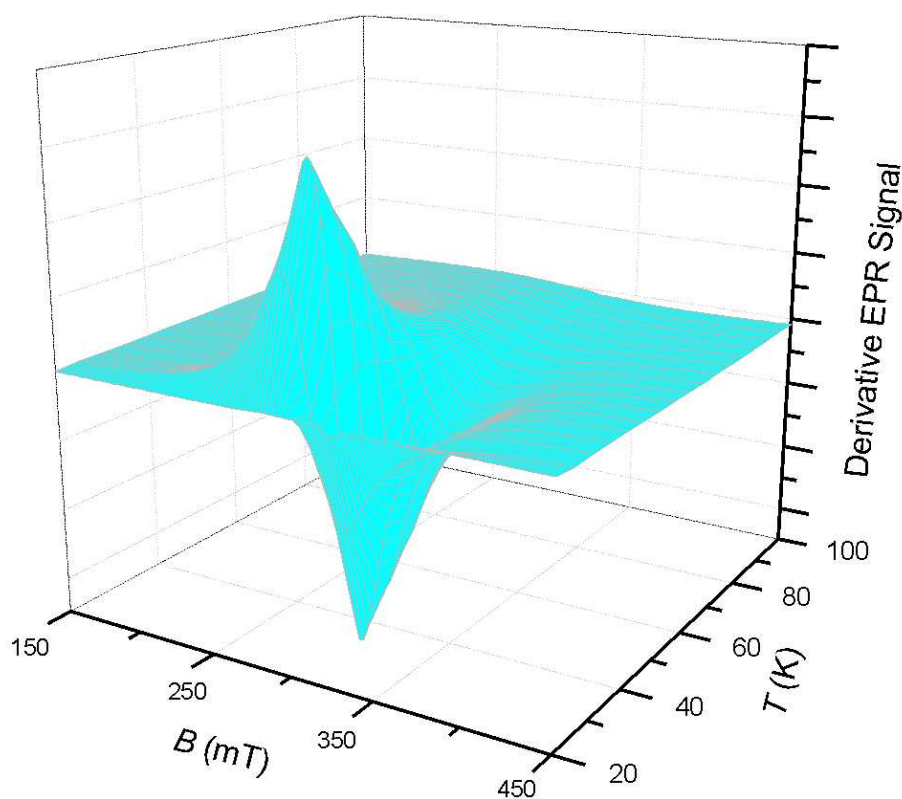


Figure 4.7 3D representation of the temperature dependence of the EPR signal for AgCuF_3 with temperature decreasing in a range of 100 - 20 K.

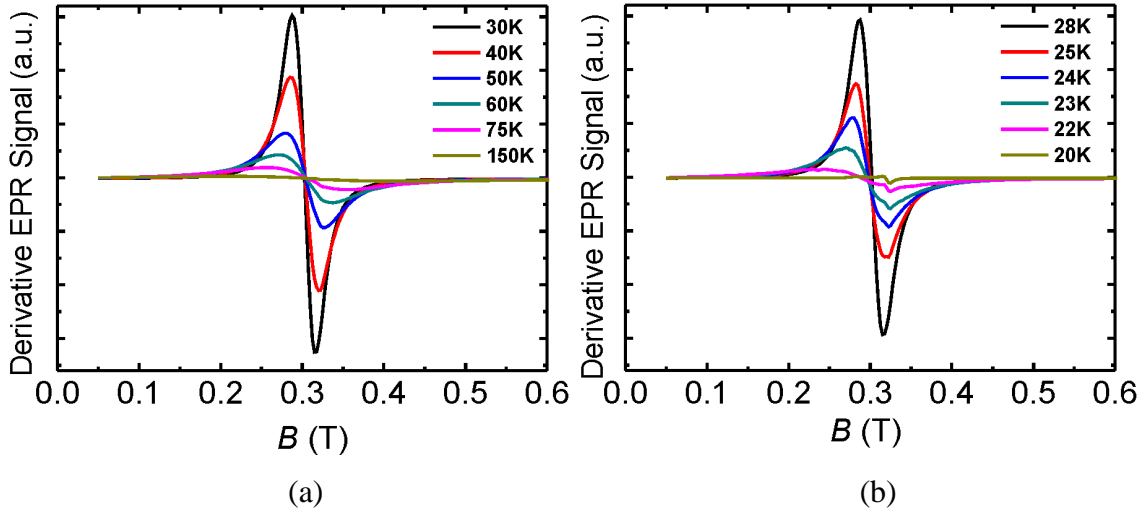


Figure 4.8 2D representations of the temperature dependence of the EPR signal for AgCuF_3 with temperature decreasing in a range of (a) 150 – 30 K, (b) 28 – 20 K.

As shown in Figure 4.8, below 25 K the signal becomes more asymmetric and at even lower temperature an additional signal with a smaller line width, lower intensity and lower resonance field occurs on the right side of the main line. Since the temperature is just above T_N , this second signal might be related to paramagnetic impurities.

Figure 4.9 shows a typical EPR signal at $T = 30\text{K}$ (inset), the temperature behavior of the line width (top panel), the intensity of the EPR signal (middle panel) and the temperature dependence of the g factor (bottom panel) for AgCuF_3 . At temperatures $T > 25\text{ K}$ we observe a signal which can be nicely fitted with a single differential Lorentzian line (red line in the inset) providing the EPR parameters line width and g factor ($g = \mu_B B_0 / h\nu$, B_0 - resonance field). The temperature variation of the intensity I was derived by double integration of the first derivative EPR line after correcting for baseline shift and a linear component of B (Figure 4.9 middle). The integrated intensity I is proportional to the spin susceptibility, and it is compared to the renormalized fit from the molar susceptibility from Figure 4.5 with a hump at around 175 K (red line in Figure 4.9 middle). The maximum at $T = 30\text{ K}$ and the subsequent decrease of I at lower temperatures demonstrate the onset of the long range ordering. The observed g factors of ~ 2.14 ($\mu_{\text{eff}} \approx 1.853 \mu_B$) at room temperature are reasonable for Cu^{2+} powder samples in a distorted octahedral environment since a $3d^9$ system should have a spin orbital coupling constant of negative value.

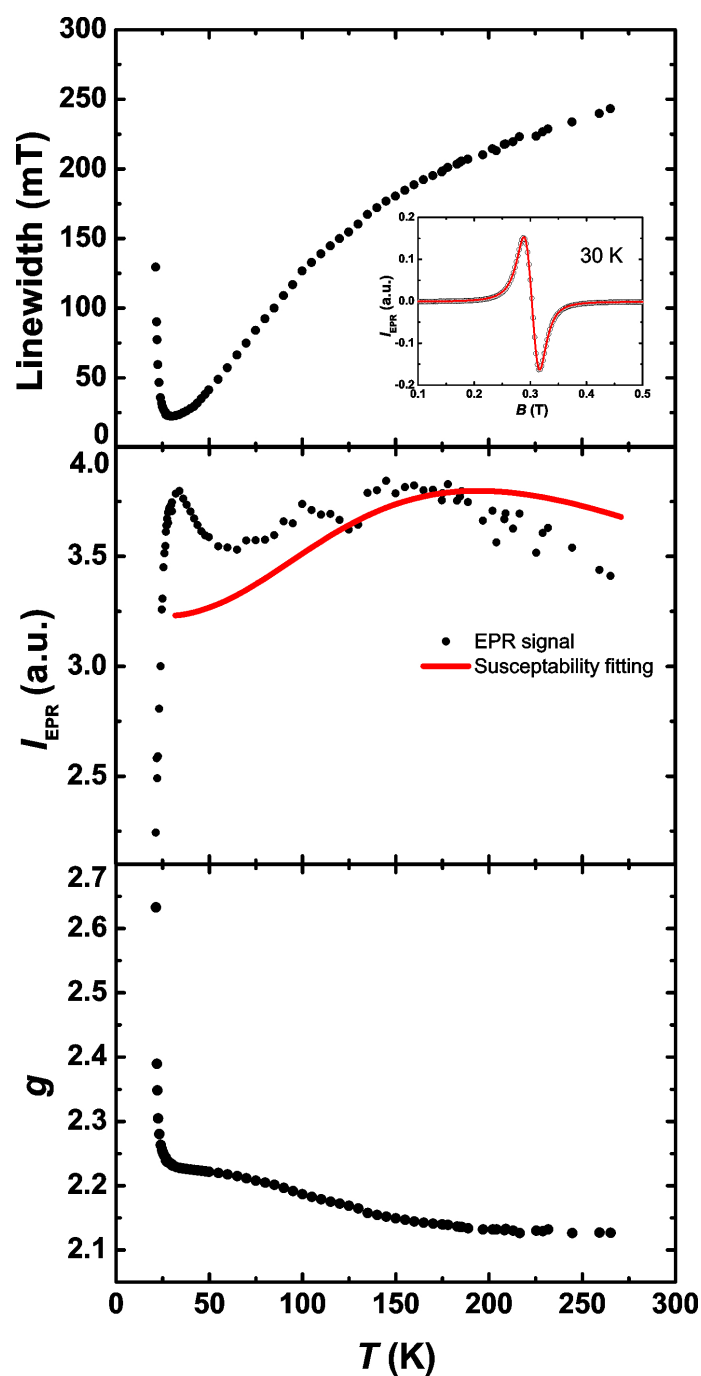


Figure 4.9 The inset shows a typical EPR signal for AgCuF_3 (black circles) with the differential of a Lorentzian fit (red line) given. The temperature dependence of the signals line width (black circles) is shown for AgCuF_3 in the top main panel. The two lower panels show the intensity of the EPR signal with renormalized fit from the molar magnetic susceptibility (middle) and the temperature dependence of the g factor (bottom) for AgCuF_3 .

The line width shows a definite minimum at $T = 30$ K and increases rapidly at lower temperatures, while in the same temperature range, g exhibits an obvious platform and then a considerable increase. The divergence of the line width and g factor at lower temperatures indicate a magnetic phase transition below 20 K. This behavior is similar to the oxygen deficient $RBa_2Cu_3O_{6+x}$ ($R = Nd, Sm$) and can be phenomenologically explained in terms of a fluctuating internal field which adds to the applied field altering the resonance condition, while at the same time slowing down of the fluctuation rate of this field may produce a progressive broadening of the resonance line as the temperature decreases [93]. The occurrence of such fluctuating fields might be traced back to short range ordering.

Figure 4.10 and Figure 4.11 show the temperature dependence of the EPR spectrum recorded for a powder sample of $NaCuF_3$. The 3D representation for $NaCuF_3$ in Figure 4.10 shows the increase of the signal with temperature decreasing between 100 – 20 K. A radical change of the EPR signal has occurred as more than one single line appears. More detailed information is shown in the 2D representations at certain temperatures (a) decreasing firstly from 100K to 25 K, and afterwards (b) increasing from 22 K to 97 K. The two processes exhibit similar behavior.

Within the temperature range of 22 - 260 K for $NaCuF_3$, we observe a signal which can be nicely fitted with three Lorentzian lines providing the EPR parameters line width and g factor shown in Figure 4.12. In a typical EPR signal at $T = 22$ K (inset), the Lorentzian fit (red line) is the sum of three individual Lorentzian lines (black, turquoise and purple lines), representing three different phases in the sample. In the main panels, red dots represent the main phase $NaCuF_3$, while the black and turquoise dots are ascribed to paramagnetic impurities. As can be seen in all three panels, the black and turquoise dots both remain unchanged over the whole temperature range. At lower temperature the intensity of the signal is too low and as such the fit gets less reliable, causing the fluctuation, especially for the integral intensity and g factor (two lower panels). In the top panel, the line width decreases as the temperature lowers, indicating that the transition from the strongly correlated 1D regime at low temperatures to a purely paramagnetic regime. The big error bars for the intensity at higher temperatures hinder the reproduction of the typical hump from fit data for the susceptibility for a 1D AFM chain. The observed g factors are in good agreement with expected g factor of Cu^{2+} of 2.13 shown as the dotted line.

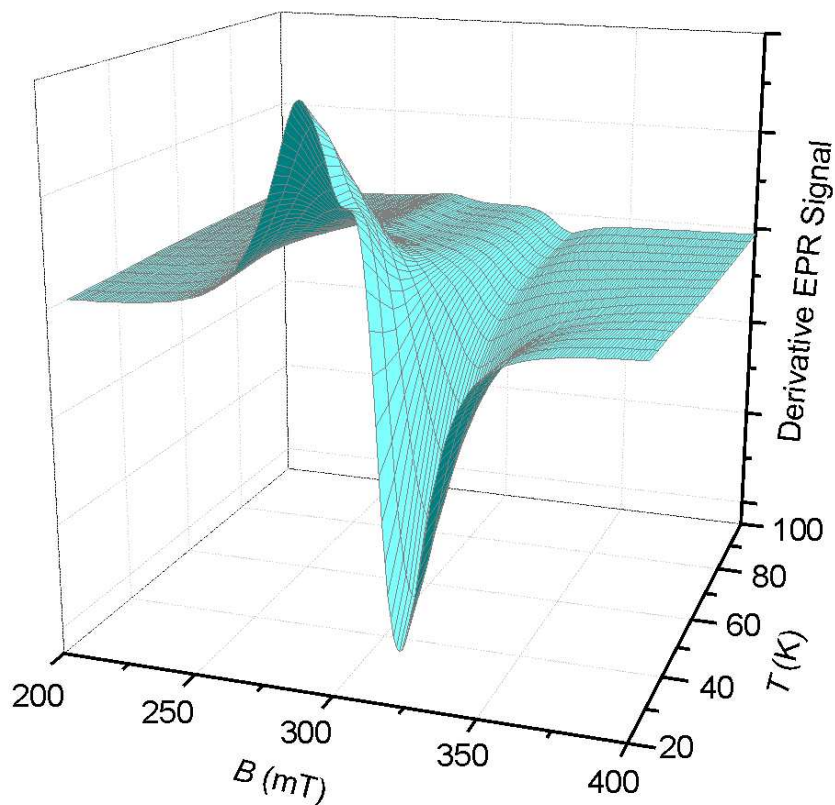


Figure 4.10 3D representation of the temperature dependence of the EPR signal for NaCuF_3 with temperature decreasing in a range of 100 – 20 K.

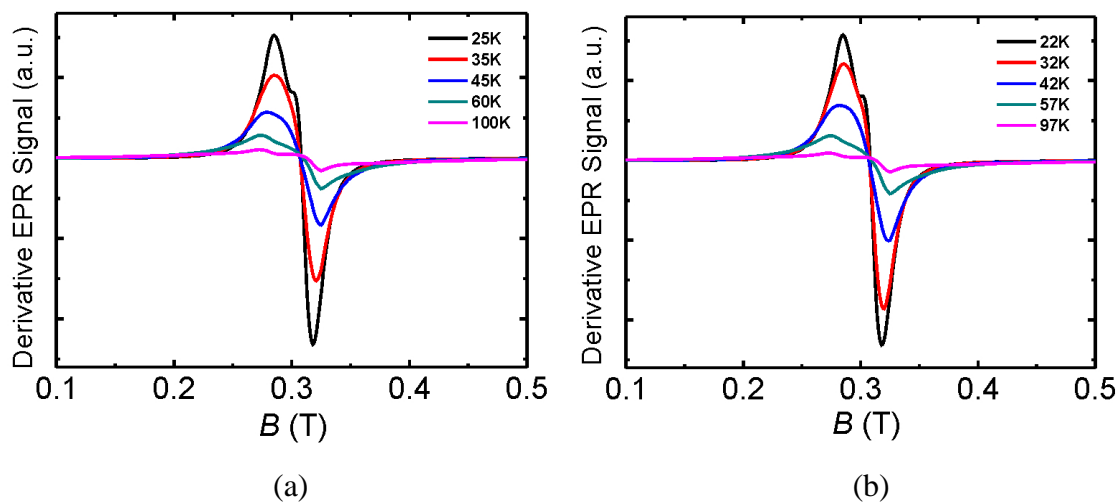


Figure 4.11 2D representations of the temperature dependence of the EPR signal for NaCuF_3 with temperature (a) decreasing between 100 – 25 K and (b) increasing between 22 – 97 K.

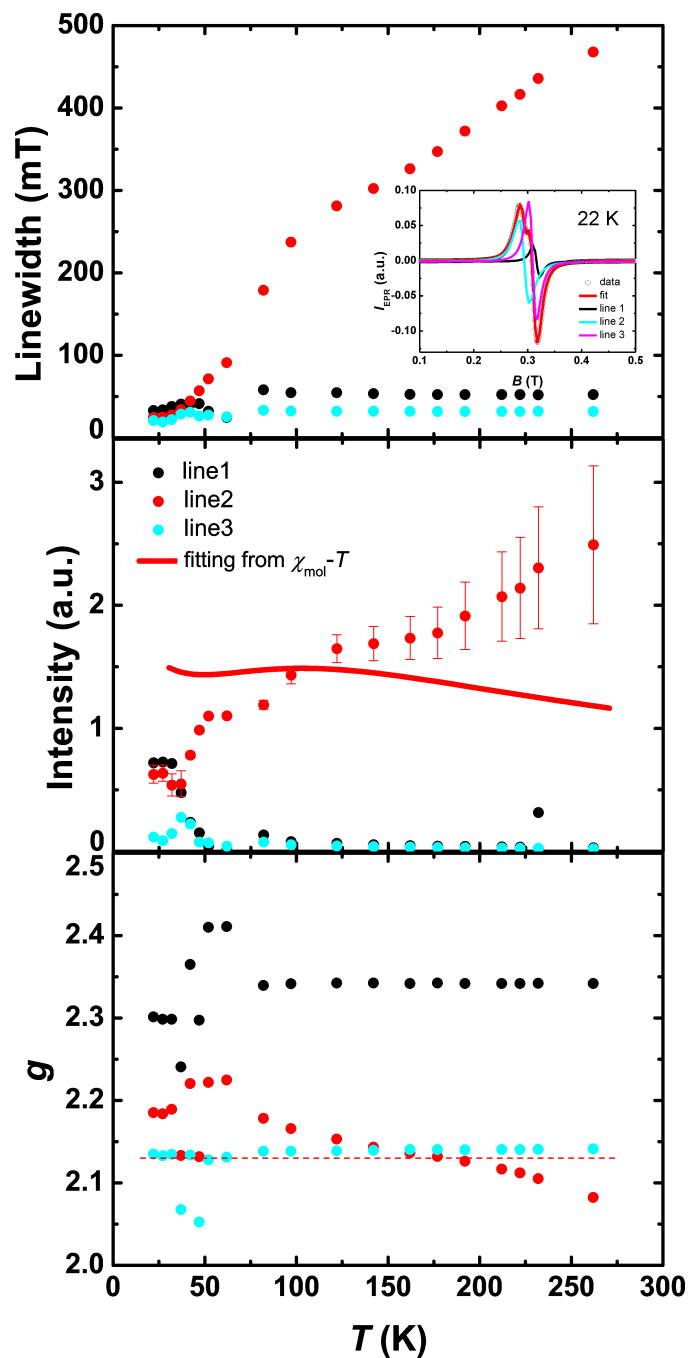


Figure 4.12 The inset shows a typical EPR signal for NaCuF_3 (black circles) with the differential of a Lorentzian fit (red line), the deconvoluted signals are shown by respective lines in black, turquoise and purple. In the main panels, red dots represent NaCuF_3 , while the black and turquoise dots are the paramagnetic impurities. The temperature dependence of line width (black circles) is shown for NaCuF_3 in the top main panel. The middle panel shows the intensity with error bars of the EPR signal and the renormalized fit from the molar susceptibility (red solid line). Shown in the bottom panel is the temperature dependence of the g factor, with the dotted line showing expected g factor of Cu^{2+} of 2.13.

4.3.5 Specific heat

In order to better verify the phase transition temperatures and superexchange intrachain interactions of AgCuF_3 and NaCuF_3 obtained from the magnetic data, the specific heat of both compounds (powder samples) have been determined for the first time. In Figure 4.13 an anomaly in the plot of C_p/T vs. T^2 at 21.1 K can be ascribed to the long range ordering in AgCuF_3 . The fitting in the temperature range above T_N is done according to Eq. 4.2. The specific heat C_p is composed of two parts, the magnetic part C_{mag} and the lattice part C_{lat} . Eq. 4.3 and 3.4 show the relationship of C_{mag} and C_{lat} with temperature respectively, in which R is the gas constant, J is the superexchange intrachain interaction between adjacent Cu^{2+} ions, β and δ are the parameters of higher order in T^2 with $\beta = N \times 1944 (1/T_D)^3$, wherein N is Avogadro constant and T_D is the Debye temperature [94].

In the plot of C_p/T vs. T^2 for AgCuF_3 , there is good agreement between the fitting and the experimental data in the temperature above T_N with $J/k_B = -35(2)$ K and $T_D = 239(2)$ K. The negative value of J/k_B means the exchange interaction between adjacent Cu^{2+} ions is antiferromagnetic, but the value is different from that obtained from the fit of susceptibility data, i.e. -298 K. In order to reconcile the discrepancy, we repeated the measurement several times with different batches of AgCuF_3 samples. The same result has been obtained with good repeatability.

$$C_p = C_{mag} + C_{lat} \quad \text{Eq. 4.2}$$

$$C_{mag}/T = 2/3 \times R/J \quad \text{Eq. 4.3}$$

$$C_{lat}/T = \beta T^2 + \delta T^4 \quad \text{Eq. 3.4}$$

The temperature dependence of the specific heat for NaCuF_3 is shown in Figure 4.14. The anomaly observed for NaCuF_3 is at $T_N = 18.6$ K. Using the same fitting procedure, $J/k_B = -201(6)$ K and $T_D = 315(2)$ K have been obtained for NaCuF_3 . The J/k_B is in good agreement with the result obtained from susceptibility data, -191 K.

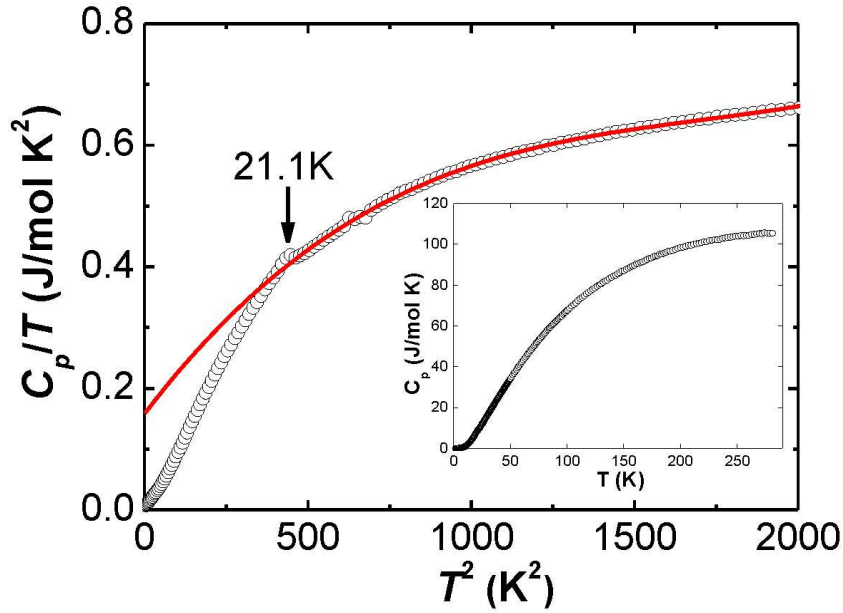


Figure 4.13 The plot of C_p/T vs. T^2 for AgCuF_3 with a sharp anomaly at 21.1 K and the fit according to Eq.3.2-3.4 (red line) with the inset shows the temperature dependence of the specific heat.

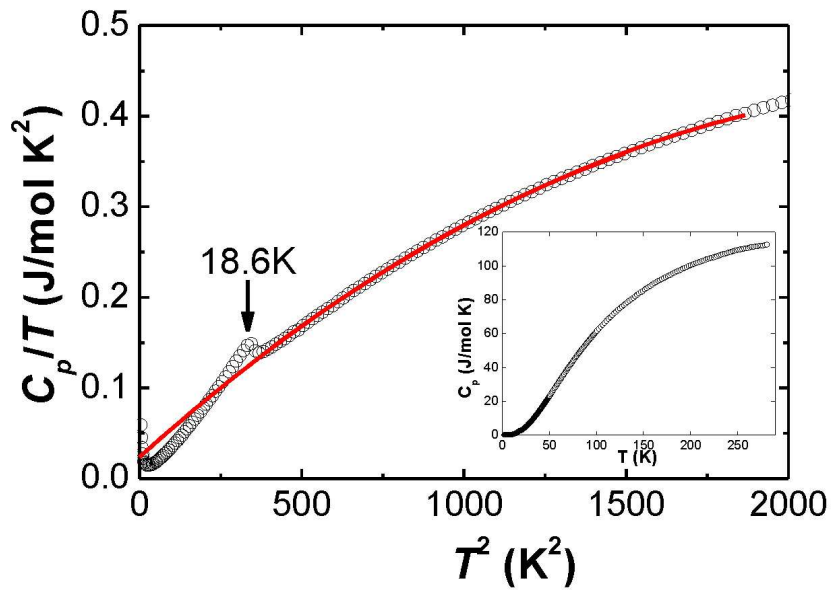


Figure 4.14 The plot of C_p/T vs. T^2 for NaCuF_3 with a sharp anomaly at 18.6 K and the fit according to Eq. 4.2-3.4 (red line) with the inset showing the temperature dependence of the specific heat.

4.3.6 Powder neutron diffraction studies

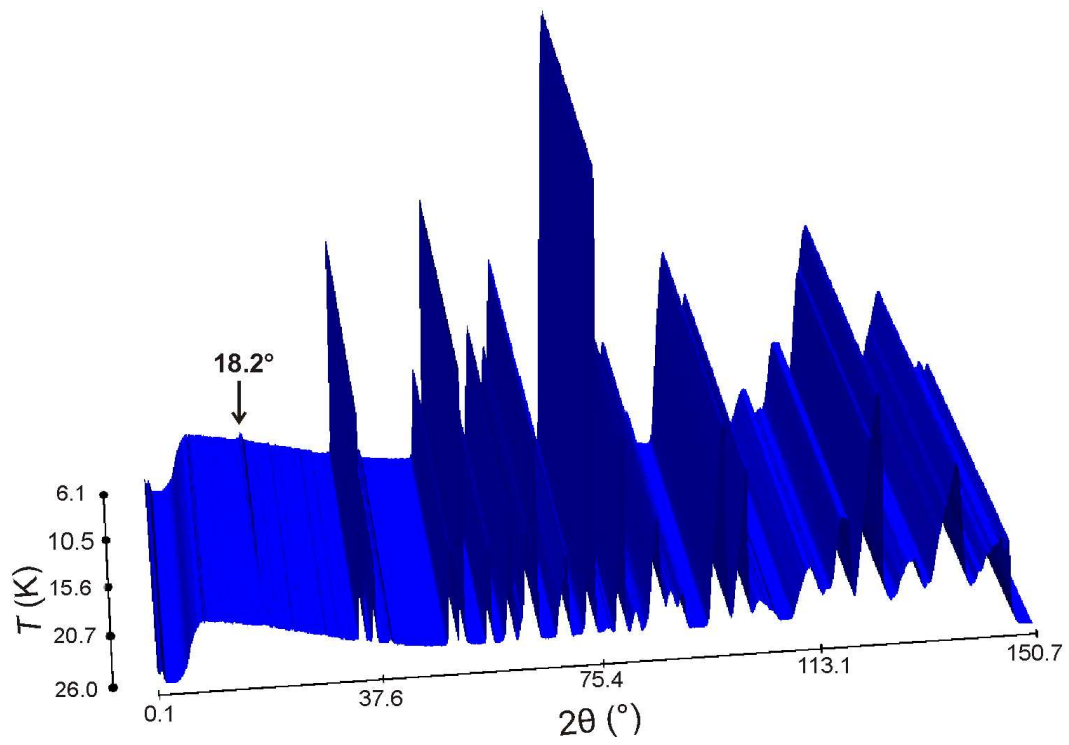
Powder neutron diffraction measurements were performed in order to obtain the magnetic structures of AgCuF_3 and NaCuF_3 and to follow the structural properties as a function of temperature. The temperature dependence of the neutron diffraction patterns for AgCuF_3 and NaCuF_3 are shown in Figure 4.15.

Due to the small moment of the Cu^{2+} ions, only a few weak magnetic Bragg reflections were observed below the Néel temperature. The temperature dependence of these reflections identifies them unambiguously of magnetic origin demonstrated for both compounds in Figure 4.16.

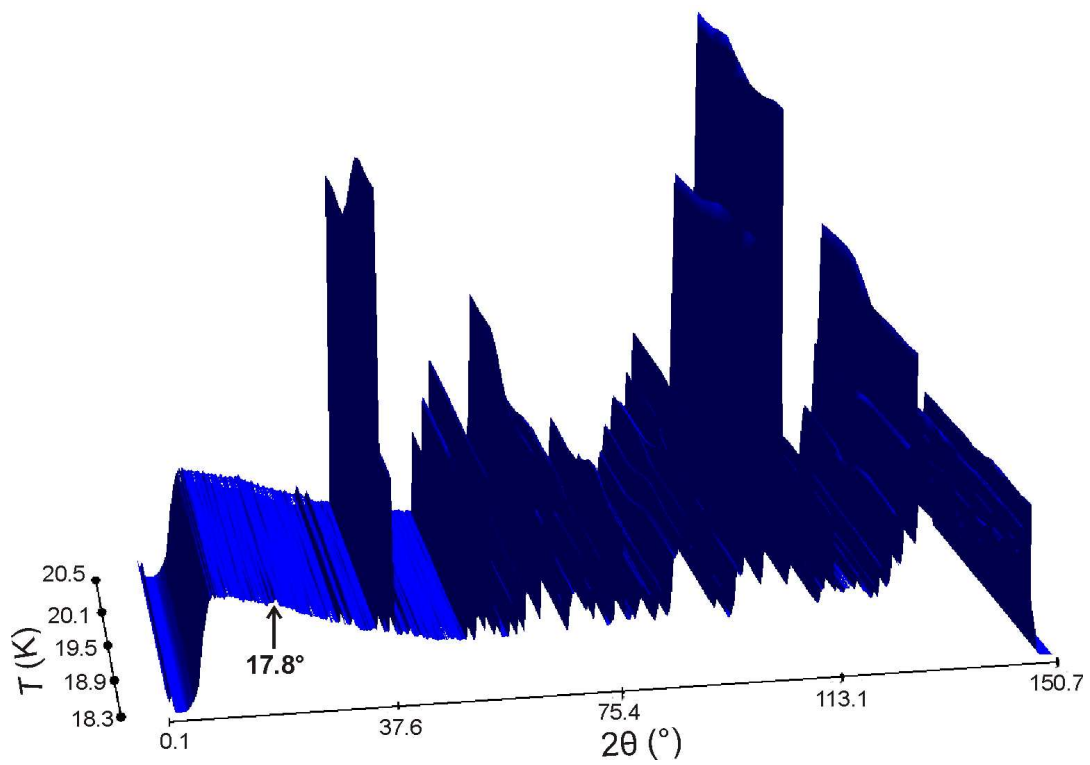
The integrated intensity of the magnetic reflection observed at $2\theta = 18.2^\circ$ for AgCuF_3 ($\lambda = 2.4 \text{ \AA}$) was calculated at different temperatures with the Origin program. A fitting with a power law shown as red line in Figure 4.16(a) was obtained with the critical temperature of 21.3(5) K, when the magnetic reflections were found to disappear in the 3D graph in Figure 4.15(a).

Similarly for NaCuF_3 , $T_N(\text{NaCuF}_3) = 18.5(3) \text{ K}$ has been obtained from the fitting of the temperature dependence of the magnetic reflection at $2\theta = 17.8^\circ$. These temperatures are in good agreement with the measurements of the specific heat and magnetic susceptibilities.

The profile matching (Le Bail method) and Rietveld refinements to the diffraction data collected at 2 and 30 K for AgCuF_3 have been performed using Fullprof [34]. However, the Bragg peaks in the 2θ range from 66° to 72° or the one asymmetric peak near 37° in the pattern at 30 K are unlikely to be indexed and refined as a starting phase for a magnetic structure refinement. The difference curve between 2 and 30 K data for AgCuF_3 shown in green in Figure 4.17 exhibits clearly the occurrence of several magnetic reflections below the ordering temperature. A magnetic reflection at $\sim 18.2^\circ$ is clearly seen, which has already been discussed before. Due to these reflections, it is possible to define a propagation vector by indexing the positions in the scattering angle. Using BASIREPS within the Fullprof suite, we arrive at a tentative propagation vector of $\mathbf{k} = [0.25, 0, 0]$ for AgCuF_3 , which suggests a commensurate structure along the a axis with a quadrupling of the nuclear cell.



(a)



(b)

Figure 4.15 The 3D temperature dependence of the powder neutron diffraction patterns of (a) AgCuF_3 and (b) NaCuF_3 .

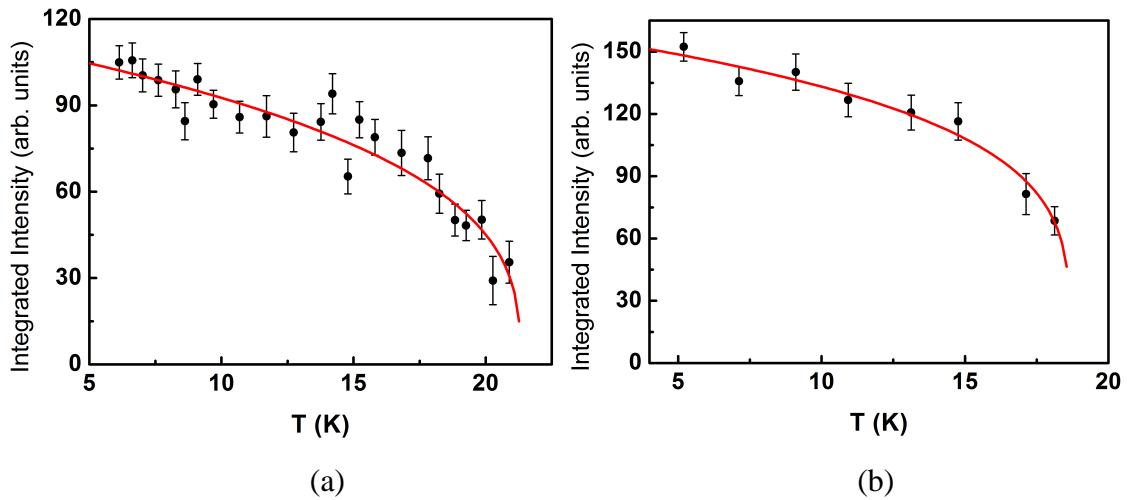


Figure 4.16 The temperature dependence of the integrated intensity of the magnetic reflection observed for (a): AgCuF_3 at $2\theta = 18.2^\circ$ and (b): NaCuF_3 at $2\theta = 17.8^\circ$ ($\lambda = 2.4 \text{ \AA}$). The solid line is a fit of the experimental data with a power law with a critical temperature of $T_N(\text{AgCuF}_3) = 21.3(5) \text{ K}$ and $T_N(\text{NaCuF}_3) = 18.5(3) \text{ K}$.

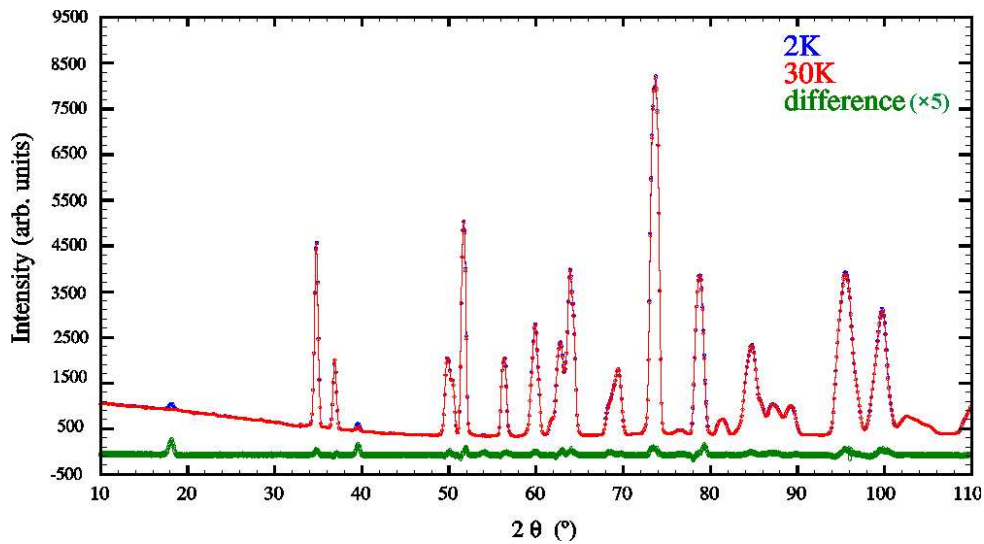


Figure 4.17 Powder neutron diffraction pattern of AgCuF_3 : The green line in the bottom is the difference between diffraction data of 2 K (red) and 30 K (blue), showing the magnetic reflections.

Likewise, a clearly visible magnetic reflection at 2θ of $\sim 17.8^\circ$ has been observed for NaCuF_3 . The 2D temperature dependence of the powder neutron diffraction for NaCuF_3 is shown in Figure 4.18. There seems to be a structural transition around 19 K, which is very close to the magnetic ordering temperature, i.e. 18.5 K. The difference curve between the diffraction patterns at temperatures 2 K and 30 K shown in Figure 4.19 contains too many differences other than only magnetic reflections, causing the difficulty to index for the propagation vector. However, it is reasonable to suggest that the propagation vector for AgCuF_3 and NaCuF_3 do not differ greatly, as we expect from the similarity in the crystal structure.

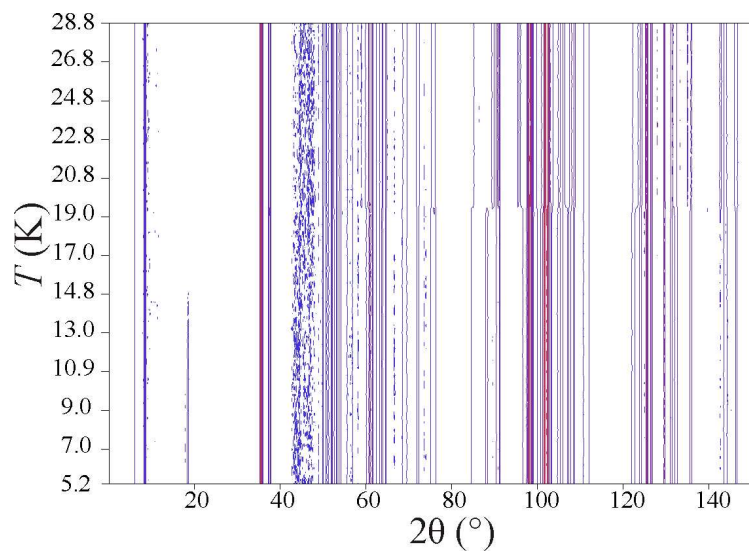


Figure 4.18 The 2D graph of the temperature dependence of powder neutron diffraction for NaCuF_3 .

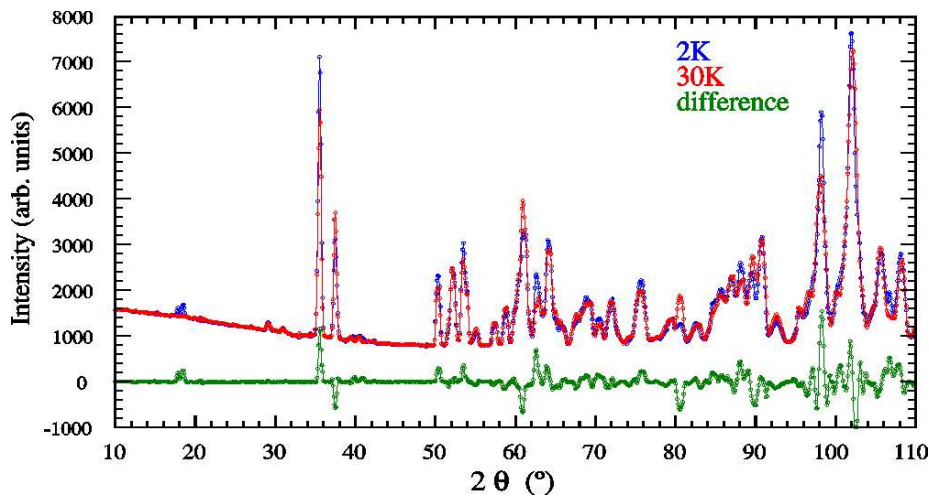


Figure 4.19 Powder neutron diffraction patterns taken at $T = 2$ K and 30 K as well as their difference (2 K - 30 K) for NaCuF_3 .

4.3.7 High pressure study of NaCuF₃

Figure 4.20 shows the high pressure synchrotron data for NaCuF₃. The pattern at the starting pressure, i.e. 5.5 kbar, corresponds to one pure phase of NaCuF₃ according to a Rietveld refinement using the TOPAS program. As the pressure increases, NaCuF₃ exhibits an incomplete phase transition at a pressure above 130 kbar. The new phase does not transform back when the pressure was released, indicating an irreversible transition.

Attempts to index the new phase found at high pressure using Fullprof give a possible monoclinic unit cell with $a \sim 5.0 \text{ \AA}$, $b \sim 3.6 \text{ \AA}$, $c \sim 5.5 \text{ \AA}$. Further search for a suitable model in a large number of (distorted) perovskite structures has been done, and until now several possible models have been proposed. More efforts have to be taken in the future to solve this problem.

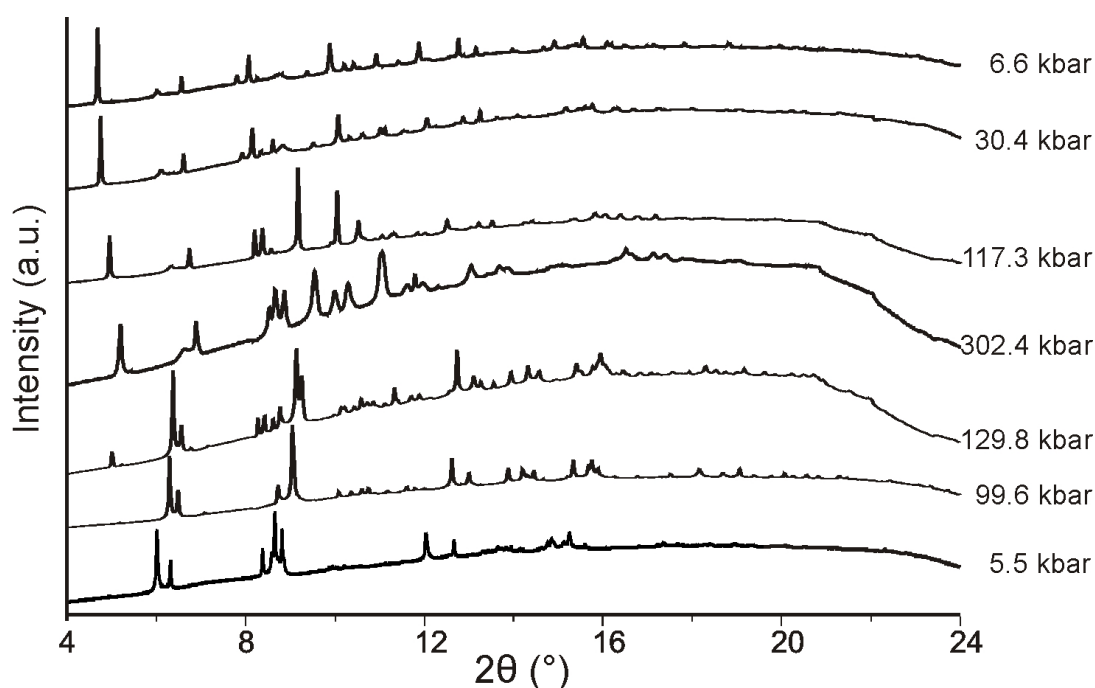


Figure 4.20 The high pressure synchrotron data for NaCuF₃ powder, obtained at ID09A beamline of ESRF, Grenoble. From bottom to top, the pressure increase first from 5.5 kbar to 302.4 kbar, then drop to lower pressure again.

4.3.8 Calculation of the spin exchange interactions of AgCuF₃ and NaCuF₃

The spin exchange parameters J_{12} and J_{34} of AgCuF₃ and NaCuF₃ are evaluated by carrying out appropriate electronic structure calculations [95].

In the spin dimer analysis, the $(\Delta\varepsilon)^2$ values obtained from EHTB calculations are summarized in Table 4.5, where $\Delta\varepsilon$ is the energy difference between the two magnetic orbitals representing the spin dimer. The $(\Delta\varepsilon)^2$ values reveal that the average of the J_{12} and J_{34} interactions is stronger for AgCuF₃ than for NaCuF₃ by a factor of ~ 1.4 , in reasonable agreement with the experimental estimate of 1.6. Furthermore, for both AgCuF₃ and NaCuF₃, J_{34} is calculated to be slightly stronger than J_{12} . This is consistent with the fact that the average Cu-F bond length is shorter, while the \angle Cu-F-Cu bond angle is slightly greater, for both AgCuF₃ and NaCuF₃.

4.4 Conclusion

The new triclinic perovskite AgCuF₃ prepared in this work is isostructural with NaCuF₃. In the structures of both compounds, the CuF₃ network of corner-sharing CuF₆ octahedra shows a cooperative Jahn-Teller distortion such that their magnetic properties above 50 K are well described by the $S = 1/2$ Heisenberg uniform antiferromagnetic chain model assuming only the nearest neighbor interactions with the average antiferromagnetic spin exchange $J/k_B = -300$ and -180 K, respectively. The observation that AgCuF₃ has stronger intrachain antiferromagnetic interactions than NaCuF₃ is consistent with the geometrical parameters associated with their Cu-F-Cu superexchange paths, and is well reproduced by a spin dimer analysis based on EHTB calculations. Powder neutron diffraction data show good agreement with the susceptibility data on the critical temperature T_N indicating long-range magnetic ordering. The Rietveld refinements of the magnetic structure of both compounds are hindered by the low symmetry of the structure and impurities. The high pressure synchrotron data for NaCuF₃ suggests an incomplete and irreversible phase transition at about 130 kbar. A possible monoclinic unit cell is given, and further search for a suitable model is needed in the future to solve the structure of the new phase.

Chapter 5

Physical properties of two dimensional Cs_2AgF_4 : Spin exchange of Ag^{2+} in layered Cs_2AgF_4 and dimers in $\text{Ag}_2\text{ZnZr}_2\text{F}_{14}$

5.1 Introduction

The oxidation state +2 for Ag is rather unusual in contrast to its lighter homologue Cu and only a few Ag(II) oxides and Ag(II) fluorides are known so far. The ternary layered fluoride Cs_2AgF_4 was first synthesized by Odenthal in 1974 [96]. It crystallizes in the K_2NiF_4 -type structure, behaving as a 2D square-lattice Heisenberg ferromagnet [97]. Structurally similar compounds include the antiferromagnets K_2CuF_4 [98], Rb_2MnF_4 [97] and La_2CuO_4 , which becomes superconducting when slightly doped with O or Sr [98, 99].

The magnetic behavior of Cs_2AgF_4 has attracted the attention because of its unusual magnetic properties [100]. It can be well modeled as a 2D Heisenberg ferromagnet described by the Hamiltonian $H = J\sum_{ij}S_i \cdot S_j$ with intralayer coupling $J/k_B = 44$ K, in sharp contrast to the antiferromagnetism of La_2CuO_4 . In addition, magnetic transition below $T_C \approx 15$ K was observed with no spontaneous magnetization in zero field (ZF) and a small saturation magnetization (~ 40 mT), suggesting the existence of a weak interlayer coupling. The electronic structure of Cs_2AgF_4 has been extensively investigated, and an explanation based on orbital order [101-105] and Ag-F covalency [106] has been proposed for the origin of this particular ferromagnetism. Muon-spin relaxation experiments have shown evidence for the magnetic order in Cs_2AgF_4 with an exchange anisotropy of $|J'/J| = 1.9 \times 10^{-2}$ for the ratio of inter- to intraplane coupling and the critical behavior intermediate in character between 2D and 3D [107]. First principle calculations for the Jahn-Teller distortion induced orbital order in Cs_2AgF_4 have been carried out, suggesting possible optical and conductivity experiments for confirming such orbital order indirectly [108].

In order to study the physical properties of Cs_2AgF_4 for a deeper understanding, here we present our work on Cs_2AgF_4 , which was prepared via a solid state reaction of AgF_2

and CsF. For the first time, the specific heat, EPR and optical measurements for Cs₂AgF₄ have been carried out.

5.2 Experimental section

5.2.1 Sample preparation

The layered fluoride Cs₂AgF₄ was prepared by a solid-state reaction of the stoichiometric mixtures of AgF₂ and CsF. Due to the extreme sensitivity of the reagents and products to air, all manipulations were carried out using the Schlenk technique or an argon-filled glovebox. In a typical preparation, Cs₂AgF₄ was prepared from a mixture of finely dispersed powders of AgF₂ and CsF (total weight 899.5 mg). The mixture was heated at 603 K for 12 h followed by slow cooling at a rate of 35 K/min.

5.2.2 Sample characterization

The product has been characterized by means of powder XRD, temperature and field dependent magnetizations ($0 \text{ T} < B_{\text{ext}} < 7 \text{ T}$), specific heat, EPR and UV-Vis diffuse reflectance.

5.3 Results and discussions

5.3.1 Crystal structure

Cs₂AgF₄ has modena color, and it immediately turns black when exposed to moisture, which provides an efficient indicator for traces of moisture in the samples. Cs₂AgF₄ crystallizes in the space group *I*4/*mmm* with $a = 4.581(1) \text{ \AA}$ and $c = 14.186(1) \text{ \AA}$. Figure 5.1 shows the Rietveld refinement of the X-ray powder diffraction pattern using TOPAS. The crystallographic data and results of the Rietveld refinements are listed in Table 5.1. The crystal structure of Cs₂AgF₄ is displayed in Figure 5.2. Layers of corner-sharing AgF₆ octahedra are stacked in *c*-direction. Each octahedron is surrounded by 8+2 Cs⁺ ions. The octahedra are compressed along the *c*-direction with an interlayer distance of 7.096 Å. Selected bond distances are shown in Table 5.2, which illustrates that each Cs ions is surrounded by 9 F ions.

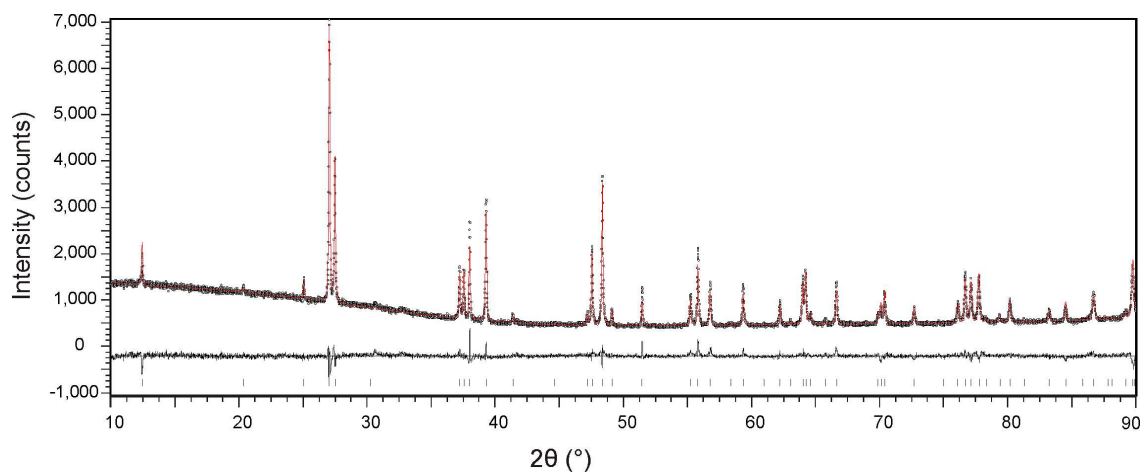


Figure 5.1 Rietveld refinement of Cs_2AgF_4 XRD data. The black dots represent the calculated pattern, red line represents the observed pattern, gray line shows the difference pattern and vertical bars indicate reflection positions.

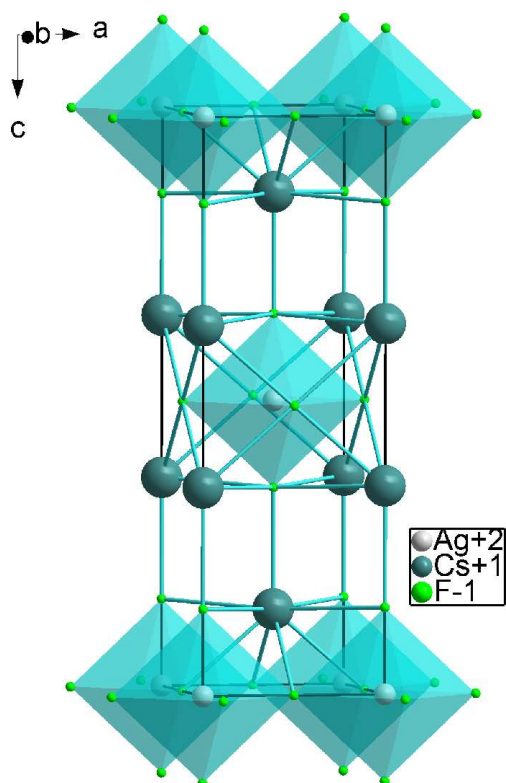


Figure 5.2 Crystal structure of Cs_2AgF_4 .

Table 5.1 Crystallographic data of Cs₂AgF₄.

Crystal system	tetragonal
Space group	<i>I4/mmm</i> (139)
<i>Z</i>	2
<i>a</i> (Å)	4.581(1)
<i>c</i> (Å)	14.186(1)
<i>V</i> (Å ³)	297.73(1)
Temperature (K)	298
formular weight (g mol ⁻¹)	440.67
ρ -calc (g/cm ³)	5.016
Wavelength (Å)	1.540596
<i>R</i> -exp (%) [*]	3.63
<i>R</i> -p (%) [*]	5.58
<i>R</i> -wp (%) [*]	8.36
Goodness of fit (%) [*]	2.30
Starting angle (°2 θ)	10
Final angle (°2 θ)	90
Step width (°2 θ)	0.01
No. of variables	25

^{*} *R*-exp, *R*-p, *R*-wp, and Goodness of fit as defined in TOPAS (Bruker AXS).

Table 5.2 Selected bond distances of Cs₂AgF₄.

Atom	Distance (Å)	Atom	Distance (Å)
Ag1- F1	2.282(13) ×2	Cs1- F1	2.767(13) ×1
F2	2.2906 ×4	F2	3.0699 ×4
Cs1	3.8001 ×8	F1	3.2424 ×4

5.3.2 Magnetic susceptibility

Temperature and field dependent measurements of the magnetic moment ($0 \text{ T} < B_{\text{ext}} < 7 \text{ T}$) of Cs_2AgF_4 were performed using a MPMS SQUID magnetometer. The inverse static molar magnetic susceptibility of polycrystalline Cs_2AgF_4 is shown in Figure 5.3. The fitting according to Curie-Weiss law shown as red line provides $\mu_{\text{eff}} = 1.850 \mu_{\text{B}}$ and Weiss temperature $\theta = 29.15 \text{ K}$, with χ_0 fixed at $-1.0 \times 10^{-4} \text{ cm}^3 \text{ mol}^{-1}$, which is obtained from $\chi_{\text{dia}} = -1.23 \times 10^{-4} \text{ cm}^3 \text{ mol}^{-1}$ diminished by the Van Vleck paramagnetism. Our results are consistent with the earlier data from McLain et al [100]. The behavior is characteristic for a ferromagnet rather than for an antiferromagnet such as K_2CuF_4 and Rb_2MnF_4 . This magnetic property of Cs_2AgF_4 can be described by the Hamiltonian, $H = -J_{ij} \sum S_i \cdot S_j$, where $J > 0$ is the exchange constant, mainly in plane, and S_i and S_j are $S = 1/2$ spin operators of nearest-neighbor Ag^{2+} ions. The inset in Figure 5.3 shows the temperature dependence of the magnetization with a Curie transition at $T_{\text{C}} = 14.5 \text{ K}$ with the external field of 100 Oe. As an ideal 2D Heisenberg magnet does not undergo a 3D magnetic ordering [109], this transition is related to a magnetic ordering of the ferromagnetic AgF_4 layers.

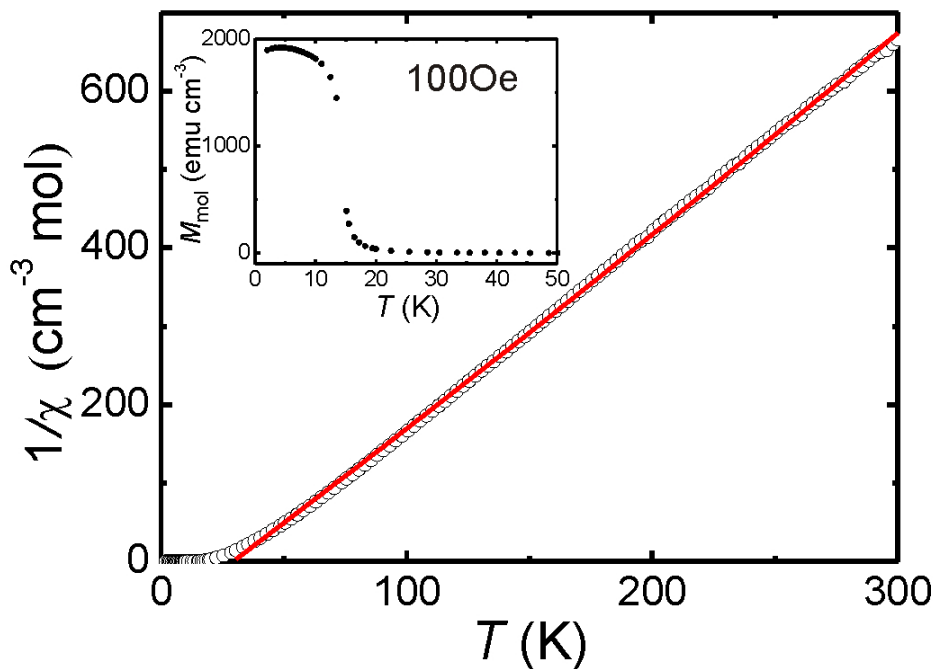


Figure 5.3 Temperature dependence of the inverse molar magnetic susceptibility of Cs_2AgF_4 in a magnetic field of 100 Oe. The red line is the fitted curve from Curie-Weiss law; inset shows the temperature dependence of molar magnetization.

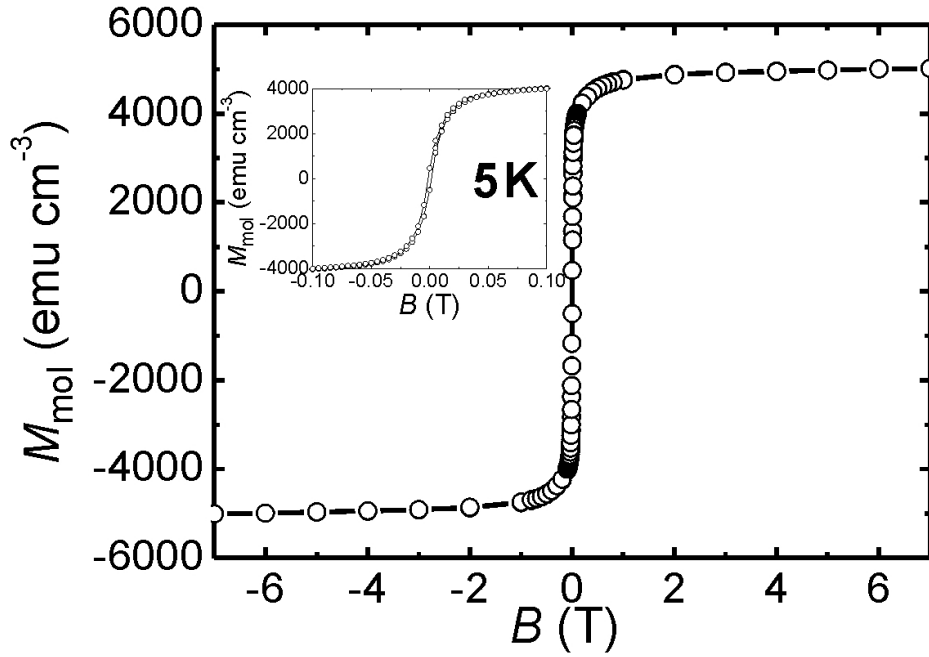


Figure 5.4 The hysteresis curve at $T = 5$ K (open circles) for Cs_2AgF_4 ; the inset shows the curve in fields between -500 and 500 Oe in detail, the line is a guide for the eye.

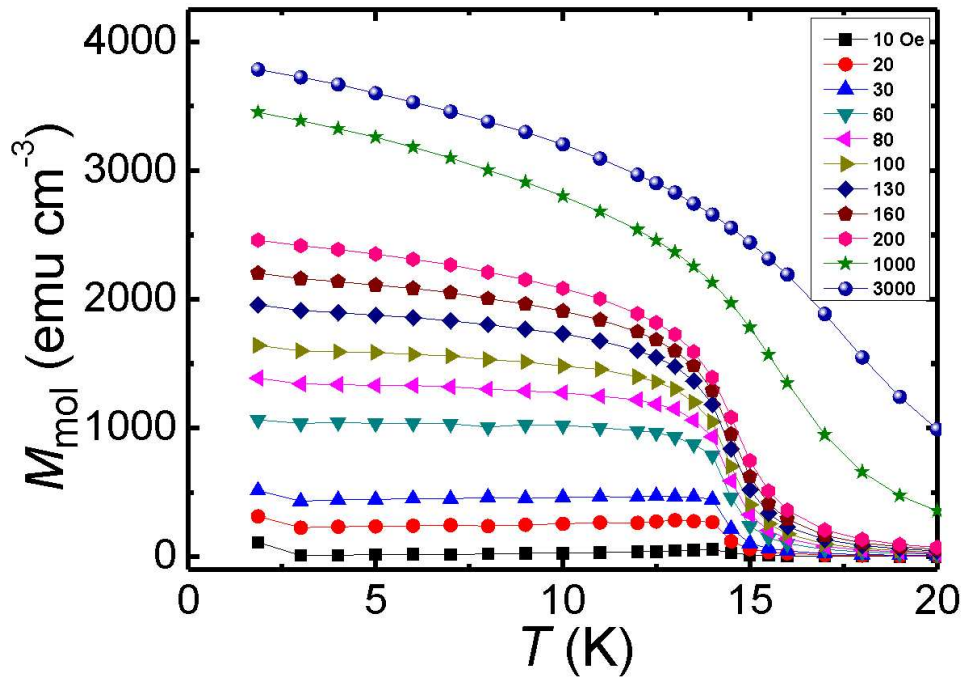


Figure 5.5 Temperature dependence of the magnetization at different magnetic fields, lines are a guide for the eye only.

The hysteresis loop in Figure 5.4 demonstrates that Cs_2AgF_4 is a soft magnet. The figure shows nearly no spontaneous magnetization at $B = 0$, which implies the antiferromagnetic coupling between layers, in good agreement with the temperature dependence of the inverse molar susceptibility shown in Figure 5.3. This coupling is weak as indicated by saturation near 500 Oe, and shows that the magnetism in this system has the character of mainly 2D. The magnetic moment per Ag^{2+} is found to be $\sim 0.9 \mu_B$ at the saturated magnetization.

To explore the nature of the interlayer interaction in Cs_2AgF_4 below T_C , we have examined the temperature dependence of its magnetization under the external magnetic field ranging from 10 to 3000 Oe. Our results summarized in Figure 5.5 show that the magnetic saturation of Cs_2AgF_4 increases steadily with increasing the applied magnetic field. Furthermore, with increasing the magnetic field, the phase transition becomes more smeared out and the magnetization upturn occurs at a higher temperature in a magnetic field higher than 200 Oe.

5.3.3 Specific heat

In order to analyze the field dependence of the ferromagnetic transition, for the first time we have performed the specific heat measurements of Cs_2AgF_4 (powder sample) at various magnetic fields, which show more sensitivity to the transition. The anomaly observed at $T_C = 14.2$ K shown in the inset of Figure 5.6 is due to the onset of interlayer coupling, and this is consistent with the magnetic susceptibility data.

As shown in Figure 5.6, when increasing the external field from zero (black circles), the anomaly becomes smaller without shifting its position, and it disappears when the field is higher than 200 Oe, implying that the interlayer antiferromagnetic exchange might transform into ferromagnetic at higher external fields. This means that increasing the extent of interlayer ferromagnetic coupling reduces the specific heat anomaly, given the field dependence of the magnetization vs. temperature discussed in the previous section. The field dependence of the specific heat anomaly is reversible. When the applied field is removed, the anomaly (green triangles) returns practically with no change in shape from that (black squares) observed before applying an external field.

Figure 5.7 shows the plot of C_p/T vs. T^2 . According to the previous prediction of the low-temperature behavior of 2D systems [94], there should be a linear relationship between C_p and T^2 for a 2D ferromagnet, which is in rather good agreement with our result at temperatures below T_C .

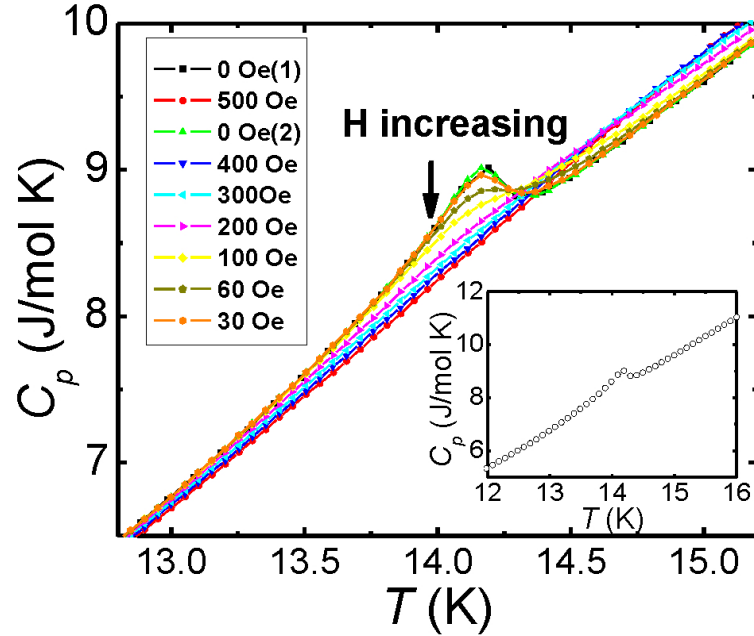


Figure 5.6 Temperature dependence of the specific heat in different fields in a range from 0 to 3000 Oe, 0 Oe (1) and 0 Oe (2) are the zero field at the beginning and end of the variation of the external field, respectively. The lines are a guide for the eye only. Inset: the specific heat with an anomaly at $T_C = 14.2$ K at zero field.

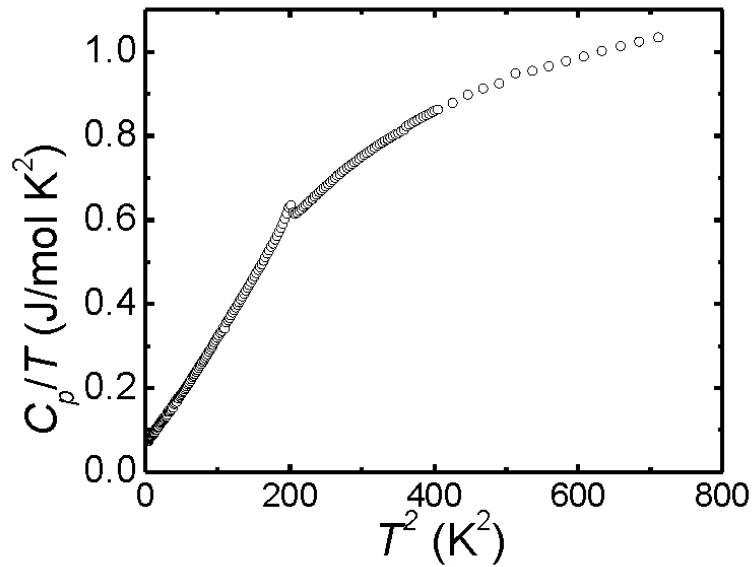


Figure 5.7 The temperature dependence of the specific heat, showing an approximate linear relationship between C_p/T vs. T^2 below T_C .

5.3.4 Electron paramagnetic resonance

In order to obtain more detailed information about spin exchange in Cs_2AgF_4 , EPR measurements have been carried out at different temperatures. The detected spectra are shown in Figure 5.8. At high temperature the EPR spectrum is dominated by one isotropic signal from Ag^{2+} ions, which is similar to that observed in AgCuF_3 in the previous chapter. At lower temperature it shows the superposition of the Cu^{2+} EPR spectrum with another isotropic EPR signal which rapidly intensifies with a larger line width upon lowering the temperature, especially on the high-field side. The second signal might be related to the anisotropy of the EPR parameters, but could also originate from paramagnetic impurities or indicate a resonance mode resulting from the onset of the internal field.

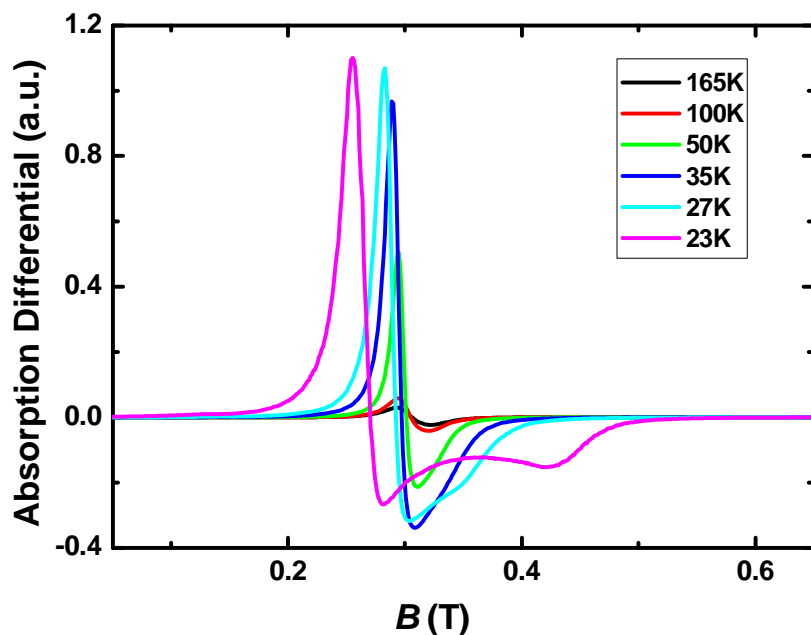


Figure 5.8 Temperature dependence of EPR signal for Cs_2AgF_4 .

Figure 5.9 shows the analytic results of EPR spectra for Cs_2AgF_4 . The signal below 100 K has an unusual shape and becomes more asymmetric. As a consequence the signals observed at $T > 100\text{K}$ could be nicely fitted with a single Lorentzian line (red line in inset) providing the EPR parameters, line width and g factor ($g = \mu_B B_0 / h\nu$, B_0 - resonance field). In Figure 5.9 a typical EPR signal at $T = 155\text{K}$ (inset) and the temperature behavior of the line width (top panel) for Cs_2AgF_4 are shown.

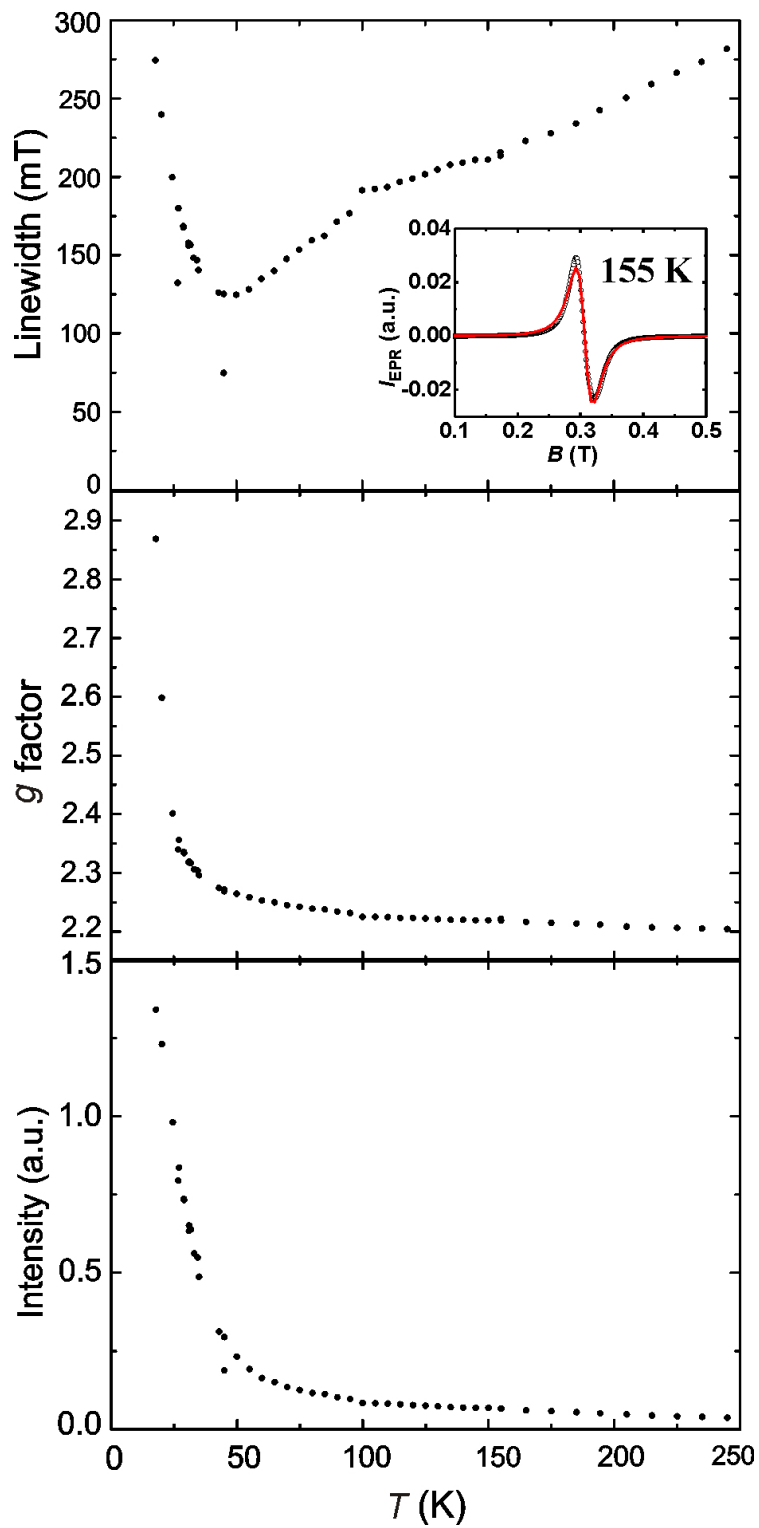


Figure 5.9 The temperature dependence of the line widths for the EPR signals is shown for Cs_2AgF_4 in the top main panel. The inset shows a typical EPR signal (black circles) with a Lorentzian fit (red line). The two lower panels show the temperature dependence of the g factor (middle) and the intensity of the EPR signal (bottom panel) for Cs_2AgF_4 .

The two lower panels show the temperature behavior of the EPR intensity and the measured g factor. The observed g factors of ≈ 2.20 ($\mu_{\text{eff}} \approx 1.905 \mu_{\text{B}}$) at higher temperature are reasonable for Ag^{2+} in a distorted octahedral environment, and this is in fair agreement with the static susceptibility fitted by the Curie-Weiss law. In the temperature range below 50 K the g value exhibits a rapid change reaching the values of 2.87 at $T = 17.8$ K, while the integral intensity continuously increases reaching the largest values at the lowest temperature. Additionally, the line width increases with decreasing temperature as well but shows a minimum at about 50 K, similar to the temperature variation of the Cu^{2+} EPR spectrum of the sample AgCuF_3 .

5.3.5 UV-Vis diffuse reflectance

The modena color of Cs_2AgF_4 calls for a detailed study of its optical spectra. The UV-vis diffuse reflectance spectra of Cs_2AgF_4 in the range of 200 - 800 nm at room temperature are shown in Figure 5.10. For a check of the sample safety, the color of Cs_2AgF_4 is also a good indicator, and after the measurement the color did not alter. Since the sample holder was not air-tight enough for the air-sensitive Cs_2AgF_4 , a measurement of the sample shortly exposed in air has been done as well, the spectrum of which has shown almost no overlap with the absorption bands from the Argon-protected one (black in Figure 5.10).

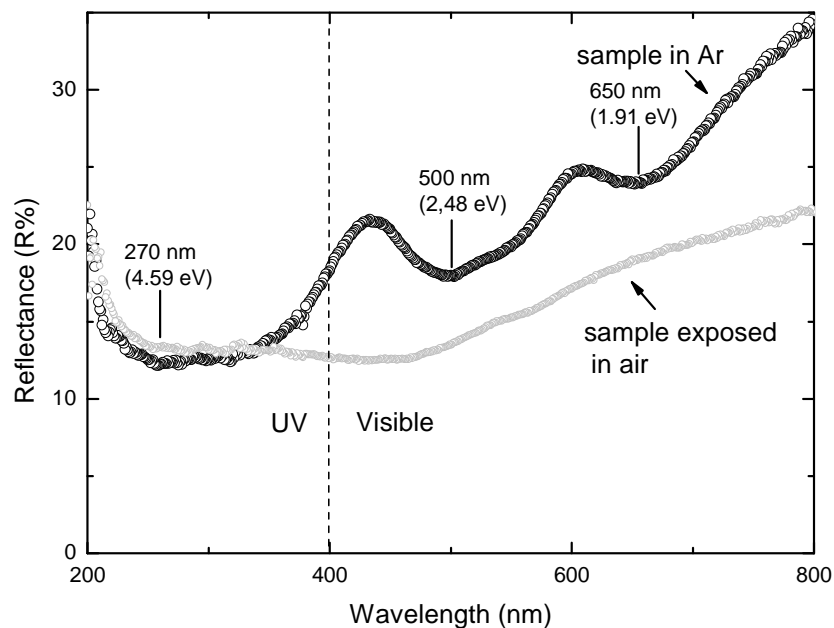


Figure 5.10 UV-Vis diffuse reflectance of two Cs_2AgF_4 samples: in Ar (black) and shortly exposed in air (gray).

Cs_2AgF_4 exhibits absorption in visible light as well as in the UV range. The reflectance coefficient is ~35% at 800 nm. In the visible region from the main absorption edge a dip is seen at 500 nm with a decreased reflectance coefficient of 24%. Via the relation between wavelength and absorption energy [110],

$$\lambda_g \text{ (nm)} = 1240/E_g \text{ (eV)} \quad \text{Eq. 5.1}$$

a gap energy of 2.48 eV has been obtained, which is in astonishingly good agreement with the previously calculated band gap of about 2.5 eV for Cs_2AgF_4 [111], and this corresponds to the modena color of Cs_2AgF_4 . Another dip in this region from the main absorption edge is also recorded at 650 nm (1.91 eV) probably due to the absorption band of interstitial Cs^+ ions [112], which needs to be validated from calculations in the future.

In the UV part of the reflectance spectrum a more intensive broad band exists in the region 200 – 370 nm, centered at about 270 nm, possibly originating from the electron transfer from the valence to the conduction band, and accompanied by the decrease of the reflectance coefficient to ~12%. This band could be assigned to the charge transfer band (CTB) of $\text{F}^- \rightarrow \text{Ag}^{2+}$ [111, 113, 114].

Radwanski et al. have claimed that the insulating gap for Cs_2AgF_4 should be much larger, say 4 - 5 eV, and that a $d-d$ excitation of 2.0 - 2.3 eV related to the $t_{2g}-e_g$ promotion energy (= 10 Dq) is a reason for the modena color of Cs_2AgF_4 [115].

The optical absorption near the band edge follows the equation [116, 117]:

$$\alpha = A(h\nu - E_g)^{n/2}/h\nu \quad \text{Eq. 5.2}$$

where α , ν , E_g , A , and n are the absorption coefficient, incident light frequency, band gap, constant, and an integer, respectively. The integer n depends on the characteristics of the optical transition ($n = 1, 2, 4$ and 6). The value of n as determined for Cs_2AgF_4 is 1, indicating that a direct optical transition can occur with no significant change in the wave vector. The $(\alpha h\nu)^2$ versus $h\nu$ curve for Cs_2AgF_4 is illustrated in Figure 5.11. The optical band gap for Cs_2AgF_4 was estimated to be about 2.17 eV by this method, which is roughly in correspondence with the estimated direct band gap of 2.5 eV [111].

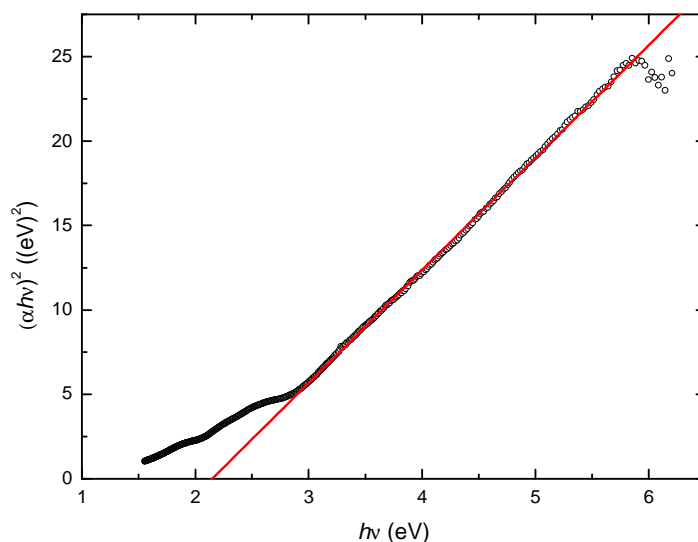


Figure 5.11 The $(\alpha hv)^2$ versus hv curve of Cs_2AgF_4 .

5.4 Spin exchange of Ag^{2+} in dimers in $\text{Ag}_2\text{ZnZr}_2\text{F}_{14}$

In order to study the exchange interaction of $[\text{AgF}_4]^{2-}$ with Ag^{2+} in d^9 configuration, we have chosen a Zn-substituted $\text{Ag}_3\text{Zr}_2\text{F}_{14}$, i.e. $\text{Ag}_2\text{ZnZr}_2\text{F}_{14}$, in which Zn has substituted one of the Ag atom positions, leaving pure Ag^{2+} dimers. The powder sample of $\text{Ag}_2\text{ZnZr}_2\text{F}_{14}$ was prepared by Kraus according to B. Müller [118]. It has violet color, and decomposes into white powder when heated to 200 °C in vacuum.

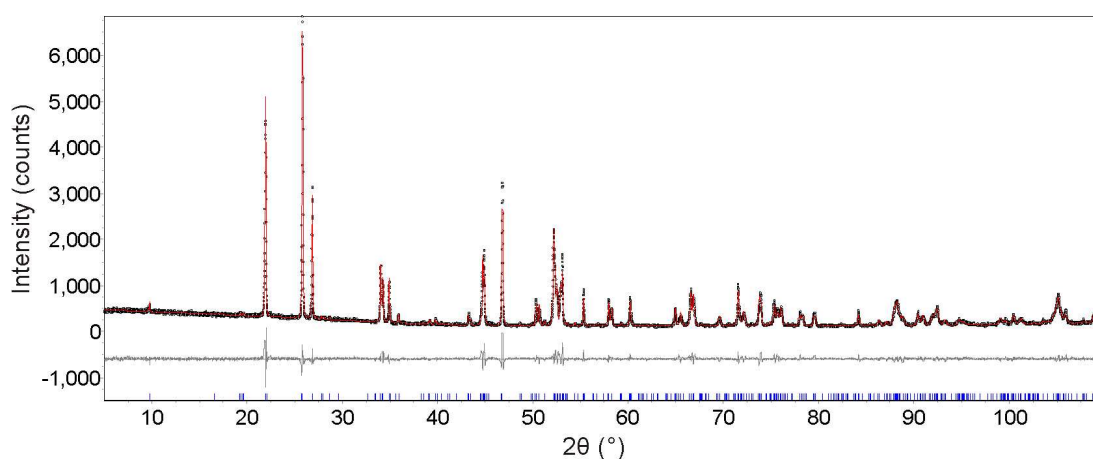


Figure 5.12 Rietveld refinement of XRD data for $\text{Ag}_2\text{ZnZr}_2\text{F}_{14}$. The black dots represent the calculated pattern, red line represents the observed pattern, gray line shows the difference pattern and blue vertical bars indicate reflection positions.

$\text{Ag}_2\text{ZnZr}_2\text{F}_{14}$ crystallizes in the space group $C2/m$ with $a = 9.0204(1)$ Å, $b = 6.6372(1)$ Å, $c = 9.0564(1)$ Å and $\beta = 90.45(1)^\circ$, isotypic to $\text{Ag}_3\text{Zr}_2\text{F}_{14}$. Figure 5.12 shows the Rietveld refinement of the X-ray powder diffraction pattern using TOPAS [35]. The crystallographic data and results of the Rietveld refinements are listed in Table 5.3.

Table 5.3 Crystallographic data of $\text{Ag}_2\text{ZnZr}_2\text{F}_{14}$.

Compound	$\text{Ag}_2\text{ZnZr}_2\text{F}_{14}$
Temperature (K)	298
Formula weight (g/mol)	729.57
Space group	$C2/m$ (12)
Z	2
a (Å)	9.0204(1)
b (Å)	6.6372(1)
c (Å)	9.0564(1)
β (°)	90.45(1)
V (Å ³)	542.196(12)
ρ -calc (g/cm ³)	4.469
Wavelength (Å)	1.54052
R -exp (%) [*]	5.98
R -p (%) [*]	6.97
R -wp (%) [*]	9.31
R -F ² (%) [*]	1.56
Starting angle (°2 θ)	5
Final angle (°2 θ)	110
Step width (°2 θ)	0.01
No. of variables	62

^{*} R -exp, R -p, R -wp, and R -F² as defined in TOPAS (Bruker AXS)

The crystal structure of $\text{Ag}_2\text{ZnZr}_2\text{F}_{14}$ is displayed in Figure 5.13. Atomic coordinates are given in Table 5.4. Each Zn atom is surrounded by 4+2 F^- ions and forms a compressed octahedron. All the octahedra are separated from each other but form planes parallel to the ab plane. Between these planes are AgF_4 squares, which further form Ag dimers, Ag_2F_7 . Zr atoms connect the Zn octahedra and Ag dimers through F-Zr-F bridges.

In the previous publication [118] $\text{Ag}_2\text{CuZr}_2\text{F}_{14}$ was reported to be isotypic to $\text{Ag}_3\text{Zr}_2\text{F}_{14}$, where there are two different Ag positions, octahedrally and quadrangulary coordinated with a ratio of 1:2. In the crystal structure of $\text{Ag}_2\text{CuZr}_2\text{F}_{14}$ both Ag and Cu atoms occupy the two Ag positions with an occupation factor of 2/3 and 1/3 respectively.

Alternatively, in our Zn analogue, $\text{Ag}_2\text{ZnZr}_2\text{F}_{14}$, Zn substitutes the Ag atom at the octahedrally coordinated position, leaving the two Ag atoms forming dimers at the quadrangulary coordinated position. In the structure refinement, the occupation factors of the two different Ag sites have been refined. The result shows that the Zn occupancy at the octahedral site is close to 100%, thus supporting our proposed ordering of Zn and Ag.

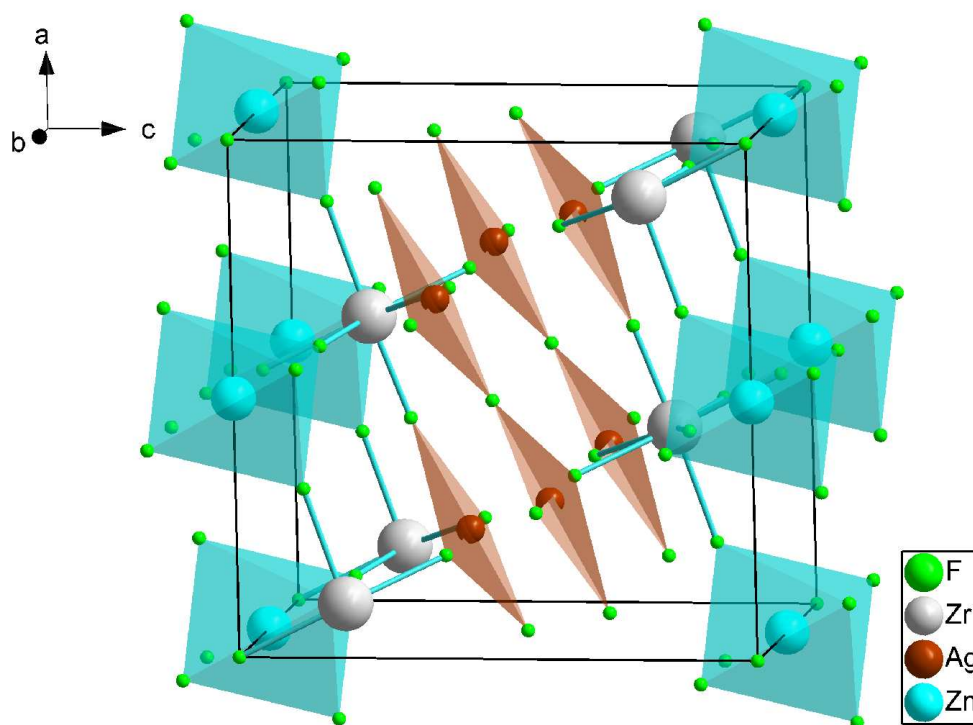


Figure 5.13 Crystal structure of $\text{Ag}_2\text{ZnZr}_2\text{F}_{14}$.

Table 5.4 Positional parameters and isotropic atomic displacement parameters for $\text{Ag}_2\text{ZnZr}_2\text{F}_{14}$.

Atom	x/a	y/b	z/c	$B_{\text{eq}}(\text{\AA}^2)$
Zn1	0	0.5	0	0.22(4)
Ag1	0.30514(35)	0	0.60631(28)	0.22(4)
Zr1	0.10511(40)	0	0.20737(33)	0.22(4)
F1	0.0790(11)	0.2953(13)	0.1450(11)	0.22(4)
F2	0.1813(14)	0.1714(11)	0.3831(12)	0.22(4)
F3	0.0905(19)	0	0.7168(15)	0.22(4)
F4	0.3264(14)	0	0.1311(14)	0.22(4)
F5	0	0.5	0.5	0.22(4)
F6	0	0	0	0.22(4)

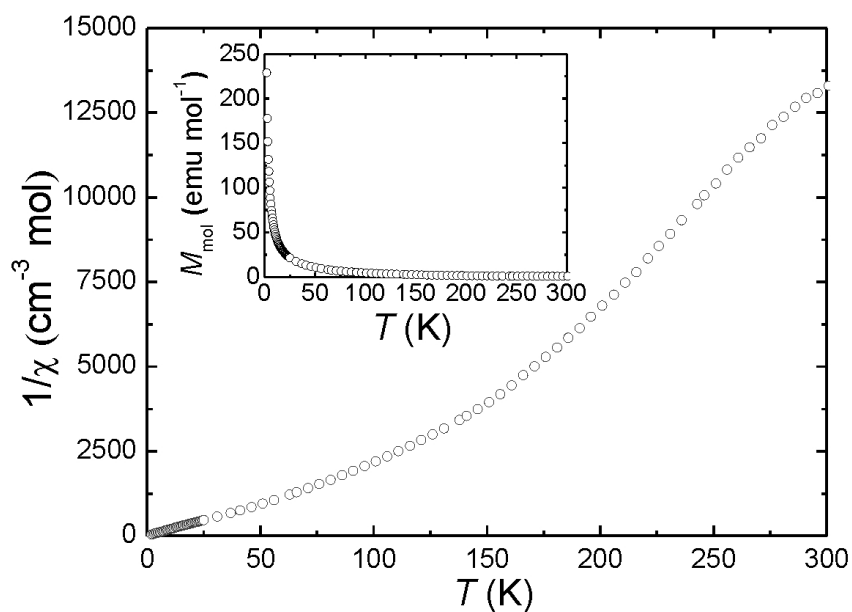


Figure 5.14 Temperature dependence of the inverse molar susceptibility of $\text{Ag}_2\text{ZnZr}_2\text{F}_{14}$ at a magnetic field of 1 T; inset shows the temperature dependence of molar magnetization.

In order to examine interesting magnetic properties originating from the Ag^{2+} dimer, temperature and field dependent measurements of the magnetic moment ($0 \text{ T} < B_{\text{ext}} < 7 \text{ T}$) of $\text{Ag}_2\text{ZnZr}_2\text{F}_{14}$ were performed using a MPMS SQUID magnetometer. The inverse molar magnetic susceptibility and molar magnetization of polycrystalline $\text{Ag}_2\text{ZnZr}_2\text{F}_{14}$ are shown in Figure 5.14. The magnetic moment is too small, thus it is believed that the single spins of Ag^{2+} have strong coupling in the Ag_2F_7 dimers, causing the magnetic moment of individual Ag^{2+} to disappear. From the high temperature region of the inverse molar magnetic susceptibility data as a function of temperature, one can estimate with the Curie-Weiss law that a very large negative θ value will be obtained indicating a strong coupling of Ag^{2+} in the dimers as well, which is in good agreement with calculation performed by M.-H. Whangbo [119].

5.5 Conclusion

In summary, we have prepared the layered Ag^{2+} fluoride Cs_2AgF_4 through a solid-state reaction and measured the magnetic properties and specific heat. A ferromagnetic transition has been observed at $T_C = 14.5 \text{ K}$. The low saturation value near 500 Oe in the hysteresis curve at $T = 5 \text{ K}$ implies an antiferromagnetic coupling between layers. What is more unusual is that the $T_C = 14.2 \text{ K}$ at zero field found in the specific heat measurement has a field dependent behavior. It disappeared after applying a magnetic field larger than 200 Oe, implying that the interlayer antiferromagnetic exchange might transform into ferromagnetic. The measurement of the UV-vis diffuse reflectance reveals Cs_2AgF_4 as an insulator with a band gap of 2.48 eV, in good agreement with the calculated band gap of about 2.5 eV. Nevertheless, the interpretation of the special features in the spectra of Cs_2AgF_4 is still open.

We have studied another Ag^{2+} fluoride, a powder sample of $\text{Ag}_2\text{ZnZr}_2\text{F}_{14}$. In its crystal structure Zn has substituted one of the Ag atom positions in $\text{Ag}_3\text{Zr}_2\text{F}_{14}$, leaving pure Ag^{2+} dimers. The high temperature region of the inverse molar magnetic susceptibility data indicates a strong coupling of Ag^{2+} in the Ag_2F_7 dimers, the calculation will be given in the future.

Chapter 6

Reactions of CsF and compounds with tetrahedral molecules

6.1 Introduction

CsF has the strong tendency to form fluoride complexes, and easily includes molecules like H₂O or Br₂ [26]. During the reaction between nitriles and bromine in presence of CsF, it was found that CsF could absorb bromine [120, 121]. Subsequent investigations of Seppelt et al. [26] revealed that an intercalation compound CsF·Br₂ with layers of CsF squares separated by layers of Br₂ molecules, which oriented perpendicular to the CsF layers, could be prepared from CsF and Br₂. Ab initio calculations by Ruiz and Alvarez indicate that CsF·I₂ might be another possible intercalate as well [122]. A more CsF-rich compound, 2CsF·Br₂, was later prepared by Seppelt, composed of two layers of CsF followed by one layer of bromine molecules [27]. The inclusion of halogen into the lattice of CsF is unique in that halogen molecules transform the cubic lattice of CsF into a layered structure and intercalate between the ionically bound layers of CsF. This compares to being placed in the van der Waals gaps of a 2D lattice as in graphite, or occupying cages or channels in a 3D structures as in zeolite intercalates.

The question arises, whether it is possible to include tetrahedral molecules, e.g. OsO₄ and P₄, into the CsF lattice. Osmium tetroxide, one of the most well-known compounds of osmium, has a molecular structure with the O-Os-O bond angles around 109.5° in the tetrahedral OsO₄ molecule, and these molecules pack in a crystal to form the CF₄ type structure. It is an example for the highest oxidation state (VIII) in a compound. This extremely toxic crystalline solid with clear yellow color has the low m.p. = 40 °C, b.p. = 130 °C and high volatility. OsO₄ can oxidize the halides and expands its coordination number, and it can also be converted easily to osmium (VIII) compounds with higher coordination number, e.g. OsO₃F₂ [123].

Phosphorus has several allotropes with different colors, and they possess remarkably different properties [124]. The two most common allotropes are white (yellow) phosphorus and red phosphorus. Other forms include violet phosphorus, scarlet phosphorus and black phosphorus. White phosphorus has three forms, high-temperature α ,

low-temperature β and γ forms [125]. They all contain a P_4 tetrahedron as a structural unit, in which each atom is bound to the other three atoms by a single bond. White phosphorus is highly flammable and pyrophoric (self-igniting) upon contact with air as well as toxic, and it will gradually transform to red phosphorus. Only the black phosphorus is thermodynamically stable at normal condition.

Here we present studies of the possibilities of the inclusion of tetrahedral molecules, i.e. OsO_4 and P_4 , into the CsF lattice.

6.2 CsF+OsO₄

6.2.1 Sample preparation and characterization

All manipulations were carried out using Schlenk technique or an argon-filled glove box. CsF and OsO_4 were mixed in a stoichiometry of 4:3, sealed in a Duran glass tube and then heated at 280°C for 7 days. Deep brown microcrystals of $Cs_3OsO_4F_3$, which were extremely moisture sensitive, have been obtained and characterized by means of powder XRD, Raman spectroscopy and solid-state NMR.

6.2.2 Results and discussions

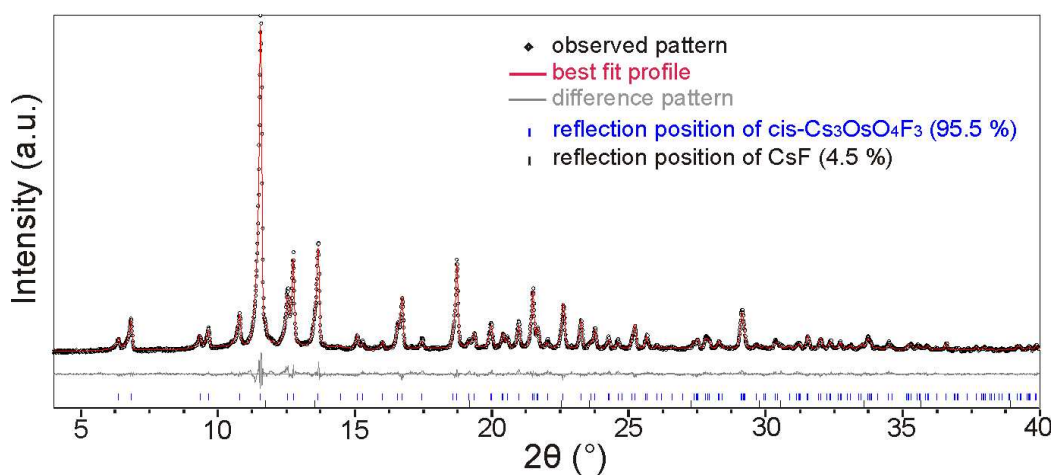
6.2.2.1 Crystal structure

The program STOE [65] was used for indexing the powder X-ray pattern of polycrystalline $Cs_3OsO_4F_3$, and a primitive tetragonal unit cell was obtained with the lattice parameters given in Table 6.1. At first glance $Cs_3OsO_4F_3$ is isotypic to Cs_3SiF_7 with the space group $P4/mbm$ [126]. But the distribution of O and F at different anion sites of $Cs_3OsO_4F_3$ was not straightforward, although there were some hints from the refinements. It is suggested that high-valent cations pick high-valent anions, indicating that all the four O atoms locate in the Os octahedra, which has been confirmed by the ^{19}F NMR results discussed later. $Cs_3OsO_4F_3$ contains, according to $Cs_3[OsO_4F_2]F$, both octahedral $[OsO_4F_2]^{2-}$ units and F atoms that are only bound to Cs atoms. The crystal structure was solved by the global optimization method of simulated annealing in real space using the TOPAS program [35]. The result of the Rietveld refinement based on the Cs_3SiF_7 structural model is shown in Figure 6.1(a), and the final agreement factors are listed in Table 6.1 under *trans*- $Cs_3OsO_4F_3$, in which two F^- ions in the $[OsO_4F_2]^{2-}$

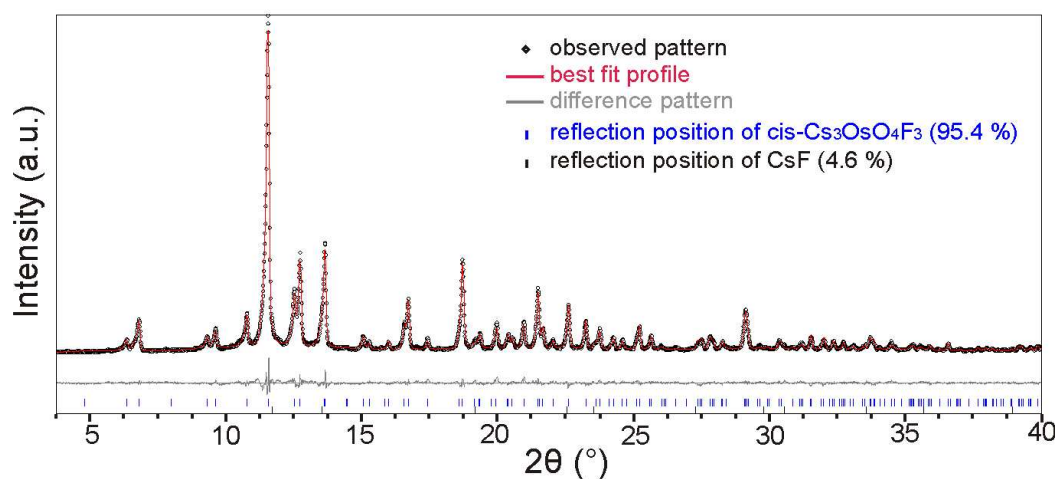
octahedron are in a *trans* position. Table 6.2 shows the atomic positions and isotropic temperature factors for *trans*-Cs₃OsO₄F₃.

In previous publications about Cs₂[OsO₄F₂] it has been claimed that the configuration of the two F⁻ ions in the [OsO₄F₂]²⁻ octahedra are in a *cis* position determined from optical spectroscopy [127, 128]. It is also suggested that in the [OsO₄F₂]²⁻ octahedra the Os=O covalency energetically tends to form more O-Os-O angles near 90°, which is found for other transition metal oxyfluoride species, such as [WO₂F₄]²⁻ and [MoO₂F₄]²⁻ [129]. This number of pairs of Os=O bonds in a 90° relationship is 4 and 5 for the *trans*- and *cis*-[OsO₄F₂]²⁻ octahedron, respectively. Therefore the space group *P4*, a subgroup of *P4/mbm*, was chosen as the second model for the structure refinement, in which the atomic positions from the first model were used and the F⁻ ions were put in a *cis* position. Meanwhile, the O/F ordering was also determined by analyzing the Os-F and Os-O bond distances [130]. A slightly better fit was successfully validated by Rietveld refinement. The final result is given in Figure 6.1(b), and the agreement factors are listed in Figure 6.2 under *cis*-Cs₃OsO₄F₃. The atomic positions and isotropic temperature factors are shown in Table 6.3. Temperature factors are fixed at 3 Å² in the refinements for both structures.

A small amount of unreacted CsF was still present in the product. This amount was refined to be 4.5% for *trans*-Cs₃OsO₄F₃ and 4.6% for *cis*-Cs₃OsO₄F₃. The *R* values shown in Table 6.1 for the both configurations are similar to each other. Further characterization is needed to determine which structure is preferable.



(a)



(b)

Figure 6.1 Powder X-ray diffraction patterns for (a) *trans*-Cs₃OsO₄F₃ and (b) *cis*-Cs₃OsO₄F₃. Shown are the observed pattern (black diamonds), the best Rietveld fits profile in *P4/mbm* for *trans*-Cs₃OsO₄F₃ and *P4* for *cis*-Cs₃OsO₄F₃ (red lines), the difference curve between observed and calculated profile (grey line), and the reflection markers (vertical bars). The wavelength is $\lambda = 0.7093 \text{ \AA}$ (MoK α).

Table 6.1 Data collection and structure refinement for the two possible structures of $\text{Cs}_3\text{OsO}_4\text{F}_3$.

Compound	<i>trans</i> - $\text{Cs}_3\text{OsO}_4\text{F}_3$	<i>cis</i> - $\text{Cs}_3\text{OsO}_4\text{F}_3$
Temperature (K)	298	298
Formula weight (g/mol)	709.92	709.92
Crystal system	tetragonal	tetragonal
Space group	<i>P4/mbm</i> (127)	<i>P4</i> (75)
Z	2	2
<i>a</i> (Å)	8.4311(2)	8.4309(2)
<i>c</i> (Å)	6.3892(2)	6.3891(2)
V (Å ³)	454.17(3)	454.14(3)
ρ -calc (g/cm ³)	5.1912(4)	5.1915(4)
Wavelength (Å)	MoK α 0.7093	MoK α 0.7093
<i>R</i> -exp (%) [*]	4.21	4.20
<i>R</i> -p (%) [*]	5.21	5.11
<i>R</i> -wp (%) [*]	6.51	6.88
<i>R</i> -F ² (%) [*]	1.55	1.55
Starting angle (°2 θ)	2	2
Final angle (°2 θ)	40	40
Step width (°2 θ)	0.02	0.02
No. of variables	44	52

^{*} *R*-exp, *R*-p, *R*-wp, and *R*-F² as defined in TOPAS (Bruker AXS)

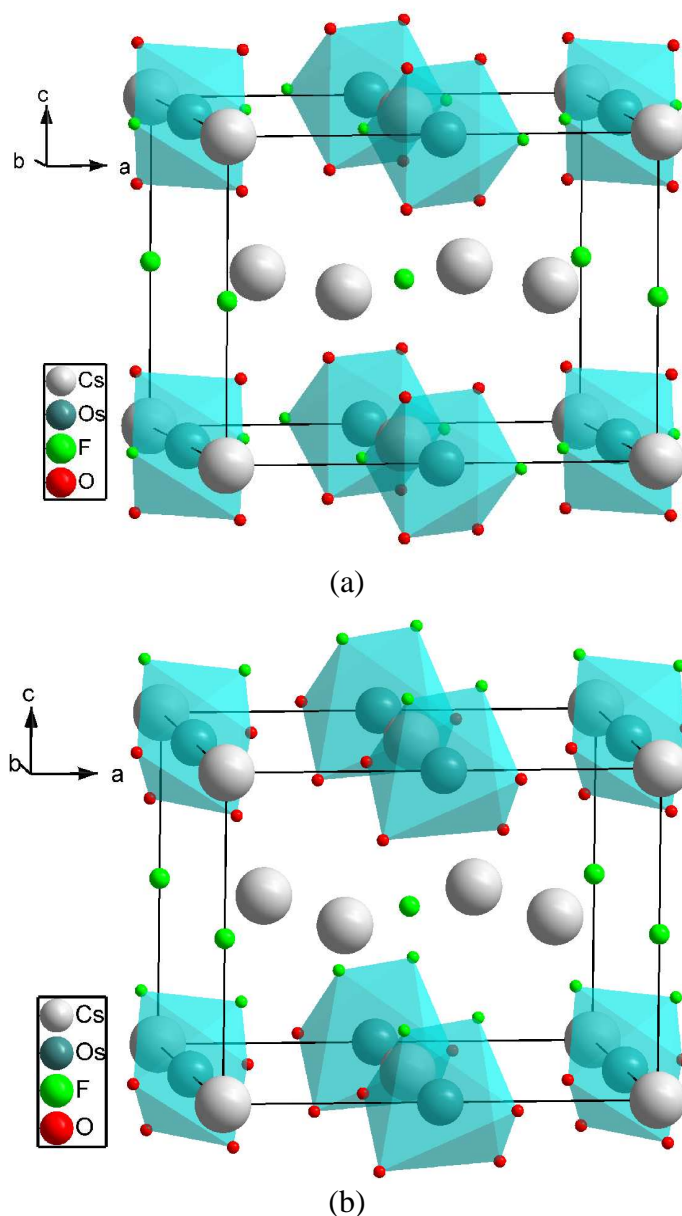


Figure 6.2 Crystal structure of the two possible structures of $\text{Cs}_3\text{OsO}_4\text{F}_3$. the turquoise octahedra are (a) $trans$ - $[\text{OsO}_4\text{F}_2]^{2-}$ units and (b) cis - $[\text{OsO}_4\text{F}_2]^{2-}$, respectively. In both structures, $[\text{Cs}_2\text{F}]$ layers are parallel to the ab plane at $c/2$.

Figure 6.2 displays the unit cells of the investigated crystal structures. For both $trans$ - and cis - $\text{Cs}_3\text{OsO}_4\text{F}_3$, layered discrete $[\text{Cs}_2\text{F}]$ (parallel to the ab plane) separates $[\text{OsO}_4\text{F}_2]^{2-}$ octahedral single layers. The $trans$ - $[\text{OsO}_4\text{F}_2]^{2-}$ octahedron is compressed along the F-Os-F bonds, with the two Os-F distances of 1.846 Å and the four equatorial Os-O distances of 1.860 Å, showing that it is very close to an ideal octahedron. However, it is contradictory with the fact that Os-F distances are normally longer than Os-O distances, which is in fact a double bond Os=O [131, 132].

In contrast, the *cis*-[OsO₄F₂]²⁻ deviates from the ideal octahedron with Os-O distances of 1.845 Å (×2) and 1.875 Å (×2). It would be realistic to assign the longest bond length 1.919 Å (×2) to Os-F bonds, because the resulting Os-F distance would be comparable to typical Os-F bonds, e.g. 1.885-2.086 Å in OsO₃F₂ or 2.048 Å in Cs₂OsO₄F₂, and that the Os-F distance is longer than Os-O distance. Selected intramolecular distances and angles in the two structures of Cs₃OsO₄F₃ are listed in Table 6.4 and Table 6.5, respectively.

Table 6.2 Positional parameters and isotropic temperature factors for *trans*-Cs₃OsO₄F₃.

Atom	Wyckoff	<i>x/a</i>	<i>y/b</i>	<i>z/c</i>	<i>B</i> _{eq} (Å ²)
Cs1	2 <i>a</i>	0	0	0	3
Cs2	4 <i>h</i>	0.1947(2)	0.6947(2)	0.5	3
Os1	2 <i>d</i>	0	0.5	0	3
O1	8 <i>k</i>	0.3949(11)	0.8949(11)	0.2152(17)	3
F1	2 <i>b</i>	0	0	0.5	3
F2	4 <i>g</i>	0.1551(12)	0.6551(12)	0	3

Table 6.3 Positional parameters and isotropic temperature factors for *cis*-Cs₃OsO₄F₃.

Atom	Wyckoff	<i>x/a</i>	<i>y/b</i>	<i>z/c</i>	<i>B</i> _{eq} (Å ²)
Cs1	1 <i>a</i>	0	0	0	3
Cs2	1 <i>b</i>	0.5	0.5	0	3
Cs3	4 <i>d</i>	0.1942(2)	0.6942(2)	0.5	3
Os1	2 <i>c</i>	0.5	0	0	3
O1	4 <i>d</i>	0.1548(15)	0.6548(15)	0	3
O2	4 <i>d</i>	0.0759(51)	0.3439(39)	0.8265(50)	3
F1	1 <i>b</i>	0.5	0.5	0.5	3
F2	1 <i>a</i>	0	0	0.5	3
F3	4 <i>d</i>	0.4099(30)	0.9099(30)	0.2488(50)	3

Table 6.4 Selected intramolecular distances (Å) and angles (°) for *trans*-Cs₃OsO₄F₃.

Os1	-F2	1.846(14) × 2	O1-Os1-O1	90.00 × 5
	-O1	1.860(12) × 4		180.00(1) × 1
Cs1	-F2	3.188(5) × 4	O1-Os1-F2	84.68(78) × 2
	-F1	3.195 × 2		90.00 × 3
Cs2	-O1	3.002(13) × 2		95.32(78) × 2
	-F1	3.053 × 2		180.00 × 1
			F2-Os1-F2	180.00(1) × 1

Table 6.5 Selected intramolecular distances (Å) and angles (°) for *cis*-Cs₃OsO₄F₃.

Os1	-O1	1.845(18) × 2	O1-Os1-O1	180.00 × 1
	-O2	1.875(34) × 2	O1-Os1-O2	75.2(12) × 2
	-F2	1.919(33) × 2		102.6(12) × 1
Cs1	-O1	3.190(6) × 4		104.8(12) × 1
	-O2	3.193(33) × 4	O1-Os1-F3	68.1(21) × 1
	-F2	3.194 × 2		
Cs2	-O1	3.190(6) × 4		96.0(12) × 1
	-F1	3.194 × 2		158.6(11) × 2
Cs3	-F3	3.015(20) × 2	O2-Os1-O2	104.8(12) × 1
	-F3	3.031(35) × 1	O2-Os1-F3	90.0 × 3
	-F2	3.054 × 1		96.0(12) × 1
	-F1	3.054 × 1	F3-Os1-F3	90.0 × 1
	-O2	3.063(39) × 1		
	-O2	3.072(37) × 1		

The $[\text{OsO}_4\text{F}_2]^{2-}$ octahedra in the two structures have been displayed along the c axis in Figure 6.3. In $\text{trans-Cs}_3\text{OsO}_4\text{F}_3$ on the left side the $[\text{OsO}_4\text{F}_2]^{2-}$ unit is close to an ideal octahedron, whereas in $\text{cis-Cs}_3\text{OsO}_4\text{F}_3$ the octahedron has a more irregular configuration deviating from an ideal one. This is seen more explicitly from Figure 6.4, where all the bond distances are shown.

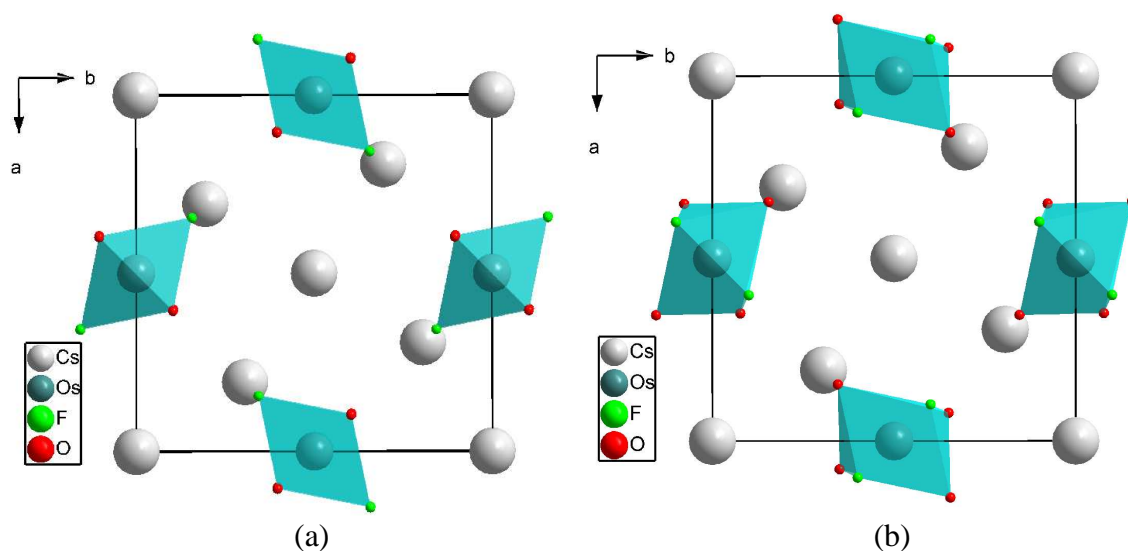


Figure 6.3 The crystal structure shown along c axis: (a) $\text{trans-Cs}_3\text{OsO}_4\text{F}_3$; (b) $\text{cis-Cs}_3\text{OsO}_4\text{F}_3$.

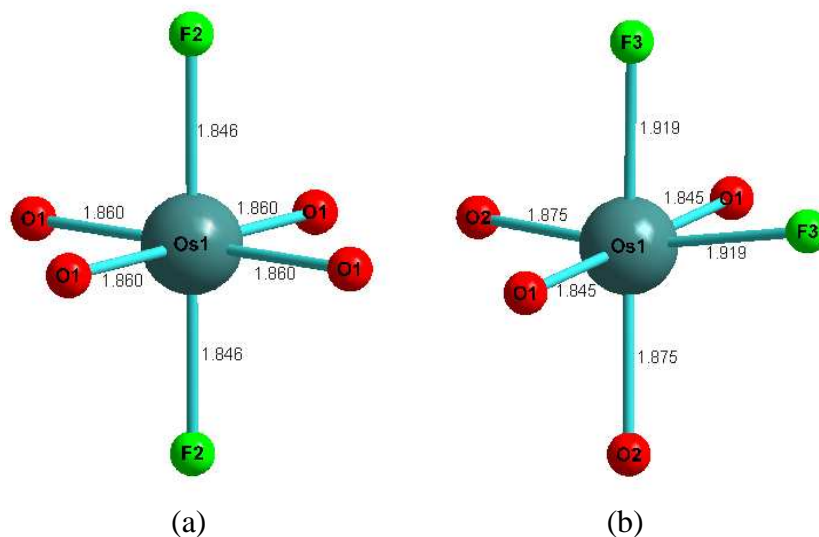


Figure 6.4 Characteristic interatomic distances (\AA) in the $[\text{OsO}_4\text{F}_2]^{2-}$ octahedron for (a) $\text{trans-Cs}_3\text{OsO}_4\text{F}_3$; (b) $\text{cis-Cs}_3\text{OsO}_4\text{F}_3$.

6.2.2.2 Raman spectroscopy

Raman spectroscopy was performed to study the O/F distribution in $\text{Cs}_3\text{OsO}_4\text{F}_3$ (Figure 6.5). The two proposed structures for the $[\text{OsO}_4\text{F}_2]^{2-}$ anion are *cis* (C_{2v}) or *trans* (D_{4h}), which usually can be distinguished by their vibrational spectra. A total of 15 vibrational modes spanning the irreducible representations $6A_1 + 2A_2 + 4B_1 + 3B_2$ under C_{2v} point symmetry are expected for the *cis* isomer with all modes Raman active. 11 vibrational bands belonging to the symmetry groups $2A_{1g} + 2A_{2u} + B_{1g} + B_{2g} + B_{2u} + E_g + 3E_u$ are expected for *trans*- $[\text{OsO}_4\text{F}_2]^{2-}$ with A_{1g} , B_{1g} , B_{2g} and E_g Raman active [133]. This leads to four and two (A_{1g} , B_{2g}) Raman active Os-O stretching bands for *cis*- and *trans*- $[\text{OsO}_4\text{F}_2]^{2-}$, respectively.

In the Raman spectrum shown in Figure 6.5 (in red) four vibrational bands are observed at 884.2, 823.3, ~869 and ~806 cm^{-1} . The last two bands can be recognized as the shoulder of the first two bands. They are assigned to Os-O stretches, indicating a *cis* arrangement, which was also the preference over the *trans* isomer for transition metal oxide fluoride or hydroxide, such as *cis*- $\text{Rb}_2\text{OsO}_4\text{F}_2$ [127] and *cis*- BaOsO_4F_2 [128]. One Os-F stretching band is observed at 407 cm^{-1} in the spectrum. The vibrational bands below 400 cm^{-1} are assigned to bending modes based on LDFT calculations in the reference [133].

As external references, the vibrational bands marked in black and grey in Figure 6.5 are from different CsF samples. The grey one was obtained from a CsF sample exposed in air and has therefore absorbed lots of water. As a consequence the bands at 271 and 968 cm^{-1} are assigned to CsF and H_2O , respectively.

In order to avoid the influence of inhomogeneity, which could be caused by nonuniformly distributed CsF, the Raman spectra of $\text{Cs}_3\text{OsO}_4\text{F}_3$ have been measured at different positions of the sample-containing capillary continuously with a step of 10 μm . Figure 6.6 shows the consistent spectra from several positions, demonstrating that the sample is homogeneous and the small amount of CsF is finely dispersed in $\text{Cs}_3\text{OsO}_4\text{F}_3$.

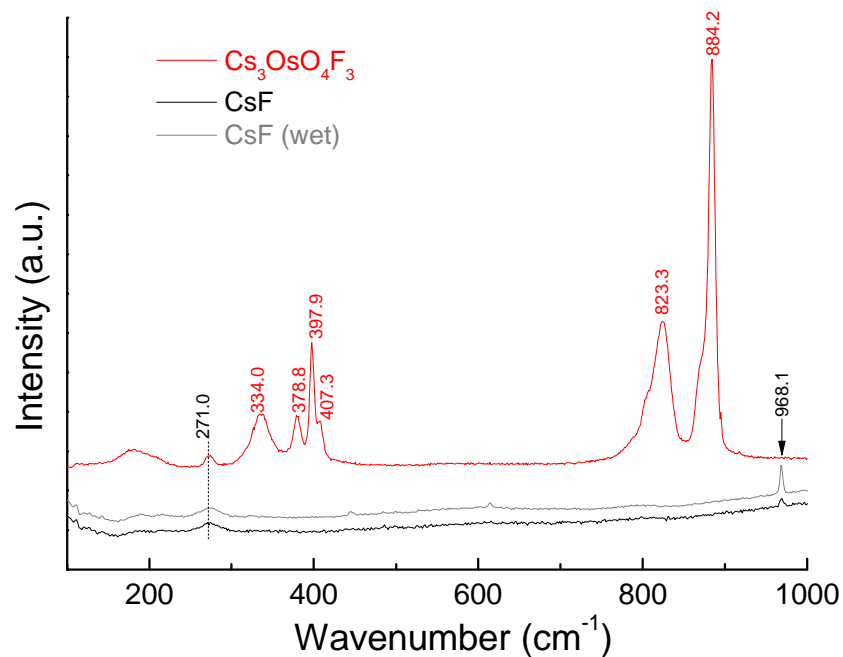


Figure 6.5 Raman spectrum of $\text{Cs}_3\text{OsO}_4\text{F}_3$ and CsF , showing six modes from $\text{Cs}_3\text{OsO}_4\text{F}_3$ represented in red. The numbers in red are assigned to the vibration of $\text{Cs}_3\text{OsO}_4\text{F}_3$ and black for wet CsF .

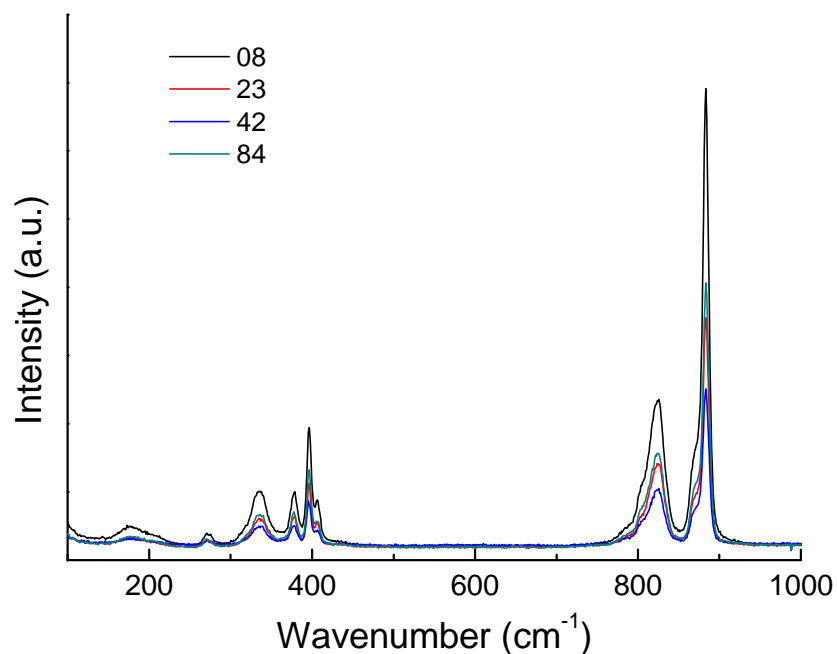


Figure 6.6 Raman spectrum of $\text{Cs}_3\text{OsO}_4\text{F}_3$ measured at different positions of the capillary. Randomly selected numbers represent different positions at the capillary.

6.2.2.3 ^{19}F MAS NMR

Solid-state NMR experiments have been carried out as well to study the O/F ordering in the structure of $\text{Cs}_3\text{OsO}_4\text{F}_3$. ^{19}F MAS spectra of $\text{Cs}_3\text{OsO}_4\text{F}_3$ are shown in Figure 6.7. The spectra of CsF and a mixture of $\text{Cs}_3\text{OsO}_4\text{F}_3$ and CsF are displayed in Figure 6.8.

The ^{19}F MAS spectrum of $\text{Cs}_3\text{OsO}_4\text{F}_3$ consists of a main singlet at 21.7 ppm, which is assigned to F in the $[\text{OsO}_4\text{F}_2]^{2-}$ octahedron. The smaller singlet at 65.4 ppm indicates the F from the $[\text{Cs}_2\text{F}]$ layer. Another weaker singlet appears at -4.3 ppm, possibly indicative of unreacted CsF. In order to prove it, cesium fluoride is characterized by a ^{19}F signal at 96.4 ppm with chemical shifts referenced to calcium fluoride (0 ppm) shown in Figure 6.8. Although this is consistent with the previous publication [134], it does not agree with our result. Weak resonances are also observed, and have been ascribed to surface hydrated species [135].

It is proposed that ^{19}F signals of CsF depend strongly on the chemical environment, resulting on a large shift of the signals [136]. In our experiments, the NMR spectra of CsF and $\text{Cs}_3\text{OsO}_4\text{F}_3$ have been measured individually. There is one main singlet in the spectrum of CsF. Adding up the two individual spectra will give us a sum spectrum shown at the top in Figure 6.8. The NMR spectrum of a mixture of CsF and $\text{Cs}_3\text{OsO}_4\text{F}_3$ in a ratio of 1:1 has also been measured. The $\text{Cs}_3\text{OsO}_4\text{F}_3$ used contains a small amount of CsF as stated in the results from Rietveld refinements, but comparing to the large amount of CsF added in the mixture it is negligible. The obtained spectrum is almost identical to the sum spectrum of individual CsF and $\text{Cs}_3\text{OsO}_4\text{F}_3$. This indicates no interaction between $\text{Cs}_3\text{OsO}_4\text{F}_3$ and the extra CsF. Most likely the reason would be that the two components are only mixed macroscopically and this could not change the local environment of CsF in the matrix of $\text{Cs}_3\text{OsO}_4\text{F}_3$. However, this local environment is an important fact for NMR spectroscopy. As observed from Raman spectra, the extra CsF is dispersed in $\text{Cs}_3\text{OsO}_4\text{F}_3$ after reaction, therefore the local environment of CsF is probably strongly influenced by the $\text{Cs}_3\text{OsO}_4\text{F}_3$ matrix, leading to the shifted signal from 96.4 ppm to -4.3 ppm.

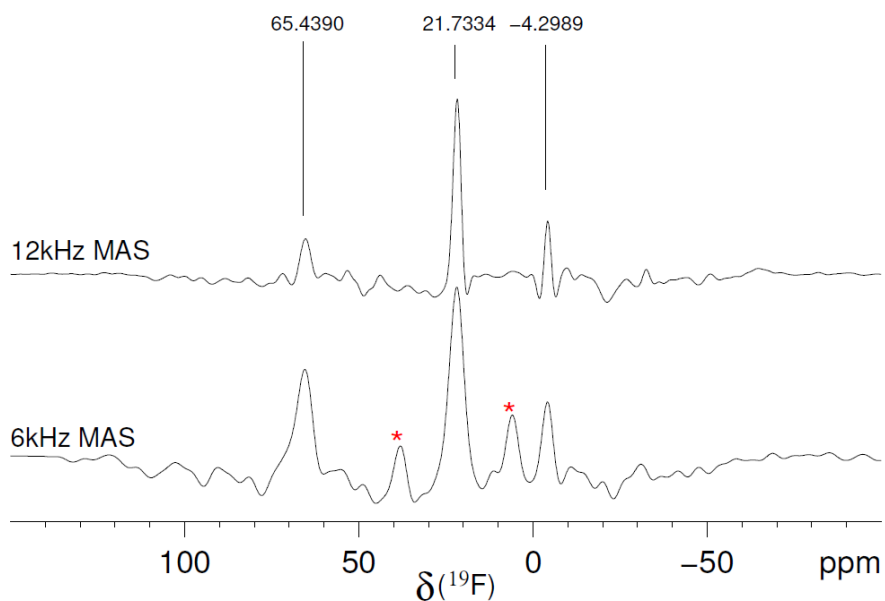


Figure 6.7 ^{19}F MAS NMR spectra of $\text{Cs}_3\text{OsO}_4\text{F}_3$ with chemical shifts referenced to calcium fluoride (0 ppm). *Spinning side bands.

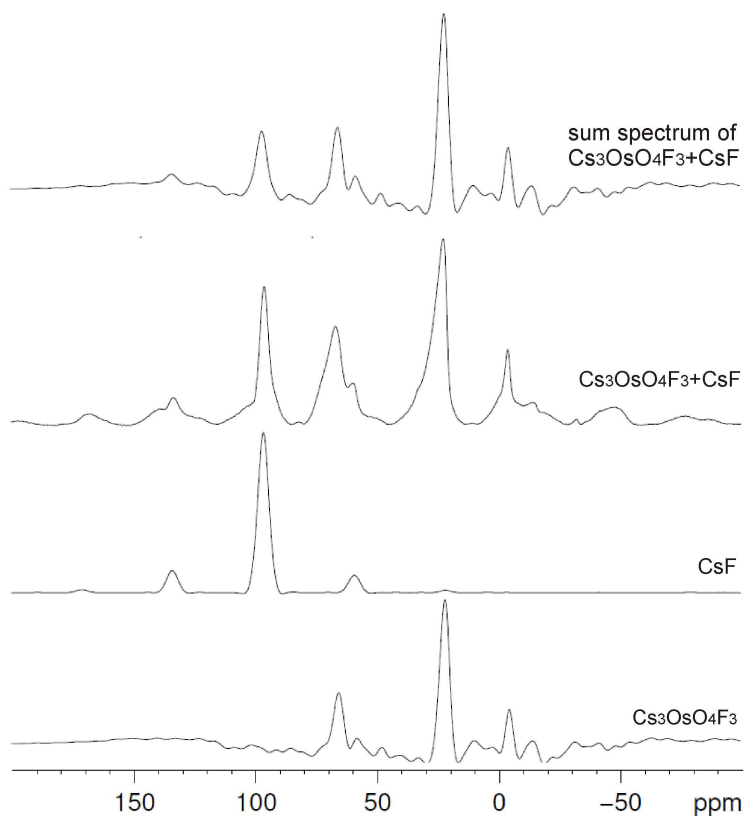


Figure 6.8 ^{19}F NMR spectra (at 14 kHz MAS) of samples with chemical shifts referenced to calcium fluoride (0 ppm), from bottom to top: $\text{Cs}_3\text{OsO}_4\text{F}_3$, CsF, mixture of $\text{Cs}_3\text{OsO}_4\text{F}_3$ and CsF, and sum spectrum of the first two spectra.

6.2.2.4 Discussion

Cations and anions based on osmium oxyfluorides have been investigated by means of XRD, Raman and ^{19}F NMR spectroscopy, extended X-ray absorption fine structure (EXAFS) and electron structure calculations, e.g. OsO_2F_3^+ and $\text{F}(\text{cis-OsO}_2\text{F}_3)^{2+}$ derived from *cis*- OsO_2F_4 [137], OsO_3F^+ and $\mu\text{-F}(\text{OsO}_3\text{F})^{2+}$ derived from *cis*- OsO_3F_2 [138], as well as OsO_4F^- , $\text{OsO}_4\text{F}_2^{2-}$ and OsO_3F_3^- derived from OsO_4 [127, 128, 131, 133, 139]. $\text{Cs}_2[\text{OsO}_4\text{F}_2]$ is the only Cs salt among those oxyfluorides, which is first synthesized from OsO_4 and CsF by Krauss and Wilken in 1925 [139]. On the basis of its vibrational spectra the assignment of a *cis* (C_{2v}) coordination of the $[\text{OsO}_4\text{F}_2]^{2-}$ octahedron is proposed [127, 128]. Os L_{III} edge extended X-ray absorption fine-structure data have been obtained and refined to give $d(\text{Os}=\text{O}) = 1.70 \text{ \AA}$ and $d(\text{Os}-\text{F}) = 2.05 \text{ \AA}$ for $\text{Cs}_2[\text{OsO}_4\text{F}_2]$ [131].

In my work from the reaction of CsF with OsO_4 an oxyfluoride, *cis*- $\text{Cs}_3\text{OsO}_4\text{F}_3$, is formed, which contains $[\text{OsO}_4\text{F}_2]^{2-}$ octahedral units and $[\text{Cs}_2\text{F}]$ layers. The two Os-F distances are 1.923 \AA and the four equatorial Os-O distances are in the range of $1.831\text{--}1.845 \text{ \AA}$, which is in agreement with the previous observations that $d(\text{Os}-\text{F})$ is longer than $d(\text{Os}=\text{O})$ [131]. The NMR spectra show that there are three different F^- ions in the product. Since the two F^- ions in the $[\text{OsO}_4\text{F}_2]^{2-}$ octahedron have the same chemical environment, the spectra do not allow to determine the configuration of the octahedron.

The Raman spectrum of *cis*- $\text{Cs}_3\text{OsO}_4\text{F}_3$ shows consistency with that of $[\text{N}(\text{CH}_3)_4]_2[\text{OsO}_4\text{F}_2]$, which contains the same $[\text{OsO}_4\text{F}_2]^{2-}$ anion [133]. However, it is totally different from earlier reports for $\text{Cs}_2\text{OsO}_4\text{F}_2$ with the same octahedron unit [127, 128]. Later it was claimed by Gerken et al that the $[\text{OsO}_4\text{F}_2]^{2-}$ discussed in the early publications was actually $[\text{OsO}_4\text{F}]^-$ [133].

6.3 CsF+P₄

6.3.1 Sample preparation and characterization

All manipulations were carried out using Schlenk technique or an argon-filled glove box. CsF and P₄ were mixed in a stoichiometric ratio of 3:1, sealed in a Duran glass tube and then heated at temperatures listed in Table 6.6. The mixture of CsF and P₄ turned black after reaching the final target temperature for several hours. The products were washed first with distilled water, then with ethanol (Carl Roth, 99.8%) and finally with CS₂ (Merck, 99.9%). The obtained black powder was characterized by means of powder XRD, EDX and SEM.

Table 6.6 Synthetic conditions and products of the reactions between CsF and P₄.

Reaction temperature (°C)	Time	Product
90	3d	
130	113h	mainly black powder with white phosphorus
150	113h	
170	113h	
200	5d	
240	5d	mainly black powder with
300	3d	red phosphorus

6.3.2 Results

CsF was found to still remain unreacted after reaction from XRD data, but its white color was completely covered by the obtained black amorphous phosphorus. Most of the white phosphorus remained unreacted in the temperature range of 90 - 200 °C, while red phosphorus formed at temperatures above 240 °C.

The reaction at 150 °C is reproducible, and the obtained black powder contains a fine mixture of CsF and white phosphorus. The product was first washed with distilled water to remove CsF, then with ethanol to remove water, and finally with CS₂ to remove the unreacted white phosphorus. The yield of black phosphorus powder is ~10 wt%.

The powder X-ray diffraction pattern of black amorphous phosphorus does not show any sharp reflections, and only the broad maximum at $\sim 30^\circ$ indicates the amorphous structure of the sample (Figure 6.9a). In some cases sharp reflections appeared which could be perfectly indexed to a cubic unit cell for phosphorus (Figure 6.9b). However, it is found that the sharp reflections are contradictory to the rough background and that the 111 reflection at $2\theta \approx 18^\circ$ is too intensive for such cubic cell with an unreasonable Z . After careful inspection by means of SEM and EDX, it is observed that those sharp reflections belong to the byproduct Cs_2SiF_6 with a cubic cell with $a = 8.9111(7) \text{ \AA}$, resulting from the reaction between CsF and the Duran glass tube.

Figure 6.10 shows the SEM images of the product. It can be seen clearly that white Cs_2SiF_6 crystals sitting in the matrix of black amorphous phosphorus. EDX results are shown in Table 6.7. The atomic ratio for Cs_2SiF_6 is perfectly correct, and the atomic% of F is within a reasonable error range.

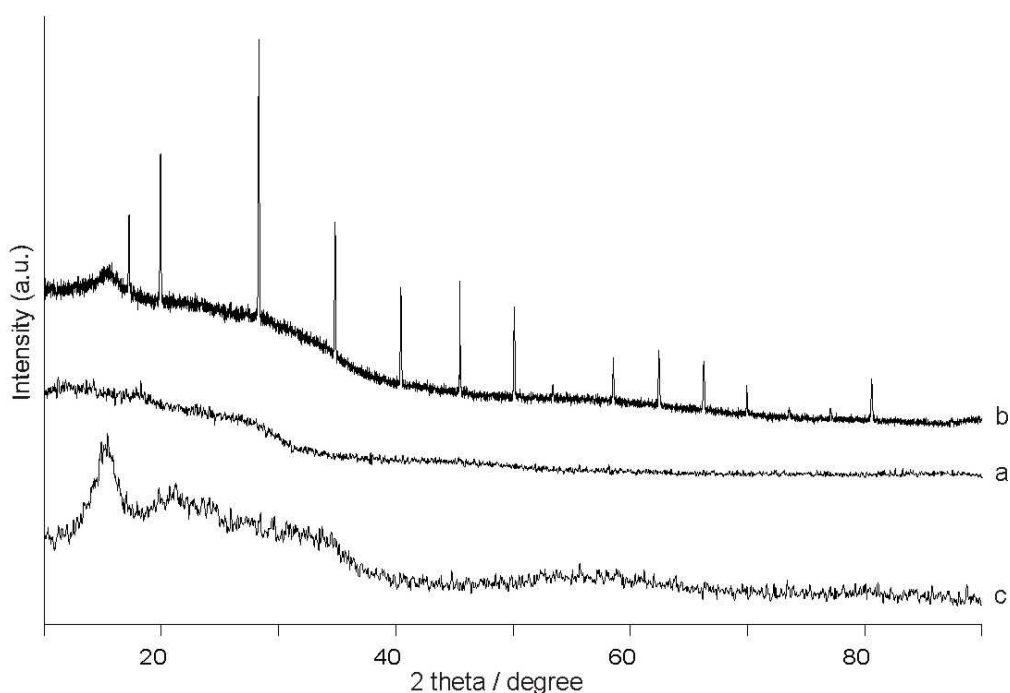


Figure 6.9 XRD patterns of (a) black amorphous phosphorus; (b) amorphous phosphorus containing the byproduct Cs_2SiF_6 ; (c) phosphorus after heating sample (a).

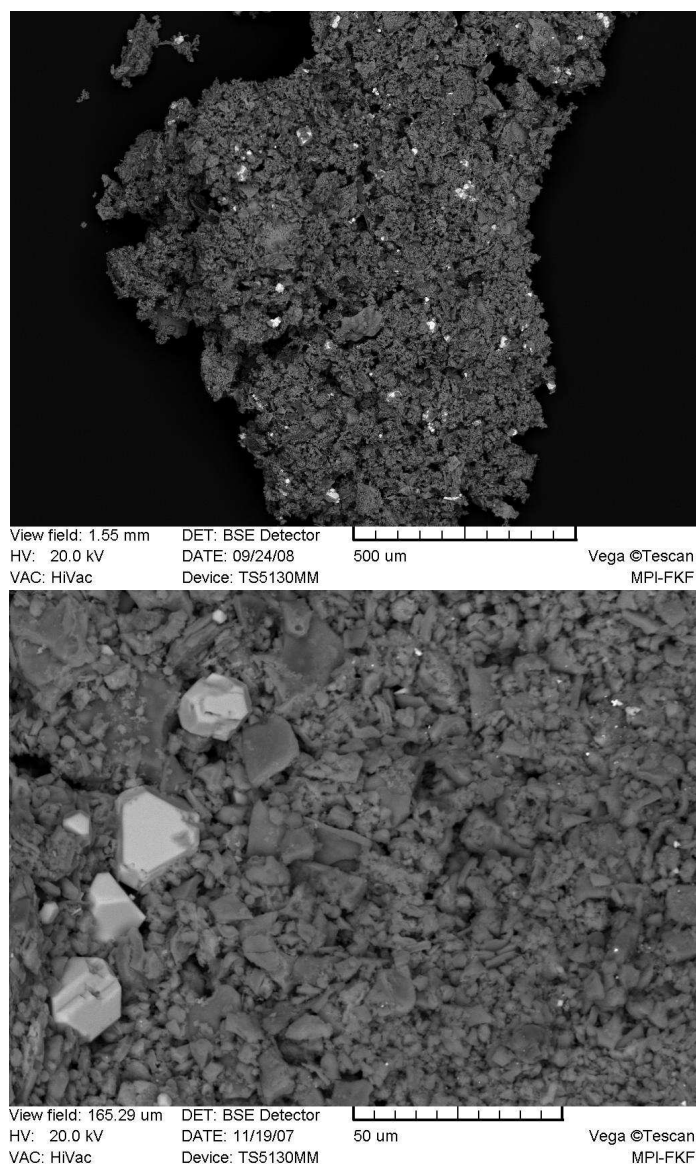


Figure 6.10 SEM images of black amorphous phosphorus with small amounts of Cs_2SiF_6 crystals (white). Top: an overview of a large scale; bottom: focus on Cs_2SiF_6 crystals in the matrix of phosphorus.

Table 6.7 EDX analysis of amorphous phosphorus (top) and Cs_2SiF_6 (bottom) separately.

Element	Intensity	Weight%	Atomic%
P	1.6087	92.00	98.01
Cs	0.7303	8.00	1.99
F	0.9467	35.71	73.75
Si	0.7329	6.60	9.22
Cs	0.8798	57.70	17.03

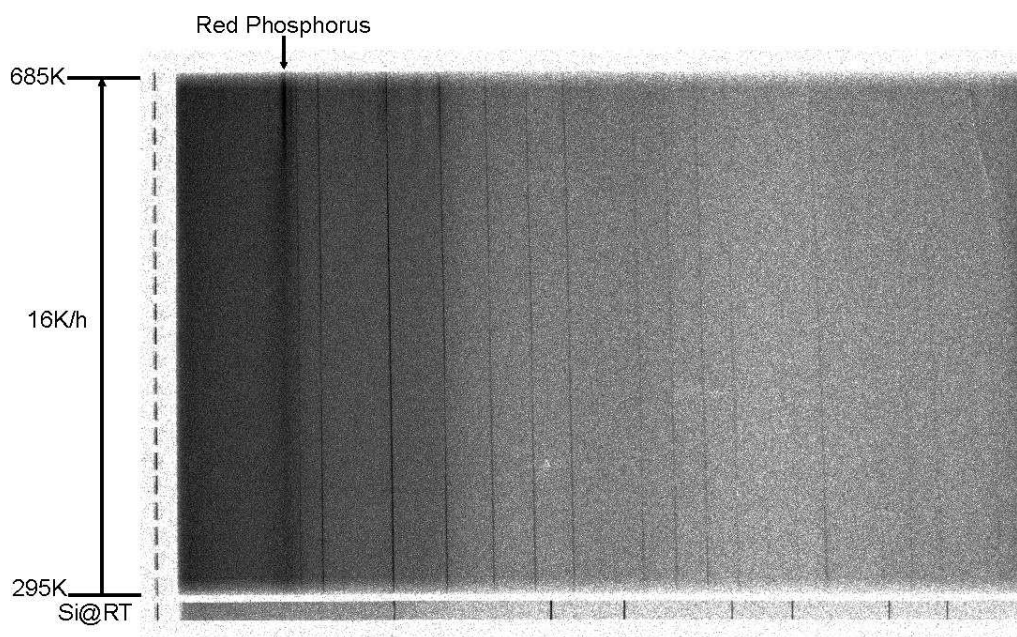


Figure 6.11 High temperature X-ray diffraction patterns of amorphous phosphorus containing Cs_2SiF_6 as internal standard by using a Simon-Guinier camera.

The capillaries filled with the black amorphous phosphorus were heated to a temperature range of 573 - 623 K. Part of the black powder turned into red. The XRD pattern is shown in Figure 6.9c, in which a broad peak around $2\theta = 15.5^\circ$ is typical for red phosphorus. The red phosphorus can also be seen in small amounts in the room-temperature XRD pattern of the black amorphous phosphorus in Figure 6.9b. The *in-situ* XRD measurement with a Simon-Guinier camera from room temperature up to 685 K is shown in Figure 6.11. The red phosphorus becomes dominant at the highest temperature, and the impurity Cs_2SiF_6 as internal standard remains unchanged (sharp lines).

6.3.3 Discussion

From previous study it is observed that Br_2 can be included into CsF lattice and turns it into a layered structure. Comparing to the Br-Br bond, the P-P bonds in the tetrahedral unit are shorter, i.e. 2.1687 - 2.1713 Å in the monoclinic lattice (γ form, $C2/m$) [125] or 2.1756 - 2.1920 Å in the triclinic lattice (β form, $P\bar{1}$) [140, 141], and each P is connected to the other three P atoms. The P_4 tetrahedral unit has a larger spatial occupation than a Br_2 unit. This is one possible reason that the P_4 unit of white phosphorus is not included into the CsF lattice. Instead, in the presence of CsF white phosphorus has transformed into black amorphous phosphorus, which is different from another allotrope, crystalline

black phosphorus and all other known amorphous phosphorus variants. The crystalline black phosphorus crystallizes in an orthorhombic structure consisting of puckered layers parallel to the *ac* plane, in which each layer is shifted by $a/2$ [142-144]. High pressures are usually required to produce black crystalline phosphorus, but it can also be produced at ambient conditions using metal salts as catalysts [145, 146]. More work is required to characterize the differences between these two black forms.

6.4 Conclusion

In summary, we have studied the possibilities of the inclusion of tetrahedral molecules, OsO_4 and P_4 , into the CsF lattice. From the reaction of CsF with OsO_4 an oxyfluoride, $\text{Cs}_3\text{OsO}_4\text{F}_3$, is formed, which contains $[\text{OsO}_4\text{F}_2]^{2-}$ octahedral units and $[\text{Cs}_2\text{F}]$ layers. Raman spectroscopic studies of $\text{Cs}_3\text{OsO}_4\text{F}_3$ demonstrate that the $[\text{OsO}_4\text{F}_2]^{2-}$ octahedron adopts a *cis* configuration, which is consistent with previous reports. The NMR spectra show that there are three different F^- ions in the product, and the main singlet at 21.7 ppm is assigned to F in the $[\text{OsO}_4\text{F}_2]^{2-}$ octahedron.

The reaction between CsF with P_4 leads to a black amorphous phosphorus. P_4 is not included into the CsF lattice. This black amorphous phosphorus transforms into red phosphorus with heating.

Chapter 7

Crystal structure of SiBr₄

7.1 Introduction

SiBr₄ (m.p. 278 K) is the only tetrahedral EX_4 compound ($E = C, Si, Ge, Sn, Pb; X = F, Cl, Br, I$) for which the crystal structure has not yet been reported (see Table 7.1). In 1931 Pohland described two modifications of SiBr₄ [147], which were assigned to the tetragonal ($T < 243$ K) and cubic crystal system ($T > 243$ K) by polarization–microscopy analysis. The structures, configurations and bond distances of a number of EX_4 molecules in the gas phase have been investigated via scattering of fast electrons [148]. Spitzer et al. in 1942 [149] have studied the structure of SiBr₄ by electron diffraction method, which confirmed the tetrahedral bond-angle values. Elastic and rotationally inelastic cross-section calculations by low-energy electron scattering of several tetrahalides have been reported by Varella et al. in 1999 [150]. Earlier packing analyses of EX_4 compounds [151] showed that in all structures the molecules (thus the E atoms) form distinct sphere packings, including hexagonal close packing (h.c.p.), cubic close packing (c.c.p.), body-centered cubic (b.c.c. – W structure) and cubic primitive packing (c.p. – Po structure). Furthermore, a packing(s) similar to the S atoms in pyrite (FeS₂) or the O atoms in solid CO₂ [152, 153] is observed. The X atoms also adopt distorted close-packing arrangements (c.c.p., h.c.p., b.c.c. or c.p.).

The structures of two polymorphs of SiBr₄ have been determined from X-ray and synchrotron powder diffraction data as well as single crystal X-ray diffraction data, and compared to the results obtained from a full crystal-structure prediction of SiBr₄ by lattice-energy minimizations. The transition temperature and the differences between the experimental and calculated structures, as well as the structure types, are described.

Table 7.1 Space groups and number of molecules per unit cell of published experimental crystal structures of molecular EX_4 compounds [132].

EX_4	F	Cl	Br	I
C	$C2/c; P2_1/c$	$Pa\bar{3}$	$C2/c$	$I\bar{4}2m$
Si	$I\bar{4}3m$	$P2_1/c$?	$Pa\bar{3}$
Ge	$I\bar{4}3m$	$P2_1/c$	$P2_1/c; Pa\bar{3}$	$Pa\bar{3}$
Sn	$I4/mmm$ *	$P2_1/c$	$P2_1/c$	$Pa\bar{3}$
Pb	$I4/mmm$ *	$I2/a$	unstable	unstable

* Octahedral coordination.

7.2 Prediction

Crystal structures of $SiBr_4$ were predicted using the program CRYSCA [49] by global minimization of the lattice energy. Presumably $SiBr_4$ are isotopic to $GeBr_4$, therefore crystal structures for $GeBr_4$ were calculated as a test, and the results are compared with the two experimental structures, which have been determined previously [154, 155], in order to obtain reasonable parameters for Br atoms. In an energy range of 5 kJ mol^{-1} ten low-energy crystal structures were found (Table 7.2). From the seven structure types observed experimentally for other EX_4 compounds, two of them were verified experimentally, $P2_1/c$ and $Pa\bar{3}$.

Table 7.2 Low-energy crystal structures of $SiBr_4$ calculated by lattice-energy minimizations [156].

Rank	Energy (kJ mol^{-1})	Space group	Z	Site symmetry of molecule	a (Å)	b (Å)	c (Å)	β (°)
1	-254.228	$C2/c$	4	2	12.314	5.662	11.173	116.86
2	-253.951	$Pbcn$	4	2	5.660	11.149	11.014	
3	-253.440	$Pbca$	8	1	5.667	11.124	22.052	
4	-252.880	$P2_1/c$	4	1	10.217	6.799	10.226	101.45
5	-252.609	$I\bar{4}2m$	2	$\bar{4}2m$	5.659		10.873	
6	-252.548	$P4_2/nmc$	2	$\bar{4}m2$	7.833		5.666	
7	-252.111	$Pmn2_1$	2	m	7.931	6.798	6.464	
8	-251.278	$Pnma$	4	m	13.595	7.941	6.459	
9	-251.268	$Pa\bar{3}$	8	3	11.167			
10	-250.434	$Pbcn$	4	2	5.635	21.899	5.645	

7.3 Experimental section

7.3.1 Characterization

SiBr₄ has been characterized by means of DSC, Simon-Guinier camera, powder synchrotron diffraction and single crystal XRD at temperatures below room temperature (RT). Liquid SiBr₄ was filled at RT in capillaries with different diameters ($\varnothing = 0.1, 0.2$ and 0.3 mm) using Schlenk technique.

A Simon Guinier camera [32] was used for obtaining X-ray powder diffraction data from RT down to 86 K. Two different procedures were used to evaluate the solidification of SiBr₄. In the first one, the capillary is slowly cooled, typically in about 20 hours, and simultaneously the diffraction pattern is recorded. Alternatively, the capillary was quenched in a gas stream set to 86 K within a fraction of a second, and the diffraction pattern was recorded in the process of warming up. In both cases, the whole liquid part in the capillary was completely surrounded by the cooling gas.

In-situ X-ray powder diffraction data of SiBr₄ at low temperature were collected in Debye-Scherrer geometry with a Cryostream 600 cold air blower (Oxford Cryosystems) on a motorized goniometer head at beamline X7B at the National Synchrotron Light Source (NSLS) at Brookhaven National Laboratory. Integration of the full-circle powder patterns was performed using the program FIT2D [157] resulting in diagrams of corrected intensities versus the scattering angle 2θ (Figure 7.3). It was observed that the diffracted intensity distributed over the Debye-Scherrer rings indicated the presence of severe texture.

Two different methods have been used to grow SiBr₄ crystals on a single crystal diffractometer with temperature control devices. The first one is repeated careful freezing and melting. However, it is relatively difficult to grow a single crystal with suitable size due to the rapid crystallization. An alternative way is to freeze one part of the liquid rapidly with a piece of dry ice at a temperature close to the melting point of SiBr₄, and make the other part of the crystals grow out of the liquid slowly with good quality. In both cases, the whole capillary filled with SiBr₄ liquid was located in the cooling gas inside the diffractometer.

Single crystal XRD data were collected at different temperatures using a STOE IPDS I image plate diffractometer with monochromatized AgK α radiation. The starting atomic parameters, derived via direct methods using the program SIR 97 [39], were subsequently refined in the space group $P2_1/c$ or $Pa\bar{3}$ with the program SHELX-97 [40] (full-matrix

least-squares on F^2 with anisotropic atomic displacement parameters for all atoms) within the WinGX program package [41].

7.3.2 DSC

Figure 7.1 shows the result of the DSC measurement. The melting point of SiBr_4 filled in a sealed Al container is $7.0\text{ }^\circ\text{C}$, and the corresponding freezing point is $-26.2\text{ }^\circ\text{C}$ (see below). SiBr_4 single crystals with good quality could be grown at temperature close to the melting point, e.g. $-3\text{ }^\circ\text{C}$ in a slow rate.

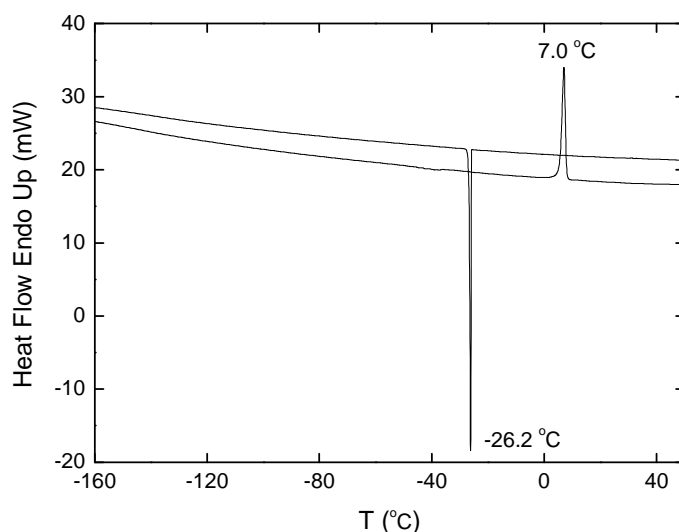


Figure 7.1 The DSC measurement of SiBr_4 in a sealed Al container.

7.3.3 Powder synchrotron diffraction

The 3D representation of the observed scattered X-ray intensities for SiBr_4 as a function of temperature is shown in Figure 7.2. A sharp phase transition from the low temperature (LT) β -phase to the high temperature (HT) α -phase of SiBr_4 could be observed at $T = 168\text{ K}$.

Indexing of the powder diffraction pattern of β - SiBr_4 at $T = 147\text{ K}$ led to a primitive monoclinic unit cell with lattice parameters given in Table 7.3. The space group $P2_1/c$ was taken from the crystal structure of β - GeBr_4 [155], because it was assumed that they were isotypic. The crystal structure of β - SiBr_4 at $T = 147\text{ K}$ was solved with the program TOPAS [38]. The tetrahedral SiBr_4 molecule was constructed with the aid of the rigid body editor of TOPAS using standard bond lengths and angles [159]. For solving the crystal structure of β - SiBr_4 , 6 external degrees of freedom were subjected to global optimization: three translations and three rotations. The average Si-Br bond length of the

β -SiBr₄ molecule was included in the structure determination process as internal degrees of freedom. The structure which gave the best fit to the data in space group $P2_1/c$ was validated by Rietveld refinement. The apparent texture was successfully modeled using symmetrised spherical harmonics of 4th order. One overall isotropic atomic displacement parameter for the SiBr₄ molecule was refined. For β -SiBr₄ at $T = 147$ K, the final Rietveld plot is given in Figure 7.3(a), final agreement factors are listed in Table 7.3, atomic coordinates are given in Table 7.4. The unit cell is shown in Figure 7.4. The average Si-Br bond length was refined to 2.175(3) Å, and each Br-Si-Br angle was fixed at 109.47°.

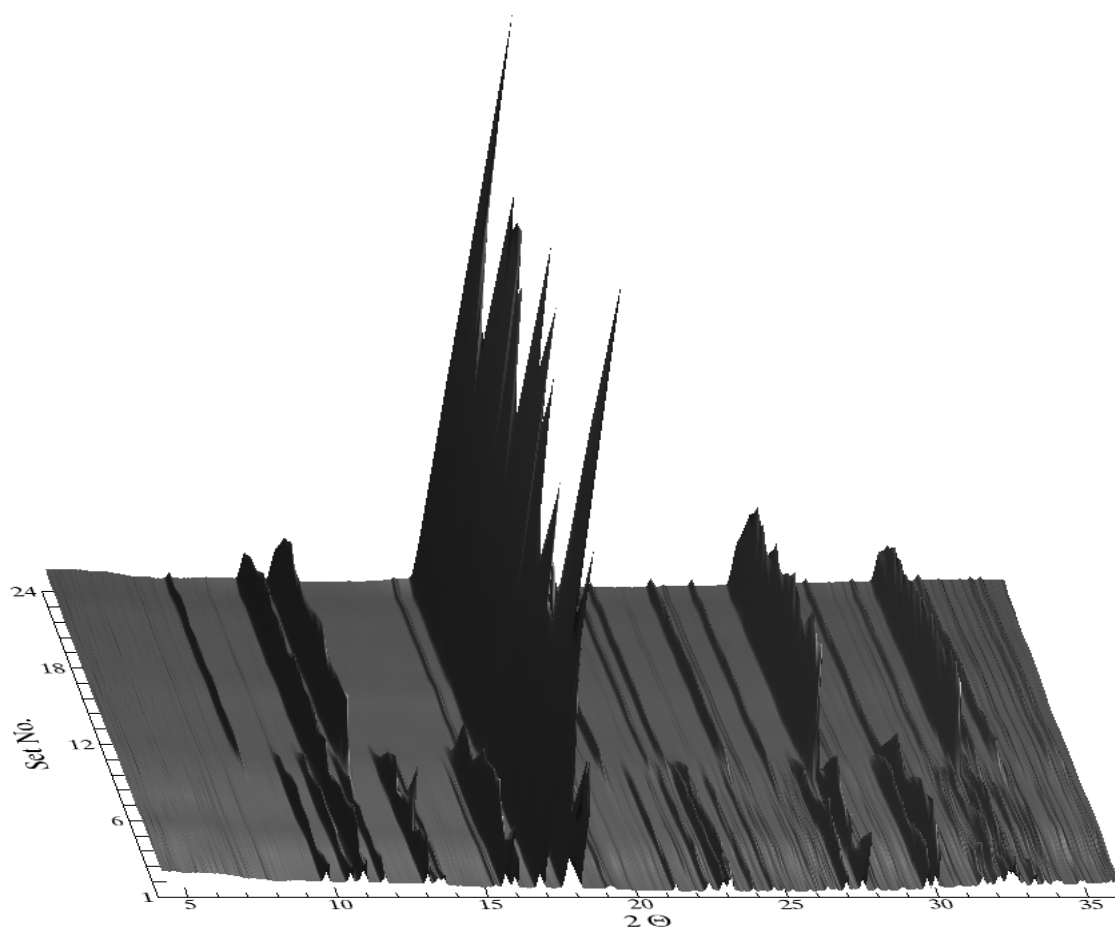


Figure 7.2 Three-dimensional representation of the observed scattered X-ray intensity for SiBr₄ as a function of diffraction angle (x -axis, 4.0-36.0° 2θ) and temperature (y -axis, 120-242 K, 2.25 °C/min, 24 scans, $\lambda = 0.92103$ Å). The phase transition at $T = 168$ K is clearly visible. This figure was prepared with Powder3D [158].

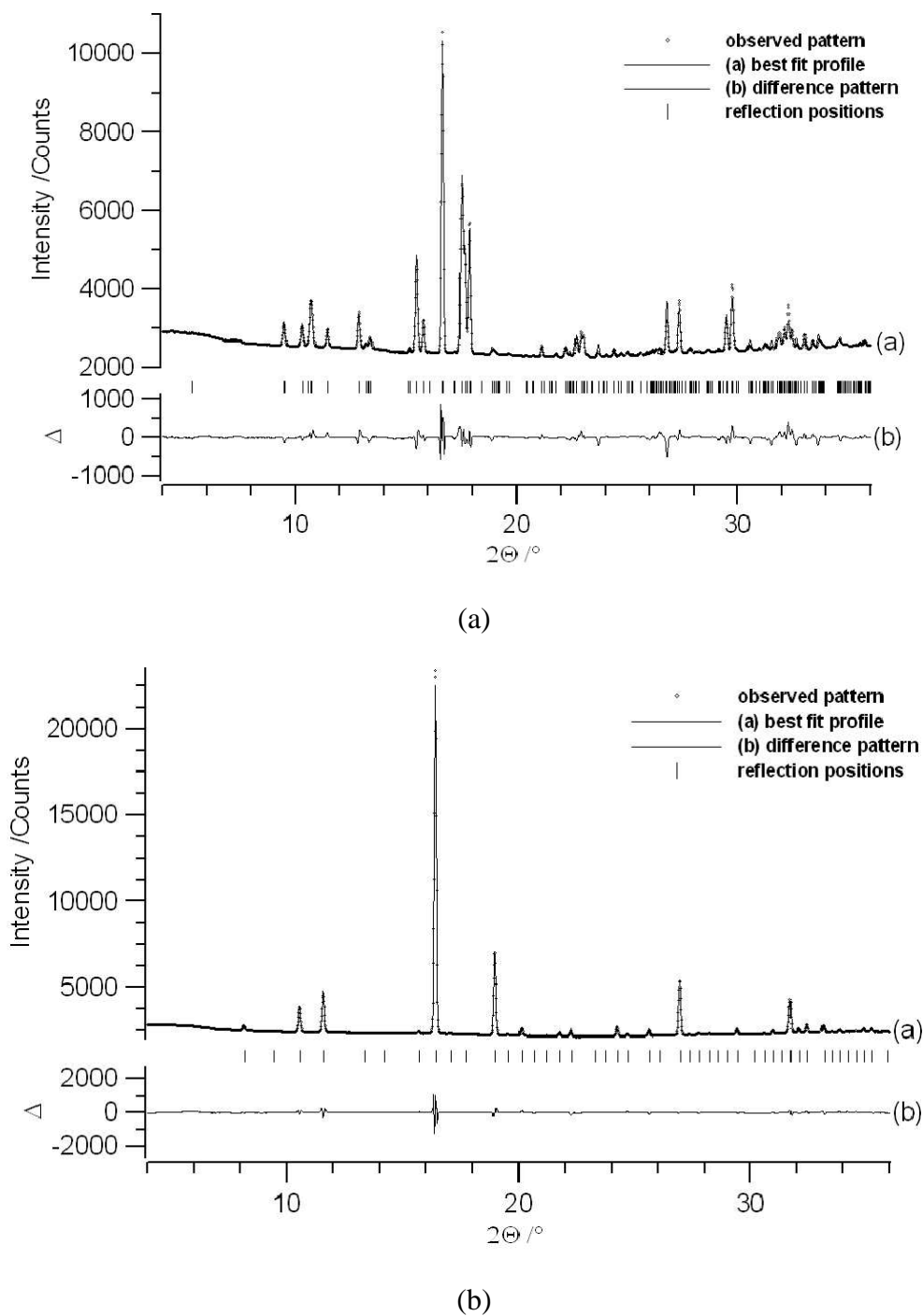


Figure 7.3 Scattered X-ray intensity (a) for β -SiBr₄ at $T = 147$ K and (b) for α -SiBr₄ at $T = 237$ K as a function of diffraction angle 2θ . Shown are the observed pattern (diamonds), the best Rietveld profile fit in $P2_1/c$ for β -SiBr₄ and $Pa\bar{3}$ for α -SiBr₄ (line a), the difference curve between observed and calculated profile (line b), and the reflection markers (vertical bars). $\lambda = 0.92103$ Å.

Starting values for the Rietveld refinement of the HT α -phase of SiBr_4 in the space group $P\bar{a}3$ at $T = 237$ K were taken from the data of $\alpha\text{-GeBr}_4$ [154]. A pronounced texture was also apparent and was successfully modeled using symmetrised spherical harmonics of 8th order. The crystal structure was refined with the program TOPAS[38]. Only one overall isotropic temperature factor for the SiBr_4 molecule was refined. The final agreement factors are listed in Table 7.3, and a typical Rietveld plot is given in Figure 7.3(b). The high degree of rotational disorder is also visible as a strongly increased hump in the background as compared to the LT phase. The unit cell of $\alpha\text{-GeBr}_4$ is shown in Figure 7.4(b). Atomic coordinates are given in Table 7.5, and a selection of intramolecular distances and angles is given in Table 7.6.

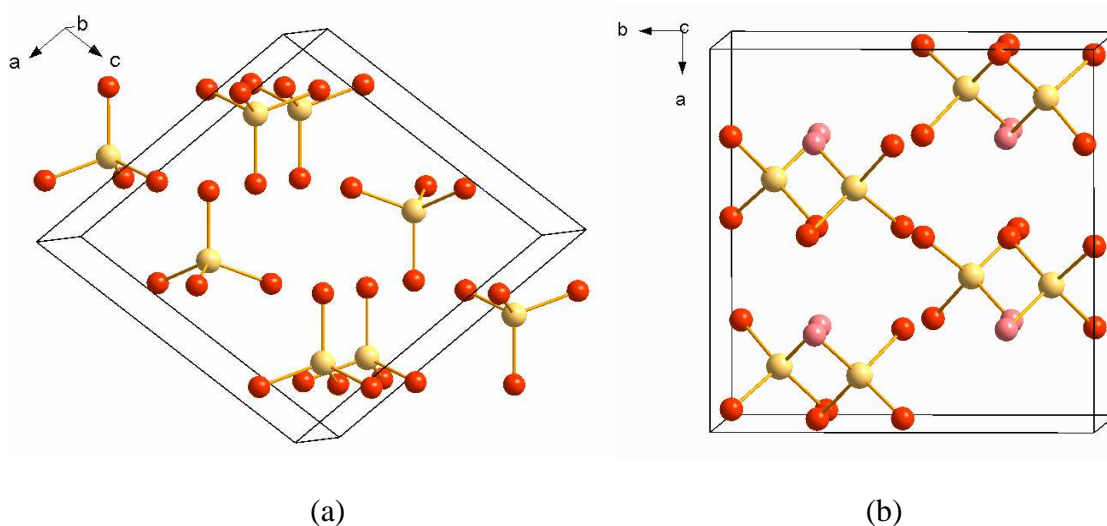


Figure 7.4 Crystal packing of (a) the LT β -phase (space group $P2_1/c$ at $T = 147$ K) and (b) HT α -phase (space group $P\bar{a}3$ at $T = 237$ K) of SiBr_4 . Yellow spheres represent Si^{4+} , red spheres represent all Br^- in (a) and only $\text{Br}(2)$ in (b), and the pink ones in (b) represent $\text{Br}(1)$.

Table 7.3 Crystallographic data for the LT and HT phases of SiBr₄ obtained from Rietveld refinements.

Compound	α -SiBr ₄	β -SiBr ₄
Temperature (K)	237	147
Formula weight (g/mol)	347.69	347.69
Space group	$Pa\bar{3}$ (205)	$P2_1/c$ (14)
Z	8	4
a (Å)	11.1770(1)	10.1319(4)
b (Å)		6.7002(2)
c (Å)		10.2389(3)
β (°)		102.66(0)
V (Å ³)	1396.3	678.2
ρ -calc (g/cm ³)	3.308	3.406
Wavelength (Å)	0.92103	0.92103
R -exp (%) [*]	2.000	1.939
R -p (%) [*]	1.021	1.294
R -wp (%) [*]	1.717	2.293
R -F ² (%) [*]	0.560	2.541
Starting angle (°2 θ)	4	4
Final angle (°2 θ)	36	36
Step width (°2 θ)	0.02	0.02
Time/scan (s)	60	60
No. of variables	25	49

^{*} R -exp, R -p, R -wp, and R -F² as defined in TOPAS (Bruker AXS)

The temperature dependence of the lattice parameters and the volume was analysed by performing Rietveld refinements on 24 datasets starting from $T = 120$ K up to $T = 242$ K (Figure 7.5). Both the lattice parameters and volumes become larger with increasing temperature, and at ~ 170 K two phases coexist.

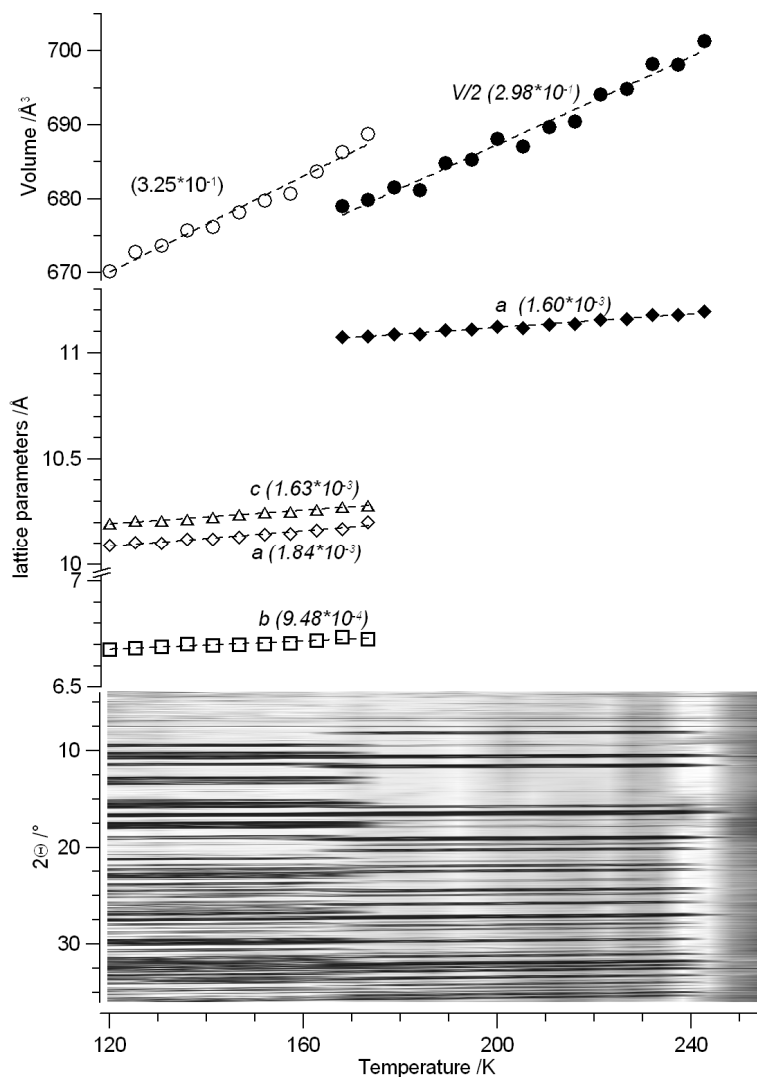


Figure 7.5 Cell volume (top), lattice parameters (middle) and powder diffraction patterns (bottom) of SiBr_4 as a function of temperature in the range from $T = 120$ K up to $T = 242$ K (2.28 K/minute). The phase transition at $T = 168$ K is clearly visible. The value in parentheses is the expansion coefficient of the corresponding parameter in $\text{\AA}/\text{K}$ for a , b and c , and in $\text{\AA}^3/\text{K}$ for volume, which was determined by a linear fit.

Table 7.4 Positional parameters and isotropic temperature factors for β -SiBr₄*.

Atom	x/a	y/b	z/c	$B_{\text{eq}}(\text{\AA}^2)$
Si1	0.246(0)	0.580(1)	0.641(0)	3.17(14)
Br1	0.192	0.886	0.583	3.17(14)
Br2	0.294	0.421	0.472	3.17(14)
Br3	0.076	0.434	0.700	3.17(14)
Br4	0.420	0.578	0.808	3.17(14)

*No esd's are given for some values due to rigid body refinement. Parameter values for rotations about the x , y and z axes of the rigid body are 203.52(92) $^\circ$, 296.35(22) $^\circ$ and 51.25(94) $^\circ$ respectively.

Table 7.5 Positional parameters and isotropic temperature factors for α -SiBr₄.

Atom	x/a	y/b	z/c	$B_{\text{eq}}(\text{\AA}^2)$
Si1	0.131(1)	0.131(1)	0.131(1)	5.22(4)
Br1	0.243(1)	0.243(1)	0.243(1)	5.22(4)
Br2	0.026(0)	0.013(1)	0.248(0)	5.22(4)

Table 7.6 Selected intramolecular distances and angles for α -SiBr₄.

Si1 - Br1	2.155(24) \AA	Br1-Si1-Br2 $\times 3$	108.46(51) $^\circ$
Si1 - Br2 $\times 3$	2.201(9) \AA	Br2-Si1-Br2 $\times 3$	110.47(52) $^\circ$

The two predicted structures are similar to the experimental powder ones, and the results of the comparison are shown in Table 7.7. The LT β -phase corresponds to the predicted structure at rank 4 (Table 7.2). In the experimental as well as the calculated structure, the Br atoms form a distorted h.c.c. with the Si atoms occupying 1/8 of the tetrahedral voids. The molecules themselves, i.e. Si atoms, also form a distorted h.c.c. This structure type is also found for GeBr₄, SnBr₄ and the chlorine compounds (Table 7.1). The volume of the calculated structure of the β -phase is 2.65% larger than that of the experimental one, because the calculations are at ambient conditions and temperature-independent, but in reality the volume decreases with decreasing temperature.

The HT α -phase corresponds to the predicted structure at rank 9 (Table 7.2). The Br atoms form a distorted c.c.p. The tetrahedral voids are occupied such that two molecules are arranged pairwise in a staggered conformation of the Br atoms. The pairs of Si atoms are packed like the O atoms of CO₂ in the solid with a Si...Si distance of 5.072 Å. The α -SiBr₄ is isostructural to GeBr₄ and most of the iodides (Table 7.1).

The coordination number of the molecules increases from 12 in the LT β -phase to 13 in the HT α -phase. The differences in bond lengths and angles between the α - and β -phases are small, thus the molecules do not deviate much from regular tetrahedra as expected. However, the experimental Si-Br bond lengths are significantly shorter than obtained in the calculations, therefore single crystals are needed for a better understanding of the large differences.

Table 7.7 Some characteristics of the experimental powder and calculated crystal structures [156].

	Experimental	Calculated	Difference (%)
α phase: $Pa\bar{3}$, $Z = 8$ ($T = 237$ K)			
a (Å)	11.1770 (1)	11.167	-0.09
V (Å ³)	1396.3 (1)	1392.5	-0.27
Si1—Br1 (Å)	2.155 (24)	2.250	4.4
Si1—Br2 $\times 3$ (Å)	2.201 (9)	2.250	2.2
Br1—Si1—Br2 $\times 3$ (°)	108.46 (51)	108.83	0.34
Br2—Si1—Br2 $\times 3$ (°)	110.47 (52)	110.10	-0.33
β phase: $P2_1/c$, $Z = 4$ ($T = 147$ K)			
a (Å)	10.139 (4)	10.217	0.77
b (Å)	6.7002 (2)	6.799	1.47
c (Å)	10.2389 (3)	10.226	-0.13
β (°)	102.66 (1)	101.45	-1.18
V (Å ³)	678.2 (1)	696.2	2.65
Si—Br (Å)	2.175 (3)	2.250	3.3
Br—Si—Br (°)	109.47†	108.74	-0.67
		108.89	-0.53
		109.31	-0.15
		109.70	0.21
		109.84	0.34
		110.33	0.79

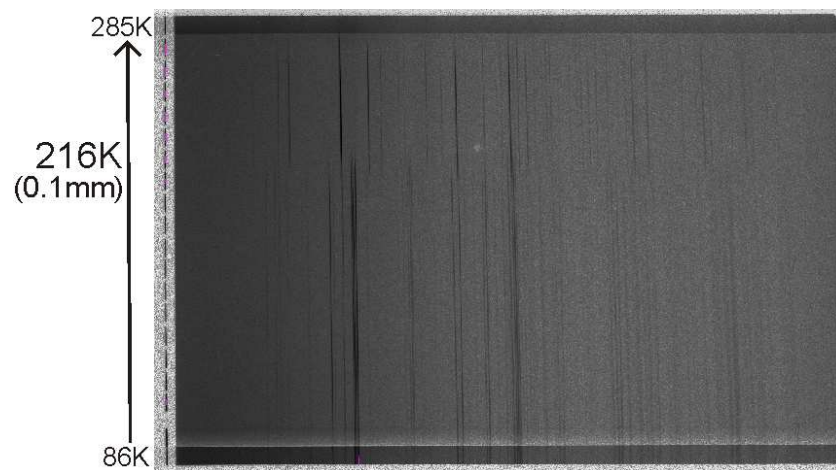
† The Br—Si—Br angle was fixed at 109.47°.

7.3.4 Studies of Transition between α -SiBr₄ and β -SiBr₄

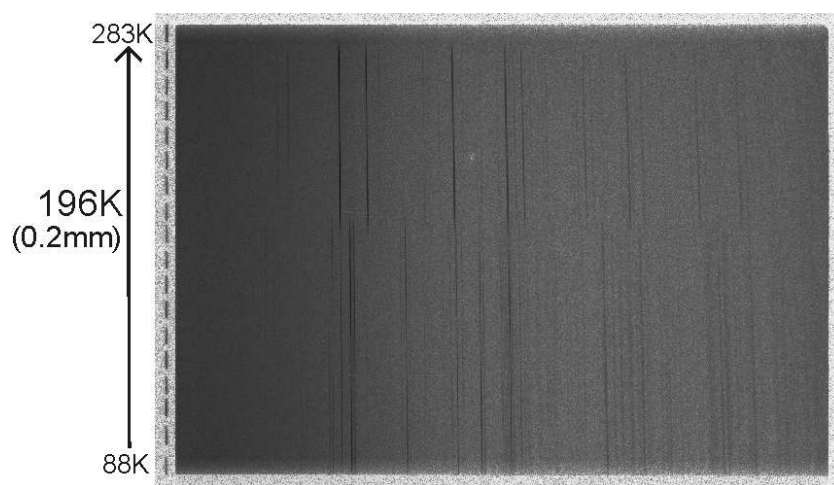
The transition temperature for SiBr₄ showed a surprising large variation with different samples. In order to study the influence of diameter of a capillary on the phase transition, X-ray powder diffraction patterns of SiBr₄ in the temperature range of RT and 86 K have been recorded with a Simon-Guinier camera (Figure 7.6). A capillary of $\varnothing = 0.1$ mm filled with SiBr₄ was quenched and then warmed slowly from 86 K up to 285 K. A transition temperature from the monoclinic to the cubic modification was observed at 216 K, see Figure 7.6(a). In capillaries with larger diameters, the transition temperatures are 196 K and 172 K for the $\varnothing = 0.2$ mm and 0.3 mm, respectively. Obviously, the transition temperature decreases as the diameter of the capillary increases.

Normally a larger diameter is equivalent to a thicker sample, requiring more time to raise the temperature of the entire sample volume because of the limitation of conductive heat transfer [160]. Since in the experiments the capillary was heated continuously, this will result in higher transition temperature with increasing diameter, which is opposite to our experimental finding.

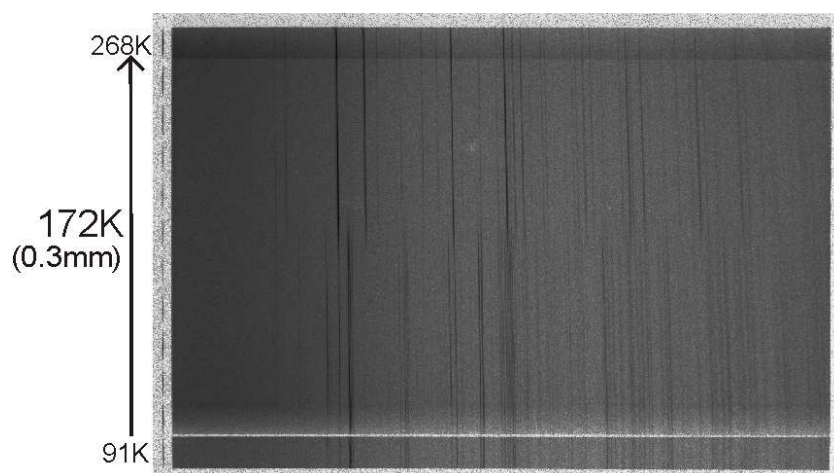
During warming the rearrangement of tetrahedral molecules is accompanied by a temporary volume shrinking according to Figure 7.5. A larger diameter of the capillary allows more “freedom”, i.e. lower energy, for the molecules repacking, thus larger diameter for lower transition temperature. In other words, this diameter dependence of the transition temperature is probably a problem of nucleation.



(a)



(b)



(c)

Figure 7.6 Temperature dependent X-ray powder diffraction patterns of SiBr_4 recorded with Simon-Guinier camera for a capillary of (a) $\varnothing = 0.1$ mm; (b) $\varnothing = 0.2$ mm; (c) $\varnothing = 0.3$ mm.

7.3.5 Single crystal XRD

In order to obtain better data for the crystal structures of α -SiBr₄ and β -SiBr₄ and to understand the differences between the calculated and experimental Si-Br bond distances, the single crystals of α -SiBr₄ and β -SiBr₄ have been grown at 269 K in capillaries with $\varnothing = 0.3$ and 0.2 mm, respectively. As known from the DSC data, the melting point and freezing point of SiBr₄ are 7.0 °C and -26.2 °C, respectively. The single crystals were grown was between these two points. The crystal structures were refined with the program SHELX-97 [40] within the WinGX program package [41]. The results for the refinement for both modifications are shown in Table 7.8. The positional parameters and anisotropic temperature factors are listed in Table 7.9 and Table 7.10, respectively.

The structures of both modifications have been discussed in the previous part of this chapter. Here only differences in the results of the single crystal investigations will be discussed. In the HT α -SiBr₄, each Si atom is surrounded by one Br1 and three Br2 atoms to form a tetrahedron with Si-Br distances of ~ 2.19 Å. The Br-Si-Br angles are close to the angle in an ideal tetrahedron. Each Br atom is cuboctahedrally surrounded by other Br atoms, whereby the three Br-Br distances belonging to a SiBr₄ tetrahedron are 3.573 and 3.578 Å, and the remaining nine Br-Br distances are slightly longer (3.94 to 4.23 Å). The selected intramolecular distances and angles are shown in Table 7.11.

In the structure of the LT β -SiBr₄, each Si atom is surrounded by four crystallographically different Br atoms with Si-Br distances ranging from 2.16 to 2.17 Å and the Br-Si-Br angles lie between 109.18° and 109.80°, therefore the SiBr₄ molecule is close to an ideal tetrahedron as well. Each Br atom is *anti*-cuboctahedrally surrounded by other Br atoms, whereby the three Br-Br distances belonging to a SiBr₄ tetrahedron are in the range from 3.53 to 3.55 Å, and the remaining nine Br-Br distances are slightly longer (3.93 to 4.55 Å). The selected intramolecular distances and angles are shown in Table 7.12.

The α -SiBr₄ and β -SiBr₄ can be grown at a temperature slightly lower than its melting point in capillaries with $\varnothing = 0.3$ and 0.2 mm respectively. According to the powder synchrotron data, β -SiBr₄ is the thermodynamically stable form at lower temperature. However, it has also been observed at the crystallizing temperature (271 K) with a capillary of $\varnothing = 0.2$ mm, which can always be well repeated without exceptions. Furthermore, when the β -SiBr₄ crystal was cooled from 271 K to a temperature below the transition temperature, i.e. 196 K for the capillary with $\varnothing = 0.2$ mm, a phase transition to

the cubic α -SiBr₄ was observed, no matter quenching or slow cooling technique was utilized. This is still an open question. The energy difference between α - and β -SiBr₄ is small, because both phases have close packed molecular structures. Once a nucleus is formed, it starts to grow without transition. Therefore, it is suggested that this is probably due to nucleation problems. What is worth mentioning is the fact that a capillary with smaller diameter ($\varnothing = 0.2$ mm) can be used to grow β -SiBr₄ and one with larger diameter ($\varnothing = 0.3$ mm) to grow α -SiBr₄.

Table 7.8 Data collection and structure refinement for two phases of SiBr₄ single crystals.

Compound	α -SiBr ₄	β -SiBr ₄
Temperature (K)	223	271
Formula weight (g/mol)	347.69	347.69
Crystal system	cubic	monoclinic
Space group	$Pa\bar{3}$ (205)	$P2_1/c$ (14)
Z	8	4
a (Å)	11.1519(13)	10.285(2)
b (Å)		6.7625(13)
c (Å)		10.377(2)
β (°)		103.15(3)
V (Å ³)	1386.90(3)	702.7(2)
ρ -calc (g/cm ³)	3.331	3.287
Wavelength (Å)	AgK α 0.56086	MoK α 0.71073
μ (mm ⁻¹)	23.252	12.270
Reflections collected	4180	5931
Independent reflections	215	1286
parameters refined	17	47
Goodness-of-fit on F^2	1.236	0.898
R_1	0.0460	0.0372
wR_2	0.0837	0.0784
R_1 (all)	0.0564	0.0698
wR_2 (all)	0.0866	0.0844
Largest diff. peak and hole (e/Å ³)	0.989, -0.715	0.545, -0.499

Table 7.9 Positional parameters and anisotropic temperature factors for α -SiBr₄.

Atom	Si1	Br1	Br2
site	8 <i>c</i>	8 <i>c</i>	24 <i>d</i>
<i>x/a</i>	0.1313(2)	0.24484(13)	0.0244(3)
<i>y/b</i>	0.1313(2)	0.24484(13)	0.01225(16)
<i>z/c</i>	0.1313(2)	0.24484(13)	0.24498(10)
<i>U</i> ₁₁	0.010(2)	0.0273(10)	0.0238(12)
<i>U</i> ₂₂	0.010(2)	0.0273(10)	0.0210(10)
<i>U</i> ₃₃	0.010(2)	0.0273(10)	0.0217(10)
<i>U</i> ₁₂	0.0005(13)	-0.0089(5)	-0.0040(9)
<i>U</i> ₁₃	0.0005(13)	-0.0089(5)	0.0071(6)
<i>U</i> ₂₃	0.0005(13)	-0.0089(5)	0.0103(5)

Table 7.10 Positional parameters and anisotropic temperature factors for β -SiBr₄.

Atom	Si1	Br1	Br2	Br3	Br4
site	4 <i>e</i>	4 <i>e</i>	4 <i>e</i>	4 <i>e</i>	4 <i>e</i>
<i>x/a</i>	0.75086(19)	0.69379(10)	0.58636(9)	0.79946(10)	0.92379(8)
<i>y/b</i>	0.4294(3)	0.12645(12)	0.58026(14)	0.57813(15)	0.43467(14)
<i>z/c</i>	0.1443(2)	0.09244(12)	0.20086(11)	-0.02342(10)	0.30921(10)
<i>U</i> ₁₁	0.0426(11)	0.0806(7)	0.0545(6)	0.0868(7)	0.0539(5)
<i>U</i> ₂₂	0.0397(10)	0.0447(4)	0.0812(7)	0.0813(7)	0.0776(6)
<i>U</i> ₃₃	0.0457(13)	0.0841(7)	0.0866(7)	0.0588(6)	0.0640(6)
<i>U</i> ₁₂	-0.0007(8)	-0.0106(4)	0.0134(4)	-0.0148(5)	0.0004(4)
<i>U</i> ₁₃	0.0072(9)	0.0148(5)	0.0159(5)	0.0164(5)	-0.0084(4)
<i>U</i> ₂₃	-0.0002(9)	-0.0103(4)	-0.0190(5)	0.0156(5)	0.0031(5)

Table 7.11 Selected intramolecular distances and angles for α -SiBr₄.

Si1	- Br1	2.193(5) Å	Br1-Si1-Br2 ×3	109.30(13)°
Si1	- Br2 ×3	2.189(4) Å	Br2-Si1-Br2 ×3	109.64(13)°

Table 7.12 Selected intramolecular distances and angles for β -SiBr₄.

Si1 - Br1	2.165(2) Å	Br1-Si1-Br2	109.18(9)°
Si1 - Br2	2.168(2) Å	Br1-Si1-Br3	109.80(10)°
Si1 - Br3	2.165(2) Å	Br1-Si1-Br4	109.80(9)°
Si1 - Br4	2.169(2) Å	Br2-Si1-Br3	109.65(10)°
		Br2-Si1-Br4	109.22(10)°
		Br3-Si1-Br4	109.18(9)°

7.3.6 Discussion

The two predicted structures come close to single crystals experimental data and the results of the calculation are all shown in Table 7.13 with the difference between calculated and single crystals data. The lattice parameters of the powder and single crystal experimental data for the HT α -phase ($P\bar{a}3$, $Z = 8$) are in fair agreement when the temperature is taken into account. They are also very close to the predicted structure for this phase. Because the predicted ones were calculated assuming room temperature, the volume of the calculated structure of the LT β -phase ($P2_1/c$, $Z = 4$) is 2.65% larger than the volume for the experimental powder structure at 147 K. With the single crystal data obtained at a much higher temperature, i.e. $T = 271$ K, the calculation fits better (only - 0.93% difference).

As previously discussed, in both structures derived from the powder diffraction data the differences between the calculated and experimental Si-Br bond lengths are relatively large as compared to the other parameters. For the single crystals, the average differences from the calculation are ~2.6 % and ~3.7 % for the α - and β -phase, respectively, which are slightly better than the powder data. This could result from the van de Waals parameter used for the Br atoms, obtained from a trial calculation for GeBr₄, having too large a value. However, there is only a small difference in the Si-Br bond lengths between experimental powder and single crystal data, and overall in both phases the differences between the calculated and experimental bond lengths are well within the error range of the experiments and calculations.

Table 7.13 Comparison of the experimental and calculated crystal structures.

	Experimental (powder) ^a	Experimental (single crystal)	Calculated	Difference (%) ^b
α -phase ($Pa\bar{3}$)	$T = 237$ K	$T = 223$ K		
a (Å)	11.1770 (1)	11.1519(13)	11.167	0.14
V (Å ³)	1396.3 (1)	1386.90(3)	1392.5	0.40
Si1-Br1 (Å)	2.155 (24)	2.193(5)	2.250	2.53
Si1-Br2 $\times 3$ (Å)	2.201 (9)	2.189(4)	2.250	2.71
Br1-Si1-Br2 $\times 3$ (°)	108.46 (51)	109.30(13)	108.83	-0.43
Br2-Si1-Br2 $\times 3$ (°)	110.47 (52)	109.64(13)	110.10	0.42
β -phase $P2_1/c$	$T = 147$ K	$T = 271$ K		
a (Å)	10.139 (4)	10.285(2)	10.217	-0.66
b (Å)	6.7002 (2)	6.7625(13)	6.799	0.54
c (Å)	10.2389 (3)	10.377(2)	10.226	-1.47
β (°)	102.66 (1)	103.15(3)	101.45	-1.68
V (Å ³)	678.2 (1)	702.7(2)	696.2	-0.93
Si-Br (Å)	2.175 (3)	2.165(2)	2.250	3.78
		2.168(2)	2.250	3.64
		2.169(2)	2.250	3.60
Br-Si-Br (°)	109.47	109.18(9)	108.74	-0.40
		109.18(9)	108.89	-0.27
		109.22(10)	109.31	0.08
		109.65(10)	109.70	0.04
		109.80(9)	109.84	0.04
		109.80(10)	110.33	0.48

^a. The data comes from the literature [161].

^b. The difference is calculated between single crystal experimental and calculated data.

7.4 Conclusion

By global lattice-energy minimizations ten possible crystal structures were predicted for SiBr_4 , and two of them were verified experimentally. The two experimental structures, which have been determined from X-ray and synchrotron powder diffraction data as well as single crystal diffraction data, are very similar to the corresponding predicted ones. Below 167 K SiBr_4 crystallizes in a monoclinic β -phase in $P2_1/c$ ($Z = 4$), and it transforms to a cubic α -phase in $Pa\bar{3}$ ($Z = 8$) above 167 K in a capillary with $\varnothing = 0.3$ mm. The transition temperature is higher when capillaries with smaller diameter are used.

Summary

For technological development and new demands of the growing society there is a constant need for new materials with novel or improved properties. The perovskite-type compounds continue to attract interest, because they can be made with an enormous variety of properties, such as superconductors, semiconductors, dielectrics, ferroelectrics, pyroelectrics, piezoelectrics, catalysts and so on. The general attention for perovskite-type compounds is on the chemistry of the BX_6 octahedra, since in most cases the A ion is an alkali, alkaline earth or a rare earth element, which will not contribute to transport or magnetic properties. As a consequence, ABX_3 perovskites can be said to be a class of transition metal perovskites where A primary acts as a spectator ion. There is a possibility of doping a specific composition at the A , B or X site, leading to further ways to chemically adjust structural and physical properties.

Although the most common perovskite-type compounds are oxides, there are also examples with nitrogen or fluorine. The preparative and structural studies of silver nitrides were first discussed in my thesis. $Ag_{3+x}N$ is found to adopt one variant of the perovskite structure, i.e. the M_4N -type structure ($M = Fe, Mn, Co, Ni, Cu$), with fully or partially filled “ A ” site. Aqueous ammonia was used as the nitriding agent in the method to prepare Ag_4N . Less Ag-rich samples $Ag_{3+x}N$ ($x = 0.2-0.3$) were obtained alternatively via the gaseous ammonia route. The band structures of Ag_3N and Ag_4N calculated using TB-LMTO demonstrate that Ag_3N is an insulator while Ag_4N is metallic. The conduction band of the Ag_4N is formed from highly hybridized Ag_{2-s} , Ag_{1-e_g} and $N-p$ states. The salts of other noble metals, i.e. Pd, Au and Hg with higher electronegativity than Ag and Cu, were reduced in the ammonolysis reactions with NH_3 , and no nitrides but elemental metals were obtained. In the attempts to prepare ternary nitrides, no copper palladium nitride was obtained, whereas Ag and Cu_3N were produced from the ammonolysis reactions of $AgCuF_3$ with diluted NH_3 .

Perovskite compounds with fluorine as the X ion have been discussed in Chapter 4, where $AgCuF_3$ and its isostructural analogue $NaCuF_3$ were found to crystallize in a distorted variant of the $GdFeO_3$ -type structure with $P\bar{1}$ symmetry. In the structures of both compounds, the CuF_3 network of corner-sharing CuF_6 octahedra shows a cooperative Jahn-Teller distortion. Their magnetic properties above 50 K are well

described by the $S = 1/2$ Heisenberg uniform antiferromagnetic chain model assuming only the nearest neighbor interactions with the average antiferromagnetic spin exchange $J/k_B = -300$ and -180 K, respectively. The observation that AgCuF_3 has stronger intrachain antiferromagnetic interactions than NaCuF_3 is consistent with the geometrical parameters associated with their Cu-F-Cu superexchange paths, and is well reproduced by a spin dimer analysis based on EHTB calculations. Powder neutron diffraction data show good agreement with the susceptibility data on the critical temperature T_N indicating long-range magnetic ordering. The Rietveld refinements of the magnetic structure of both compounds are hindered by the low symmetry of the structure and impurities. The high pressure synchrotron data for NaCuF_3 suggests an incomplete and irreversible phase transition at about 130 kbar. A possible monoclinic unit cell is given, and further search for a suitable model is needed in the future to solve the structure of the new phase.

Cs_2AgF_4 crystallizes in the K_2NiF_4 -type structure, behaving as a 2D square-lattice Heisenberg ferromagnet, which is associated with orbital order. Cs_2AgF_4 has been prepared through a solid-state reaction, and its magnetic properties, specific heat and optical properties have been measured. A ferromagnetic transition has been observed at $T_C = 14.5$ K. The magnetic saturation of Cs_2AgF_4 below T_C is very small (~ 50 mT) at $B = 0$, and increases steadily with increasing magnetic field. When $B = 0$, the specific heat C_p of Cs_2AgF_4 exhibits an anomaly at T_C that deviates from a λ -type anomaly. With increasing B , the C_p anomaly becomes weaker without shifting its position and eventually disappears when $B > 200$ Oe. These observations can be understood if the coupling between adjacent AgF_4 layers are weakly antiferromagnetic. When the external magnetic field is increased the interlayer antiferromagnetic exchange might transform into ferromagnetic, causing the disappearance of the C_p anomaly. The measurement of the UV-vis diffuse reflectance reveals Cs_2AgF_4 as an insulator with a band gap of 2.48 eV, in good agreement with the calculated band gap of about 2.5 eV.

We have studied another Ag^{2+} fluoride, a powder sample of $\text{Ag}_2\text{ZnZr}_2\text{F}_{14}$. In its crystal structure Zn has substituted one of the Ag atom positions in $\text{Ag}_3\text{Zr}_2\text{F}_{14}$, leaving pure Ag^{2+} dimers. The high temperature region of the inverse molar magnetic susceptibility data indicates a strong coupling of Ag^{2+} in the Ag_2F_7 dimers, the calculation will be given in the future.

The possibilities of the inclusion of tetrahedral molecules, e.g. OsO_4 and P_4 , into the rock-salt type CsF lattice are discussed in Chapter 6. From the reaction of CsF with OsO_4 an oxyfluoride, $\text{Cs}_3\text{OsO}_4\text{F}_3$, is formed, which contains $[\text{OsO}_4\text{F}_2]^{2-}$ octahedral units and $[\text{Cs}_2\text{F}]$ layers. Raman spectroscopic studies of $\text{Cs}_3\text{OsO}_4\text{F}_3$ demonstrate that the $[\text{OsO}_4\text{F}_2]^{2-}$ octahedron adopts a *cis* configuration, which is consistent with previous reports. The NMR spectra show that there are three different F^- ions in the product, and the main singlet at 21.7 ppm is assigned to F^- in the $[\text{OsO}_4\text{F}_2]^{2-}$ octahedron.

The reaction between CsF with P_4 leads to a black amorphous phosphorus. P_4 is not included into the CsF lattice. This black amorphous phosphorus transforms into red phosphorus with heating.

In the last chapter, structural studies have been performed on SiBr_4 (m.p. 278 K). By global lattice-energy minimizations ten possible crystal structures were predicted for SiBr_4 , and two of them were verified experimentally from X-ray and synchrotron powder diffraction data as well as single crystal diffraction data. The two experimental structures are very similar to the corresponding predicted ones. Below 167 K SiBr_4 crystallizes in a monoclinic β -phase in $P2_1/c$ ($Z = 4$), and it transforms to a cubic α -phase in $P\bar{a}3$ ($Z = 8$) above 167 K in a capillary with $\varnothing = 0.3$ mm. The transition temperature is higher when capillaries with smaller diameter are used.

List of Tables

3.1	The synthetic conditions and products from ammonolysis reactions of silver fluorides via the gaseous ammonia route.	16
3.2	Comparison of the cell parameters of different batches of silver nitride for a general molecular formula of Ag_{3+x}N .	19
3.3	The synthetic conditions and products from the ammonolysis reactions for Cu_3N .	21
3.4	Atomic coordinates for Ag_4N .	24
3.5	Cell parameters and interatomic distances (\AA) for Ag_4N and $\text{Ag}_{3.3}\text{N}$, with f.c.c. Ag for comparison.	24
3.6	The syntheses of palladium nitride from the ammonolysis reactions.	25
3.7	The synthetic conditions and products from the ammonolysis reactions for gold nitride.	26
3.8	The synthetic conditions and products from the ammonolysis reactions for mercury nitride.	26
3.9	The synthetic conditions and products from the ammonolysis reactions of AgCuF_3 .	27
3.10	The synthetic conditions and products from the ammonolysis reactions for copper palladium nitride.	28
4.1	Data collection and structure refinement parameters for AgCuF_3 .	35
4.2	Positional parameters and isotropic displacement factors for AgCuF_3 .	36
4.3	Selected interatomic distances (\AA) in the structure of AgCuF_3 .	36
4.4	Lattice parameters of AgCuF_3 and NaCuF_3 .	37
4.5	Geometrical parameters and singlet-triplet splitting energy $(\Delta\varepsilon)^2$ values associated with the spin exchange paths in AgCuF_3 and NaCuF_3^a .	39
5.1	Crystallographic data of Cs_2AgF_4 .	60
5.2	Selected bond distances of Cs_2AgF_4 .	60
5.3	Crystallographic data of $\text{Ag}_2\text{ZnZr}_2\text{F}_{14}$.	70
5.4	Positional parameters and isotropic atomic displacement parameters for $\text{Ag}_2\text{ZnZr}_2\text{F}_{14}$.	72

6.1	Data collection and structure refinement for the two possible structures of $\text{Cs}_3\text{OsO}_4\text{F}_3$.	78
6.2	Positional parameters and isotropic temperature factors for <i>trans</i> - $\text{Cs}_3\text{OsO}_4\text{F}_3$.	80
6.3	Positional parameters and isotropic temperature factors for <i>cis</i> - $\text{Cs}_3\text{OsO}_4\text{F}_3$.	80
6.4	Selected intramolecular distances (Å) and angles (°) for <i>trans</i> - $\text{Cs}_3\text{OsO}_4\text{F}_3$.	81
6.5	Selected intramolecular distances (Å) and angles (°) for <i>cis</i> - $\text{Cs}_3\text{OsO}_4\text{F}_3$.	81
6.6	Synthetic conditions and products of the reactions between CsF and P_4 .	88
6.7	EDX analysis of amorphous phosphorus (top) and Cs_2SiF_6 (bottom) separately.	90
7.1	Space groups and number of molecules per unit cell of published experimental crystal structures of molecular EX_4 compounds [132].	94
7.2	Low-energy crystal structures of SiBr_4 calculated by lattice-energy minimizations [156].	94
7.3	Crystallographic data for the LT and HT phases of SiBr_4 obtained from Rietveld refinements.	100
7.4	Positional parameters and isotropic temperature factors for β - SiBr_4 .	102
7.5	Positional parameters and isotropic temperature factors for α - SiBr_4 .	102
7.6	Selected intramolecular distances and angles for α - SiBr_4 .	102
7.7	Some characteristics of the experimental powder and calculated crystal structures [156].	103
7.8	Data collection and structure refinement for two phases of SiBr_4 single crystals.	107
7.9	Positional parameters and anisotropic temperature factors for α - SiBr_4 .	108
7.10	Positional parameters and anisotropic temperature factors for β - SiBr_4 .	108
7.11	Selected intramolecular distances and angles for α - SiBr_4 .	108
7.12	Selected intramolecular distances and angles for β - SiBr_4 .	109
7.13	Comparison of the experimental and calculated crystal structures.	110

List of Figures

2.1	Simon-Guinier camera.	6
2.2	Experimental setup of D20 at the ILL [33].	7
2.3	The DTA setup.	10
3.1	Silver nitride under water.	17
3.2	Experimental XRD patterns of the silver nitride 1 (aqueous ammonia route) and 2 (gaseous ammonia route). The vertical dashed lines correspond to the theoretical position of diffraction peaks of the silver nitride with $a = 4.29 \text{ \AA}$ (by Powdercell 2.4 [31]).	17
3.3	Observed and calculated X-ray diffraction patterns of the silver nitride. (a) From top to bottom: sample 1 (observed), Ag_4N and Ag_3N (the latter two calculated with $a = 4.35 \text{ \AA}$); (b) from top to bottom: sample 2 (observed), $\text{Ag}_{3.3}\text{N}$ (calculated with $a = 4.29 \text{ \AA}$). Powdercell was used for the calculation, with Ag2 occupation factor of 0, 0.3 and 1, respectively. The vertical dashed lines correspond to the theoretical position of diffraction peaks of the silver nitride.	18
3.4	Comparison of the observed X-ray diffraction data for the same batch of silver nitride 2 at different time after preparation. The vertical dashed lines correspond to the theoretical position of diffraction peaks of the silver nitride.	19
3.5	Electronic band structures of Ag_3N and Ag_4N . Horizontal line is the Fermi level.	20
3.6	Comparison of the contribution of different orbitals to the conduction band of Ag_4N . Ag2 is the Ag (0) at the center of the unit cell. Horizontal line is the Fermi level.	21
3.7	Unit cell of Ag_4N used for indexing. (a) The structure with the atomic positions following Figure 3.7 with the formula of $(\text{Ag}_2)\text{N}(\text{Ag}_1)_3$. (b) Shifting half of the unit cell along one of the cell axes, an f.c.c. cell for the Ag atoms is obtained.	23

3.8	Comparison of the atomic arrangements in Ag_3N and Ag_4N : (a) open-framework Ag_3N with partially close packed silver; (b) Ag_4N described by a cubic sequence ABC of close packed silver atom layers with analogous octahedra. Small blue spheres represent N atoms, and big spheres with all other colors represent Ag in different layers.	23
3.9	The XRD pattern of the products of the ammonolysis reaction of AgCuF_3 with diluted NH_3 at 250 °C. The Bragg reflections marked with “.” indicate Cu_3N , “*”Ag. Remaining reflections are from unreacted AgCuF_3 .	28
3.10	The SEM images of CuPd for rank 7 in Table 3.1 (a) with Secondary Electron (SE) detector; (b) Backscatter Electron (BSE) detector.	30
4.1	(a) Representative CuF_6 octahedron in AgCuF_3 with two short (<i>s</i>), two medium (<i>m</i>) and two long (<i>l</i>) Cu-F bonds; (b) Parallel corner-sharing CuF_6 octahedra chains. The upper chain constructed from Cu1 (turquoise) and Cu2 (green), the lower one from Cu3 (orange) and Cu4 (pink). For the color code of the bonds, see (a).	37
4.2	Unit cell of AgCuF_3 . Ag atoms are drawn in gray. For the coloring of the other atoms, see Figure 4.1.	38
4.3	DSC curve for AgCuF_3 .	40
4.4	DTA curve for NaCuF_3 .	40
4.5	Temperature-dependence of the magnetic susceptibility of AgCuF_3 in the range of 2 - 300 K. The experimental values are presented by circles, and the solid blue line is fitted. The inset shows the molar magnetic susceptibility at low temperatures.	41
4.6	Temperature dependence of the magnetic susceptibility of NaCuF_3 in the range of 2 - 300 K. The experimental values are presented by circles, and the solid blue line is the fitting curve in terms of a $S = 1/2$ Heisenberg chain with antiferromagnetic nearest-neighbor interaction. The inset shows the molar magnetic susceptibility determined with an external field of 0.1 T at low temperatures.	41
4.7	3D representation of the temperature dependence of the EPR signal for AgCuF_3 with temperature decreasing in a range of 100 - 20 K.	43

- 4.8 2D representations of the temperature dependence of the EPR signal for AgCuF_3 with temperature decreasing in a range of (a) 150 – 30 K, (b) 28 – 20 K. 44
- 4.9 The inset shows a typical EPR signal for AgCuF_3 (black circles) with the differential of a Lorentzian fit (red line) given. The temperature dependence of the signals line width (black circles) is shown for AgCuF_3 in the top main panel. The two lower panels show the intensity of the EPR signal with renormalized fit from the molar magnetic susceptibility (middle) and the temperature dependence of the g factor (bottom) for AgCuF_3 . 45
- 4.10 3D representation of the temperature dependence of the EPR signal for NaCuF_3 with temperature decreasing in a range of 100 – 20 K. 47
- 4.11 2D representations of the temperature dependence of the EPR signal for NaCuF_3 with temperature (a) decreasing between 100 – 25 K and (b) increasing between 22 – 97 K. 47
- 4.12 The inset shows a typical EPR signal for NaCuF_3 (black circles) with the differential of a Lorentzian fit (red line), the deconvoluted signals are shown by respective lines in black, turquoise and purple. In the main panels, red dots represent NaCuF_3 , while the black and turquoise dots are the paramagnetic impurities. The temperature dependence of line width (black circles) is shown for NaCuF_3 in the top main panel. The middle panel shows the intensity with error bars of the EPR signal and the renormalized fit from the molar susceptibility (red solid line). Shown in the bottom panel is the temperature dependence of the g factor, with the dotted line showing expected g factor of Cu^{2+} of 2.13. 48
- 4.13 The plot of C_p/T vs. T^2 for AgCuF_3 with a sharp anomaly at 21.1 K and the fit according to Eq.3.2-3.4 (red line) with the inset shows the temperature dependence of the specific heat. 50
- 4.14 The plot of C_p/T vs. T^2 for NaCuF_3 with a sharp anomaly at 18.6 K and the fit according to Eq. 4.2-3.4 (red line) with the inset showing the temperature dependence of the specific heat. 50
- 4.15 The 3D temperature dependence of the powder neutron diffraction patterns of (a) AgCuF_3 and (b) NaCuF_3 . 52

- 4.16 The temperature dependence of the integrated intensity of the magnetic reflection observed for (a): AgCuF_3 at $2\theta = 18.2^\circ$ and (b): NaCuF_3 at $2\theta = 17.8^\circ$ ($\lambda = 2.4 \text{ \AA}$). The solid line is a fit of the experimental data with a power law with a critical temperature of $T_N(\text{AgCuF}_3) = 21.3(5) \text{ K}$ and $T_N(\text{NaCuF}_3) = 18.5(3) \text{ K}$. 53
- 4.17 Powder neutron diffraction pattern of AgCuF_3 : The green line in the bottom is the difference between diffraction data of 2 K (red) and 30 K (blue), showing the magnetic reflections. 53
- 4.18 The 2D graph of the temperature dependence of powder neutron diffraction for NaCuF_3 . 54
- 4.19 Powder neutron diffraction patterns taken at $T = 2 \text{ K}$ and 30 K as well as their difference (2 K - 30 K) for NaCuF_3 . 54
- 4.20 The high pressure synchrotron data for NaCuF_3 powder, obtained at ID09A beamline of ESRF, Grenoble. From bottom to top, the pressure increase first from 5.5 kbar to 302.4 kbar, then drop to lower pressure again. 55
- 5.1 Rietveld refinement of Cs_2AgF_4 XRD data. The black dots represent the calculated pattern, red line represents the observed pattern, gray line shows the difference pattern and vertical bars indicate reflection positions. 59
- 5.2 Crystal structure of Cs_2AgF_4 . 59
- 5.3 Temperature dependence of the inverse molar magnetic susceptibility of Cs_2AgF_4 in a magnetic field of 100 Oe. The red line is the fitted curve from Curie-Weiss law; inset shows the temperature dependence of molar magnetization. 61
- 5.4 The hysteresis curve at $T = 5 \text{ K}$ (open circles) for Cs_2AgF_4 ; the inset shows the curve in fields between -500 and 500 Oe in detail, the line is a guide for the eye. 62
- 5.5 Temperature dependence of the magnetization at different magnetic fields, lines are a guide for the eye only. 62
- 5.6 Temperature dependence of the specific heat in different fields in a range from 0 to 3000 Oe, 0 Oe (1) and 0 Oe (2) are the zero field at the beginning and end of the variation of the external field, respectively. The lines are a guide for the eye only. Inset: the specific heat with an anomaly at $T_C = 14.2 \text{ K}$ at zero field. 64

5.7	The temperature dependence of the specific heat, showing an approximate linear relationship between C_p/T vs. T^2 below T_C .	64
5.8	Temperature dependence of EPR signal for Cs_2AgF_4 .	65
5.9	The temperature dependence of the line widths for the EPR signals is shown for Cs_2AgF_4 in the top main panel. The inset shows a typical EPR signal (black circles) with a Lorentzian fit (red line). The two lower panels show the temperature dependence of the g factor (middle) and the intensity of the EPR signal (bottom panel) for Cs_2AgF_4 .	66
5.10	UV-Vis diffuse reflectance of two Cs_2AgF_4 samples: in Ar (black) and shortly exposed in air (gray).	67
5.11	The $(ah\nu)^2$ versus $h\nu$ curve of Cs_2AgF_4 .	69
5.12	Rietveld refinement of XRD data for $\text{Ag}_2\text{ZnZr}_2\text{F}_{14}$. The black dots represent the calculated pattern, red line represents the observed pattern, gray line shows the difference pattern and blue vertical bars indicate reflection positions.	69
5.13	Crystal structure of $\text{Ag}_2\text{ZnZr}_2\text{F}_{14}$.	71
5.14	Temperature dependence of the inverse molar susceptibility of $\text{Ag}_2\text{ZnZr}_2\text{F}_{14}$ at a magnetic field of 1 T; inset shows the temperature dependence of molar magnetization.	72
6.1	Powder X-ray diffraction patterns for (a) <i>trans</i> - $\text{Cs}_3\text{OsO}_4\text{F}_3$ and (b) <i>cis</i> - $\text{Cs}_3\text{OsO}_4\text{F}_3$. Shown are the observed pattern (black diamonds), the best Rietveld fits profile in $P4/mbm$ for <i>trans</i> - $\text{Cs}_3\text{OsO}_4\text{F}_3$ and $P4$ for <i>cis</i> - $\text{Cs}_3\text{OsO}_4\text{F}_3$ (red lines), the difference curve between observed and calculated profile (grey line), and the reflection markers (vertical bars). The wavelength is $\lambda = 0.7093 \text{ \AA}$ ($\text{MoK}\alpha$).	77
6.2	Crystal structure of the two possible structures of $\text{Cs}_3\text{OsO}_4\text{F}_3$. the turquoise octahedra are (a) <i>trans</i> - $[\text{OsO}_4\text{F}_2]^{2-}$ units and (b) <i>cis</i> - $[\text{OsO}_4\text{F}_2]^{2-}$, respectively. In both structures, $[\text{Cs}_2\text{F}]$ layers are parallel to the ab plane at $c/2$.	79
6.3	The crystal structure shown along c axis: (a) <i>trans</i> - $\text{Cs}_3\text{OsO}_4\text{F}_3$; (b) <i>cis</i> - $\text{Cs}_3\text{OsO}_4\text{F}_3$.	82
6.4	Characteristic interatomic distances (\AA) in the $[\text{OsO}_4\text{F}_2]^{2-}$ octahedron for (a) <i>trans</i> - $\text{Cs}_3\text{OsO}_4\text{F}_3$; (b) <i>cis</i> - $\text{Cs}_3\text{OsO}_4\text{F}_3$.	82

- 6.5 Raman spectrum of $\text{Cs}_3\text{OsO}_4\text{F}_3$ and CsF , showing six modes from $\text{Cs}_3\text{OsO}_4\text{F}_3$ represented in red. The numbers in red are assigned to the vibration of $\text{Cs}_3\text{OsO}_4\text{F}_3$ and black for wet CsF . 84
- 6.6 Raman spectrum of $\text{Cs}_3\text{OsO}_4\text{F}_3$ measured at different positions of the capillary. Randomly selected numbers represent different positions at the capillary. 84
- 6.7 ^{19}F MAS NMR spectra of $\text{Cs}_3\text{OsO}_4\text{F}_3$ with chemical shifts referenced to calcium fluoride (0 ppm). *Spinning side bands. 86
- 6.8 ^{19}F NMR spectra (at 14 kHz MAS) of samples with chemical shifts referenced to calcium fluoride (0 ppm), from bottom to top: $\text{Cs}_3\text{OsO}_4\text{F}_3$, CsF , mixture of $\text{Cs}_3\text{OsO}_4\text{F}_3$ and CsF , and sum spectrum of the first two spectra. 86
- 6.9 XRD patterns of (a) black amorphous phosphorus; (b) amorphous phosphorus containing the byproduct Cs_2SiF_6 ; (c) phosphorus after heating sample (a). 89
- 6.10 SEM images of black amorphous phosphorus with small amounts of Cs_2SiF_6 crystals (white). Top: an overview of a large scale; bottom: focus on Cs_2SiF_6 crystals in the matrix of phosphorus. 90
- 6.11 High temperature X-ray diffraction patterns of amorphous phosphorus containing Cs_2SiF_6 as internal standard by using a Simon-Guinier camera. 91
- 7.1 The DSC measurement of SiBr_4 in a sealed Al container. 96
- 7.2 Three-dimensional representation of the observed scattered X-ray intensity for SiBr_4 as a function of diffraction angle (x -axis, 4.0 - 36.0° 2θ) and temperature (y -axis, 120 - 242 K, 2.25 $^\circ\text{C}/\text{min}$, 24 scans, $\lambda = 0.92103$ \AA). The phase transition at $T = 168$ K is clearly visible. This figure was prepared with Powder3D [158]. 97
- 7.3 Scattered X-ray intensity (a) for β - SiBr_4 at $T = 147$ K and (b) for α - SiBr_4 at $T = 237$ K as a function of diffraction angle 2θ . Shown are the observed pattern (diamonds), the best Rietveld profile fit in $P2_1/c$ for β - SiBr_4 and $Pa\bar{3}$ for α - SiBr_4 (line a), the difference curve between observed and calculated profile (line b), and the reflection markers (vertical bars). $\lambda = 0.92103$ \AA . 98

- 7.4 Crystal packing of (a) the LT β -phase (space group $P2_1/c$ at $T = 147$ K) and (b) HT α -phase (space group $Pa\bar{3}$ at $T = 237$ K) of SiBr_4 . Yellow spheres represent Si^{4+} , red spheres represent all Br^- in (a) and only $\text{Br}(2)$ in (b), and the pink ones in (b) represent $\text{Br}(1)$. 99
- 7.5 Cell volume (top), lattice parameters (middle) and powder diffraction patterns (bottom) of SiBr_4 as a function of temperature in the range from $T = 120$ K up to $T = 242$ K (2.28 K/minute). The phase transition at $T = 168$ K is clearly visible. The value in parentheses is the expansion coefficient of the corresponding parameter in $\text{\AA}/\text{K}$ for a , b and c , and in $\text{\AA}^3/\text{K}$ for volume, which was determined by a linear fit. 101
- 7.6 Temperature dependent X-ray powder diffraction patterns of SiBr_4 recorded with Simon-Guinier camera for a capillary of (a) $\text{\AA} = 0.1$ mm; (b) $\text{\AA} = 0.2$ mm; (c) $\text{\AA} = 0.3$ mm. 105

Bibliography

- [1] K. Knox, *Acta Cryst.* **1961**, *14*, 583.
- [2] S. Kadota, I. Yamada, S. Yoneyama, K. Hirakawa, *J. Phys. Soc. Jap.* **1967**, *23*, 751.
- [3] A. Okazaki, N. Tsukuda, *J. Phys. Soc. Japan* **1969**, *27*, 267.
- [4] K. Hirakawa, J. Yoshinaga, H. Miike, *J. Phys. Soc. Jap.* **1974**, *36*, 906.
- [5] H. Jacobs, D. Rechenbach, U. Zachwieja, *J. Alloys Compd.* **1995**, *227*, 10.
- [6] H. Jacobs, U. Zachwieja, *J. Less-Common Met.* **1991**, *170*, 185.
- [7] S. Mollah, *J. Phys.: Condens. Matter* **2004**, *16*, R1237.
- [8] M. W. Lufaso, P. M. Woodward, *Acta Cryst.* **2004**, *B60*, 10.
- [9] L. Šiller, N. Peltekis, S. Krishnamurthy, Y. Chao, S. J. Bull, M. R. C. Hunt, *Appl. Phys. Lett.* **2005**, *86*, 221912.
- [10] R. Juza, H. Hahn, *Z. Anorg. Allg. Chem.* **1939**, *241*, 172.
- [11] F. Gulo, A. Simon, J. Köhler, R. K. Kremer, *Angew. Chem. Int. Ed.* **2004**, *43*, 2032.
- [12] G. Paniconi, Z. Stoeva, H. Doberstein, R. I. Smith, B. L. Gallagher, D. H. Gregory, *Solid State Sci.* **2007**, *9*, 907.
- [13] J. Choi, E. G. Gillan, *Inorg. Chem.* **2005**, *44*, 7385.
- [14] J. Blucher, K. Bang, B. C. Giessen, *Mater. Sci. Eng.* **1989**, *A117*, L1.
- [15] R. Baranova, Y. Khodyrev, S. Semiletov, *Sov. Phys. Crystallogr.* **1982**, *27*, 554.
- [16] E. Gregoryanz, C. Sanloup, M. Somayazulu, J. Badro, G. Fiquet, H.-k. Mao, R. Hemley, *Nat. Mater.* **2004**, *3*, 294.
- [17] R. Yu, X. F. Zhang, *Appl. Phys. Lett.* **2005**, *86*, 121913.
- [18] B. R. Sahu, L. Kleinman, *Phys. Rev. B* **2005**, *71*, 041101(R).
- [19] J. A. Montoya, A. D. Hernandez, C. Sanloup, E. Gregoryanz, S. Scandolo, *Appl. Phys. Lett.* **2007**, *90*, 011909.
- [20] J. Zheng, *Phys. Rev. B* **2005**, *72*, 052105.
- [21] Z. W. Chen, X. J. Guo, Z. Y. Liu, M. Z. Ma, Q. Jing, G. Li, X. Y. Zhang, L. X. Li, Q. Wang, Y. J. Tian, R. P. Liu, *Phys. Rev. B* **2007**, *75*, 054103.
- [22] R. Yu, Q. Zhan, L. C. D. Jonghe, *Angew. Chem. Int. Ed. Engl.* **2007**, *46*, 1136.

- [23] J. Crowhurst, A. Goncharov, B. Sadigh, J. Zaug, Y. Meng, V. Prakapenka, *Mater. Res. Soc. Symp. Proc.* **2007**, 987, 3.
- [24] E. Gregoryanz, C. Sanloup, M. Somayazulu, J. Badro, G. Fiquet, H.-k. Mao, R. Hemley, *Nat. Mater.* **2004**, 3, 294.
- [25] A. F. Young, C. Sanloup, E. Gregoryanz, S. Scandolo, R. J. Hemley, H. K. Mao, *Phys. Rev. Lett.* **2006**, 96, 155501.
- [26] D. D. DesMarteau, T. Grelbig, S. Hwang, K. Seppelt, *Angew. Chem. Int. Ed. Engl.* **1990**, 29, 1448.
- [27] T. Drews, R. Marx, K. Seppelt, *Chem. Eur. J.* **1996**, 2, 1303.
- [28] W. Simmler, *Ullmann's Encyclopedia of Industrial Chemistry*, Silicon Compounds, Inorganic, Wiley-VCH, **2002**.
- [29] H. Lux, *Anorganisch-chemische Experimentierkunst*, Ed. J. A. Barth, 1954.
- [30] H. Kraus, H. Stach, *Z. Anorg. Allg. Chem.* **1969**, 366, 34.
- [31] G. Nolze, W. Kraus, *Powder Diffr.* **1998**, 13, 256.
- [32] A. Simon, *J. Appl. Cryst.* **1971**, 4, 138.
- [33] <http://www.ill.fr/YellowBook/D20/>, **2006**.
- [34] J. Rodriguez-Carvajal, *FULLPROF Suite Program, Version 1.00*, **Feb. 2007**.
- [35] Bruker, *TOPAS*, Version 3.0, Bruker AXS, Karlsruhe, Germany, **2000**.
- [36] A. A. Coelho, *J. Appl. Cryst.* **2003**, 36, 86.
- [37] A. LeBail, H. Duroy, J. L. Fourquet, *Mater. Res. Bull.* **1988**, 23, 447.
- [38] R. W. Cheary, A. A. Coelho, J. P. Cline, *J. Res. Natl. Inst. Stand. Technol.* **2005**, 109, 1.
- [39] A. Altomare, M. Burla, M. Camalli, B. Carroccini, G. Cascarano, C. Giacovazzo, A. Guagliardi, A. Moliterni, G. Polidori, R. Rizzi, *J. Appl. Crystallogr.* **1999**, 32, 115.
- [40] G. M. Sheldrick, *SHELXL-97: Program for the Refinement of Crystal Structures*, University of Göttingen, Germany, **1997**.
- [41] L. Farrugia, *J. Appl. Crystallogr.* **1999**, 32, 837.
- [42] M.-H. Whangbo, H.-J. Koo, D. Dai, *J. Solid State Chem.* **2003**, 176, 417.
- [43] M.-H. Whangbo, H.-J. Koo, D. Dai, *Solid State Sci.* **2005**, 7, 827.
- [44] R. Hoffmann, *J. Chem. Phys.* **1963**, 39, 1397.
- [45] L. Noodleman, *J. Chem. Phys.* **1981**, 74, 5737.
- [46] D. Dai, M.-H. Whangbo, *J. Chem. Phys.* **2001**, 114, 2887.
- [47] D. Dai, M.-H. Whangbo, *J. Chem. Phys.* **2003**, 118, 29.

- [48] F. Illas, I. d. P. R. Moreira, C. d. Graaf, V. Barone, *Theoret. Chem. Acc.* **2000**, *104*, 265.
- [49] M. U. Schmidt, H. Kalkhof, *CRYSCA*, Frankfurt am Main, Germany, **1997**.
- [50] D. M. Ceperley, B. J. Alder, *Phys. Rev. Lett.* **1980**, *45*, 566.
- [51] O. K. Andersen, *phys. Rev. B* **1975**, *12*, 3060.
- [52] E. C. Franklin, *J. Am. Chem. Soc.* **1905**, *27*, 820.
- [53] *SAMOA (Structure and Molecular Orbital Analyzer) program package*, this program can be downloaded free of charge from the website, <http://chvamw.chem.ncsu.edu/>.
- [54] L. F. Audrieth, *Angew. Chem.* **1932**, *23*, 385.
- [55] *Gmelins Handbuch der anorganischen Chemie*, Silber, *B1*, 143, **1971**.
- [56] L. C. Berthollet, *Chem. Ann. Crell.* **1788**, *2*, 390.
- [57] F. Rasehig, *Liebigs Ann. Chem.* **1886**, *223*, 93.
- [58] E. Gilbert, *Sci. Ind. Phot.* **1953**, *224*, 377.
- [59] L. J. Olmer, M. Dervin, *Bull. Soc. Chim. France* **1924**, *35*, 152.
- [60] M. Dervin, L. J. Olmer, *Compt. Rend.* **1922**, *175*, 1058.
- [61] H. Hahn, E. Gilbert, *Z. Anorg. Allg. Chem.* **1949**, *258*, 77.
- [62] L.A.C, *J. Pharm.* **1827**, *13*, 615.
- [63] M. Haisa, *Acta Cryst.* **1982**, *A38*, 443.
- [64] J. K. Luchs, *Phot. Sci. Enf.* **1966**, *10*, 334.
- [65] *STOE Win XPOW, Version 2.20*, Stoe & Cie GmbH, Germany, **Jun. 2006**.
- [66] T. Hahn, *International Tables for Crystallography*, A, Kluwer, Dordrecht, **1992**.
- [67] R. C. Agrawal, A. Chandra, A. Bhatt, Y. K. Mahipal, *J. Phys. D: Appl. Phys.* **2010**, *40*, 4714.
- [68] J. F. Pierson, D. Horwat, *Scripta Materialia* **2008**, *58*, 568.
- [69] <http://webelements.com/>.
- [70] C. D. Martin, W. A. Crichton, H. Liu, V. Prakapenka, J. Chen, J. B. Parise, *Am. Mineral.* **2006**, *91*, 1703.
- [71] R. J. Angel, J. Zhao, N. L. Ross, *Phys. Rev. Lett.* **2005**, *95*, 025503.
- [72] G. A. Samara, T. Sakudo, K. Yoshimitsu, *Phys. Rev. Lett.* **1975**, *35*, 1767.
- [73] P. Bouvier, J. Kreisel, *J. Phys. Condens. Matter* **2002**, *14*, 3981.
- [74] J. Kanamori, *J. Appl. Phys.* **1960**, *31*, 14S.
- [75] A. Tressaud, R. d. Pape, J. Portier, P. Hagenmüller, *C. R. Seances Acad. Sci. (Ser. C)* **1968**, 266.

- [76] F. Pompa, F. Siciliano, *Ric. Scient.* **1966**, 39, 21.
- [77] A. Ratuszna, K. Majewska, T. Lis, *Acta Crystallogr.* **1989**, C45, 548.
- [78] G. Benner, R. Hoppe, *J. Fluor. Chem.* **1990**, 46, 283.
- [79] W. Ruedorff, D. Babel, *Naturwissenschaften* **1962**, 49, 230.
- [80] F. Pompa, F. Siciliano, *Ric. Scient.* **1969**, 39, 370.
- [81] W. Ruedorff, J. Kaendler, D. Babel, *Z. Anorg. Allg. Chem.* **1962**, 317, 261.
- [82] M. Hidaka, M. Ono, *J. Phys. Soc. Jap.* **1977**, 43, 258.
- [83] Y. Simanov, L. Batsanova, L. Kovba, *Zh. Neorg. Khim.* **1957**, 2, 2410.
- [84] Z. Friedman, M. Melamud, J. Makovsky, H. Shaked, *Phys. Rev. B* **1970**, 2, 179.
- [85] A. Epstein, J. Makovsky, M. Melamud, H. Shaked, *Phys. Rev. B* **1968**, 174, 560.
- [86] D. T. Teaney, J. S. Blackburn, R. W. Stevenson, *Bull. Am. Phys. Soc.* **1962**, 7, 201.
- [87] V. Kaiser, M. Otto, F. Binder, D. Babel, *Z. Anorg. Allg. Chem.* **1990**, 585, 93.
- [88] J. Portier, A. Tressaud, J. Dupin, *C.R. Acad. Sc. Paris* **1970**, 270, 216.
- [89] A. d. Kozak, M. Samouël, J. Renaudin, G. Ferey, *Eur. J. Solid State Inorg. Chem.* **1988**, 25, 15.
- [90] A. Simon, *J. Appl. Cryst.* **1970**, 3, 11.
- [91] N. E. Brese, M. O'Keeffe, B. L. Ramakrishna, R. B. von Dreele, *J. solid State Chem* **1990**, 89, 184.
- [92] D. C. Johnston, R. K. Kremer, M. Troyer, X. Wang, A. Klümper, S. L. Bud'ko, A. F. Panchula, P. Canfield, *Phys. Rev. B* **2000**, 61, 9558.
- [93] V. Likodimos, N. Guskos, H. Gamari-Seale, A. Koufoudakis, M. Wabia, J. Typek, H. Fuks, *Phys. Rev. B* **1996**, 54, 12342.
- [94] L. J. deJongh, A. R. Miedema, *Adv. Phys.* **1974**, 23, 1.
- [95] J. Tong, C. Lee, M.-H. Whangbo, R. K. Kremer, A. Simon, J. Köhler, *Solid State Sci.* **2010**, 12, 680.
- [96] R. H. Odenthal, D. Paus, *Z. Anorg. Allg. Chem.* **1974**, 407, 144.
- [97] D. Dai, M.-H. Whangbo, J. Köhler, C. Hoch, A. Villesuzanne, *Chem. Mater.* **2006**, 18, 3281.
- [98] H.-J. Koo, M.-H. Whangbo, *J. Solid State Chem.* **2000**, 151, 96.
- [99] A. T. M. N. Islam, T. Hitosugi, E. Dudzik, T. Hasegawa, S. Ueda, Y. Takano, F. N. Islam, M. K. R. Khan, M. N. Islam, A. K. M. A. Islam, S. Watauchi, I. Tanaka, *Phys. Rev. B* **2009**, 80, 024505.
- [100] S. E. McLain, M. R. Dolgos, D. A. Tennant, J. F. C. Turner, T. Barnes, T. Proffen, B. C. Sales, R. I. Bewley, *Nature Materials* **2006**, 5, 561.

- [101] D. Kasinathan, K. Koepernik, U. Nitzsche, H. Rosner¹, *Phys. Rev. Lett.* **2007**, *99*, 247210.
- [102] X. Hao, Y. Xu, Z. Wu, D. Zhou, X. Liu, J. Meng, *Phys. Rev. B* **2007**, *76*, 054426.
- [103] H. Wu, D. I. Khomskii, *Phys. Rev. B* **2007**, *76*, 155115.
- [104] E.-J. Kan, L.-F. Yuan, J. Yang, J. G. Hou, *Phys. Rev. B* **2007**, *76*, 024417.
- [105] D.-Y. Liu, F. Lu, L.-J. Zou, *J. Phys. Condens Matter* **2009**, *21*, 026014.
- [106] D. Kasinathan, A. B. Kyker, D. J. Singh, *Phys. Rev. B* **2006**, *73*, 214420.
- [107] T. Lancaster, S. J. Blundell, P. J. Baker, W. Hayes, S. R. Giblin, S. E. McLain, F. L. Pratt, Z. Salman, E. A. Jacobs, J. F. C. Turner, T. Barnes, *Phys. Rev. B* **2007**, *75*, 220408.
- [108] M.-P. Zhang, Y.-M. Qian, G.-T. Wang, *Modern Phy. Lett. B* **2010**, *24*, 39.
- [109] T. Masuda, A. Zheludev, A. Bush, M. Markina, A. Vasiliev, *Phys. Rev. Lett.* **2005**, *94*, 039706.
- [110] M. Gratzel, *Heterogeneous Photochemical Electron Transfer*, CRC Press, Baton Rouge, FL, **1988**.
- [111] D. Kasinathan, K. Koepernik, U. Nitzsche, H. Rosner, *Phys. Rev. Lett.* **2007**, *99*, 247210.
- [112] M. M. Mikhailov, V. V. Neshchimenko, *J. of Surface Investigation. X-ray, Synchrotron and Neutron Techniques* **2009**, *3*, 950.
- [113] H. Yang, Z. Wang, M. Gong, L. Liang, *J. Alloys and Compounds* **2009**, *488*, 331.
- [114] Y. Q. Li, C. M. Fang, Y. Fang, A. C. A. Delsing, G. d. With, H. T. Hintzen, *J. solid State Chem.* **2009**, *182*, 3299.
- [115] R. J. Radwanski, Z. Ropka, <http://arxiv.org/abs/0804.4111v1> **2008**.
- [116] J. I. Pankove, *Optical Processes in Semiconductors*, Prentice-Hall, Englewood Cliffs, NJ, **1971**.
- [117] D. Wang, K. Tang, Z. Liang, H. Zheng, *J. solid State Chem* **2001**, *183*, 361.
- [118] B. G. Müller, *Z. Anorg. Allg. Chem.* **1987**, *553*, 196.
- [119] M.-H. Whangbo, private communication.
- [120] B. A. O'Brien, D. D. DesMarteau, *J. Org. Chem.* **1984**, *49*, 1467.
- [121] Y. Y. Zhang, Q.-C. Mir, B. A. O'Brien, D. D. DesMarteau, *Inorg. Chem.* **1984**, *23*, 518.
- [122] E. Ruiz, S. Alvarez, *J. Am. Chem. Soc.* **1995**, *117*, 2877.
- [123] R. Bougonka, B. Buua, K. Seppelt, *Chem. Ber.* **1993**, *126*, 1331.

- [124] A. Holleman, N. Wiberg, *Lehrbuch der Anorganischen Chemie*, XV 2.1.3, de Gruyter, **1985**.
- [125] H. Okudera, R. E. Dinnebier, A. Simon, *Z. Kristall.* **2005**, *220*, 259.
- [126] B. Hofmann, R. Hoppe, *Z. Anorg. Allg. Chem.* **1979**, *458*, 151.
- [127] P. J. Jones, W. Levason, M. Tajik, *J. Fluor. Chem.* **1984**, *25*, 195.
- [128] W. P. Griffith, *J. Chem. Soc. (A)* **1969**, 211.
- [129] M. E. Welk, A. J. Norquist, C. L. Stern, K. R. Poepelmeier, *Inorg. Chem.* **2001**, *40*, 5479.
- [130] J. Köhler, J. Chang, M. Whangbo, *J. Am. Chem. Soc.* **2005**, *127*, 2277.
- [131] S. A. Brewer, A. K. Brisdon, J. H. Holloway, E. G. Hope, *J. Fluor. Chem.* **1993**, *60*, 13.
- [132] *Inorganic Crystal Structure Database (ICSD)*, Karlsruhe, Germany.
- [133] M. Gerken, D. A. Dixon, G. J. Schrobilgen, *Inorg. Chem.* **2000**, *39*, 4244.
- [134] U. Gross, S. Rudiger, A. R. Grimmer, E. F. Kemnitz, *J. Fluor. Chem.* **2002**, *115*.
- [135] S. Hayashi, K. Hayamizu, *Bull. Chem. Soc. Jpn.* **1990**, *63*, 913.
- [136] H. Pizzala, C. Barrère, M. Mazarin, F. Ziarelli, L. Charlesa, *J. Am. Soc. Mass Spectrom.* **2009**, *20*, 1906.
- [137] W. J. Casteel, D. A. Dixon, H. P. A. Mercier, G. J. Schrobilgen, *Inorg. Chem.* **1996**, *35*, 4310.
- [138] M. Gerken, D. A. Dixon, G. J. Schrobilgen, *Inorg. Chem.* **2002**, *41*, 259.
- [139] F. Krauss, D. Wilken, *Z. Anorg. Allg. Chem.* **1925**, *145*, 151.
- [140] A. Simon, H. Borrmann, J. Horakh, *Chem. Ber./Recueil* **1997**, *130*, 1235.
- [141] A. Simon, H. Borrmann, H. Craubner, *Phosphorus and Sulfur and the Related Elements* **1987**, *30*, 507.
- [142] A. Brown, S. Runquist, *Acta Crystallogr.* **1965**, *19*, 684.
- [143] L. Cartz, S. R. Srinivasa, R. J. Riedner, J. D. Jorgensen, T. G. Worlton, *J. Chem. Phys.* **1979**, *71*, 1718.
- [144] M. Baba, F. Izumida, Y. Takeda, A. Morita, *Jpn. J. Appl. Phys.* **1989**, *28*, 1019.
- [145] S. Lange, P. Schmidt, T. Nilges, *Inorg. Chem.* **2007**, *46*, 4028.
- [146] T. Nilges, M. Kersting, T. Pfeifer, *J. Solid State Chem.* **2008**, *181*, 1707.
- [147] E. Pohland, *Z. Anorg. Allg. Chem.* **1931**, *201*, 265.
- [148] M. W. Lister, L. E. Sutton, *Trans. Farad. Soc.* **1941**, *37*, 393.
- [149] R. Spitzer, W. J. J. Howell, V. Schomaker, *J. Am. Chem. Soc.* **1942**, *64*, 62.

- [150] M. T. d. N. Varella, A. P. P. Natalense, M. H. F. Bettega, M. A. P. Lima, *Phys. Rev. A* **1999**, *60*, 3684.
- [151] A. K. Wolf, J. Glinnemann, M. U. Schmidt, *CrystEng-Comm* **2008**, *10*, 1364.
- [152] H. Mark, E. Pohland, *Z. Kristallogr.*, *64*, 113.
- [153] A. Simon, K. Peters, *Acta Cryst.* **1980**, *B36*, 2750.
- [154] J. Köhler, H. Okudera, D. Reuter, A. Simon, *Z. Kristallogr.* **2005**, *220*, 523.
- [155] J. Köhler, H. Okudera, A. Simon, *Z. Kristallogr.* **2005**, *220*, 524.
- [156] A. K. Wolf, J. Glinnemann, M. U. Schmidt, J. Tong, R. E. Dinnebier, A. Simon, J. Köhler, *Acta Cryst.* **2009**, *B65*, 342.
- [157] A. P. Hammersley, S. O. Svenson, M. Hanfland, D. Hauserman, *High Press. Res.* **1996**, *14*, 235.
- [158] B. Hinrichsen, R. E. Dinnebier, M. Jansen, *Z. Kristallogr. Suppl.* **2006**, *23*, 231.
- [159] C. Kratky, H. Hengge, H. Stüger, A. L. Rheingold, *Acta Cryst.* **1985**, *C41*, 824.
- [160] M. Caffrey, *Annu. Rev. Biophys. Biophys. Chem.* **1989**, *18*, 159.
- [161] A. K. Wolf, J. Glinnemann, M. U. Schmidt, J. Tong, R. E. Dinnebier, A. Simon, J. Köhler, *Acta Cryst.* **2009**, *B65*, 342.

Publications

- Crystal structures of α -silicon tetrabromide, α -SiBr₄, *room temperature modification*
J. Tong, C. Hoch, A. Simon and J. Köhler
Submitted to *Z. Kristallogr.*
- Crystal structure of β -silicon tetrabromide, β -SiBr₄
J. Tong, C. Hoch, A. Simon and J. Köhler
Submitted to *Z. Kristallogr.*
- Silver(I) Pyrophosphonates: Structural, Photoluminescent and Thermal Expansion Studies
L. Guo, J. Tong, X. Liang, J. Köhler, J. Nuss, Y. Li and L. Zheng
Submitted to *Chem. Eur. J.*
- A Novel Mesoporous Iron-Based Fluoride Cathode of Tunnel Structure for Rechargeable Lithium Batteries
C. Li, L. Gu, J. Tong, S. Tsukimoto. and J. Maier
Submitted to *J. Am. Chem. Soc.*
- Magnetic and optical properties of the two-dimensional ferromagnet Cs₂AgF₄
J. Tong, M. Whangbo, R. Kremer, A. Simon and J. Köhler
Z. Kristallogr. **2010** 225 (in print)
- Cooperative Jahn-Teller distortion leading to the spin-1/2 uniform antiferromagnetic chains in triclinic perovskites AgCuF₃ and NaCuF₃
J. Tong, C. Lee, M. Whangbo, R. Kremer, A. Simon and J. Koehler
Solid State Sci. **2010** 12, 680.
- SiBr₄ – prediction and determination of crystal Structures
A. Wolf, J. Glinnemann, M. Schmidt, J. Tong, R. Dinnebier, A. Simon and J. Koehler
Acta Cryst. **2009** B65, 342.

- Metal phosphonates based on bis(benzimidazol-2-ylmethyl)imino methylenephosphonate: From discrete dimer to two-dimensional network containing metallomacrocycles

D. Cao, J. Xiao, J. Tong, Y. Li and L. Zheng

Inorg. Chem. **2007** *46*, 428.

Acknowledgements

I am indebted to the following people without whom this work would not have been possible:

- Prof. Arndt Simon and Prof. Jürgen Köhler, for the opportunity to work at the Max-Planck-Institute and to be a member in their group as well as for the friendly guidance and encouragement throughout all the time.
- Dr. Reinhard K. Kremer, for his constant help, enthusiasm and discussion related to some areas of this thesis and physics.
- Prof. Robert Dinnebier for his beneficial and patient help in especially powder diffraction as a teacher and a member of my PhD committee.
- Dr. Constantin Hoch, for his great and innovative help growing SiBr_4 single crystals and solving single crystal structures.
- Friedrich Kögel for his general help in my experiments for a good working condition.
- Dr. Grigori Vajenine and Dr. Volodymyr Babizhetskyy for their professional discussion and advice for my work.
- Viola Duppel, Claudia Kamella, Willi Hölle, Hartmut Gärtling and Roland Eger for constant assistance in EDX, SEM, Low Temperature X-ray diffraction and DTA experiments.
- Eva Brücher and Gisela Siegle, for constant assistance in specific heat and magnetization measurements.
- Prof. Myung-Hwan Whangbo and Dr. Dai Dadi for their collaboration and always fast communication in calculations and writings on magnetism and optical spectroscopy.
- Ewald Schmitt and Sabine Seiffert for their friendly and tolerant assistance in TG and DSC experiments.
- Armin Schulz for his hospitality and assistance in Raman Spectroscopy measurements.

- Wolfgang König for assistance in IR and UV-Vis Spectroscopy.
- Thomas Bräuniger and Vinodchandran Chandrasekharan Nair for professional help in NMR measurements.
- Ilias Efthimiopoulos and Dr. Karl Syassen for their discussion and help performing High pressure synchrotron experiments on NaCuF_3 at ESRF, Grenoble.
- Dr. Thomas Hansen, for his kind help performing neutron diffraction experiments at ILL, Grenoble.
- Dr. Xiaoping Yang for her kind help in band structure calculations as a good friend.
- Nan Jiang, Tzu-Chun Tseng, Xiuping Gao, Dr. Shuiquan Deng and Lei Wang for communication in science and sharing good time together.
- Joseph Law and Prof. Jun Sung Kim for their enthusiastic discussion and interest on my work and for good company.
- Philip Brydon, Micheal banks, Puravankara Sreeraj, Manuel Schaloske, Volodymyr Smetana, Patrick Reuvekamp and Hailey Williamson for being reliable friends and colleagues.
- My parents and sister for all care and support throughout the time.
- Last but certainly not least, all my remaining colleagues who I have shared tea and coffee time with over my years here at the Max Planck Institute.

Curriculum Vitae

August 14, 1982	born in Nanjing, China
09.1996 – 06.1999	High School at Nanjing Zhonghua Middle School
09.1999 – 06.2003	Bachelor studies in Chemistry at Nanjing University, China
09.2003 – 06.2006	Graduate studies and master of Science in the group of Prof. L. Zheng at Nanjing University, China, with the thesis “Synthesis and study of coordinating compounds with phosphonic acid ligands; investigation of surface modification of nanotitania”
since 09.2006	PhD student in the group of Prof. A. Simon at Max-Planck-Institut für Festkörperforschung, Stuttgart, Germany, with the thesis “Preparations, Structures and Properties of Selected Perovskite Materials and Molecular Crystals”